5-2022

Strain-based Design of Steel-Polymer-Steel Composite Pipes

Vul Thang
vthang@uno.edu

Strain-based Design of Steel-Polymer-Steel Composite Pipes

A Dissertation

Submitted to the Graduate Faculty of the
University of New Orleans
in partial fulfillment of the
requirements for the degree of

Doctor of Philosophy
in
Engineering and Applied Science
Mechanical Engineering

by

Vul Thang, P.E.
B.Eng. National University of Singapore, 2010
M.S. Lamar University, 2014
May 2022

To Peter W. Marshall, my great friend, and professor.

ACKNOWLEDGEMENT

God, my creator, who created heaven and earth is the one who has brought me this far. I would like to thank Him first and foremost. Secondly, without the help of Dr. Peter W. Marshall, I would not be writing this dissertation. I will not forget all the hardships he went through with me. May God rewards him for all the wonderful help he had provided, and his support for this research work. I inherited so much wisdom and knowledge from him.

I would also like to thank Dr. David Hui for his guidance, advice, encouragement, and time throughout my Ph.D. program. I would like to thank the committee for their time during these difficult times, through Covid-19, Hurricane Zeta, and Hurricane Ida.

My thanks also go to Dr. Jianren Zhou, a mechanical engineering professor at Prairie View A&M University, and Dr. Nan Wu, a mechanical engineering professor at the University of Manitoba for their comments on my research work. I would also like to thank Charlie Speed for his comments and advice. I will also not forget Ph.D. candidate John Lair for some of his advice and I will miss those good times. Many people have helped me in the past and because of these, I have a chance to write this dissertation. May God bless them all.

My wife Khuang, daughter Estella, and son Peter are always in my heart.

TABLE OF CONTENTS

LIST OF FIGURES

LIST OF TABLES

ABSTRACT

Many offshore single-wall pipelines and structural failures have occurred in the past. As a result, lives were lost, and billions of dollars were spent. In addition, natural disasters such as earthquake fault zones can cause a large volume of soil movement. This can easily damage single-wall pipelines or piles of fixed offshore platforms in the earthquake fault zone.

Currently, the single-wall pipelines are used for the offshore and onshore oil and gas industry. This research investigated the use of double-wall composite pipe steel-polymer-steel (SPS) in place of single-wall pipe to prevent such failures. The double-wall composite pipe has a larger displacement capacity, higher load capacity, the ability to take higher pressure, more heat resistance, and more ductility than the single-wall pipe. Hence, this research studied improvement using double-wall composite pipes and the test results were compared against the single-wall pipes. At the first step of the research, portal steel tubular beams verifications and validations were performed. Then, the laterally loaded steel pipe in clay verification exercises were conducted. Thereafter, the single-wall and double-wall composite pipes were analyzed in clay and the results were compared. Strain, von Mises stresses, and ovality of the pipes were observed and compared against the industry standard. Four-point beam bending tests were also performed for the single and double-wall composite pipes. Boned and unboned behavior of steel and polymer were studied for the composite pipe. The stiffnesses of the clay were changed and the behavior of the steel pipe was investigated. The stiffnesses of the polymer were varied and the behavior of the composite pipes was observed. The annulus size of composite pipes was also varied, and the analysis results were documented. Weld was introduced in the pipe connection and the welding effect was observed. This research work finds significant improvement in the SPS double-wall composite pipe.

Keywords: Double-wall composite pipe; pile in clay; sandwich pipe, steel-polymer-steel; pipe ovalization; strain-based design; offshore pipeline; offshore pile foundation, finite element analysis of pile in clay

CHAPTER 1 INTRODUCTION

1.1 Background

Steel tubular structures are widely used in offshore structures such as fixed, floating, and pipelines. Figure 1.1 shows a pipeline crossing an earthquake fault plane. For a pipeline crossing earthquake fault plane, the steel pipe can be displaced as large as 7 feet which could cause serious damage to offshore fixed platforms pile foundation and the offshore pipeline. This research is to prevent such failure by strengthening a single-wall tubular with a double-wall in which the annulus is grouted with polymer using an enhanced strain-based design. Another benefit is the reduced risk and cost-saving. The composite pipe will use lesser steel material and hence the cost could be even lower if not the same compared to using a thick single-wall tubular, but the strength and ductility of the steel composite pipe are expected to be significantly improved. Thus, this research is to reduce risks, in other words, save costs and lives.

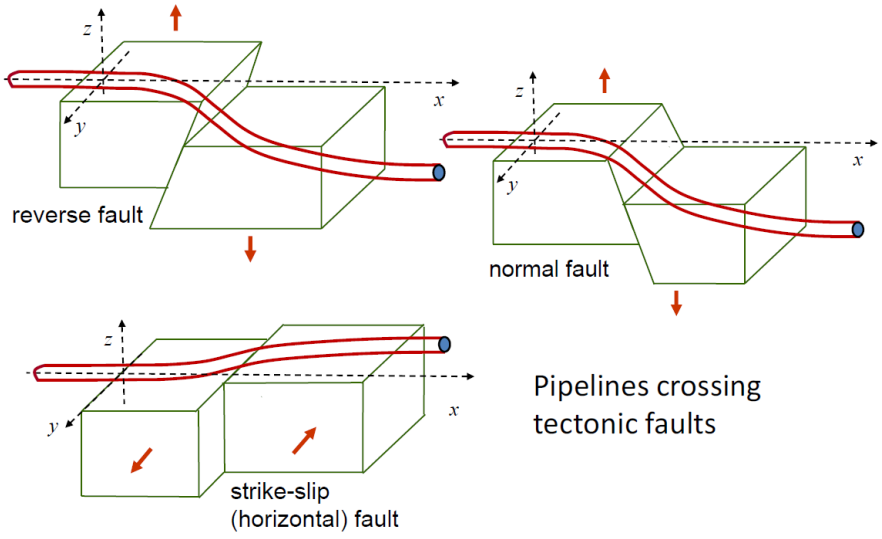

Figure 1.1 Schematic representation of pipeline configuration crossing tectonic faults

(Karamanos, Keil, & Card, 2014)

The strain-based design for double-wall steel pipeline with polymer grouted was introduced by Marshall (2004). However, no test has been performed. Double-wall pipes with annulus grouted with cement, concentric tubular, have been used as oil well casing since the late 1800s and the composite section was later used in offshore jacket platform legs. There are several research available for this. Figure 1.2 shows a fixed offshore jacket structure with a pile inside the jacket leg. The issue for the cement grouted composite section is the bond between the cement and the steel surface. There is debonding between the two materials reduces the effectiveness of the composite. Recently, there were several studies conducted to increase the steel and cement grout. Marshall et al. (2014) led the research in finding improvement on the bond between steel and cement grout, by introducing studs on the interface between steel and cement. They performed the simplified experiment and finite element (FE) analysis. This research investigates the benefits of the application of the polymer grouted double-wall tubular composite pipe.

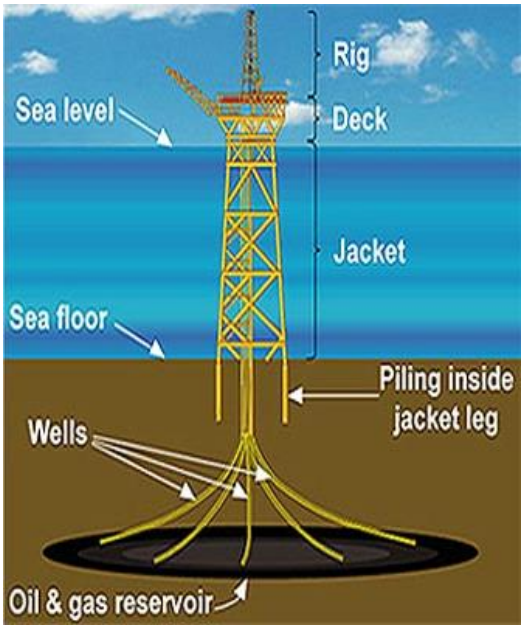

Figure 1.2 Fixed offshore structure with pile foundation
(Engineer, 2017)

Offshore oil and gas accidents can be costly, and there were several failures in the past. Looking at a recent offshore pipeline burst in the Gulf of Mexico as shown in Figure 1.3, a seafloor pipeline gas leak caused flame boiling in the water. Although the fire was put out successfully after a few hours, there were several issues that needed to be resolved such cleaning and repairing and this can be costly. This research intention is to prevent such failures from re-occurring.

Figure 1.3 Gas leak from seafloor pipeline causing a fire in the Gulf of Mexico

(Cohen, 2021)

A schematic diagram of a single wall seafloor pipeline crossing an earthquake fault is shown in Figure 1.4. In the figure, the single wall pipe failed by buckling and wrinkling. A sharp slope discontinuity or a kink appears on the pipe, and this would significantly increase strain in the pipe and decrease the pipe opening.

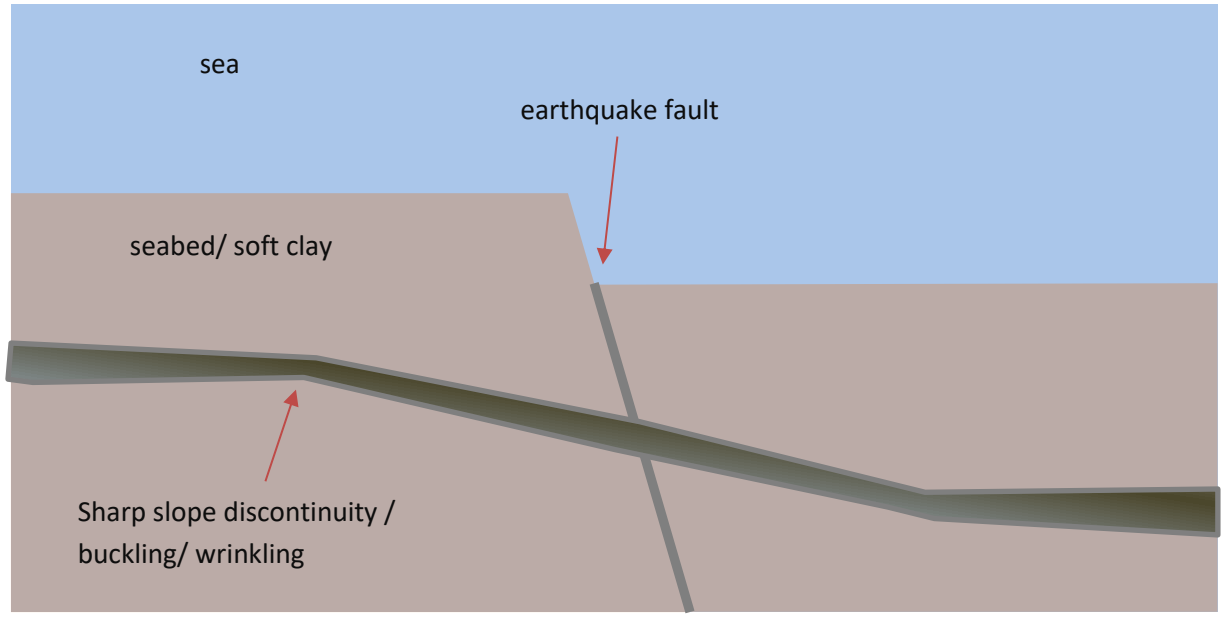

Figure 1.4 Schematic diagram of a single-wall seafloor pipeline failure at earthquake fault plane

1.2 Objectives and Scopes

The objectives of this study are:

1 To test portal beams and compare them with experimental results. These represent portal piling in offshore structures and the failure results are observed.

2 To test double-wall composite pipes in which the annulus is grouted with cement. These are similar to the composite pipe in this research.

3 To verify the numerical calculation of single-wall pipe offsets crossing earthquake fault zone.

4 To test laterally loaded single-wall pipe in clay and validate the experimental results and rigid plastic model in the literature. After the validation, test laterally loaded steel-polymer-steel composite pipe in clay.

5 To compare the double-wall composite pipe and single-wall pipe with the same overall thickness of the composite pipe.

6 To test single-wall and double-wall composite pipes in the air and investigate their failure. Perform parameters studies of the composite pipe.

7 Investigate improvement in double-wall composite pipe crossing earthquake fault zone and improve the design.

The summary of the workflow of this research work is shown in Figure 1.5

Figure 1.5 below shows the summary workflow of this research work.

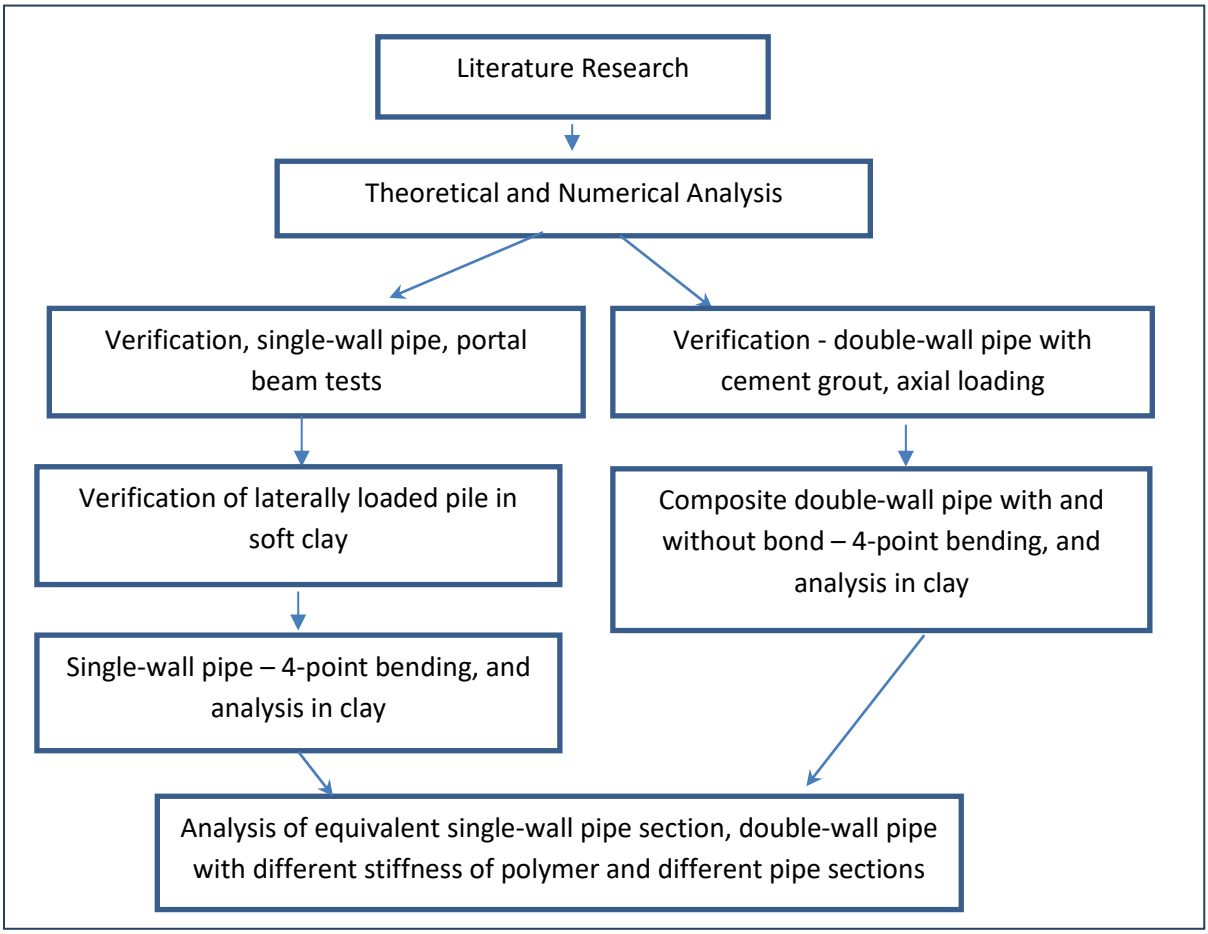

Figure 1.5 Research workflow

The double-wall composite pipe section in this research is shown in Figure 1.6.

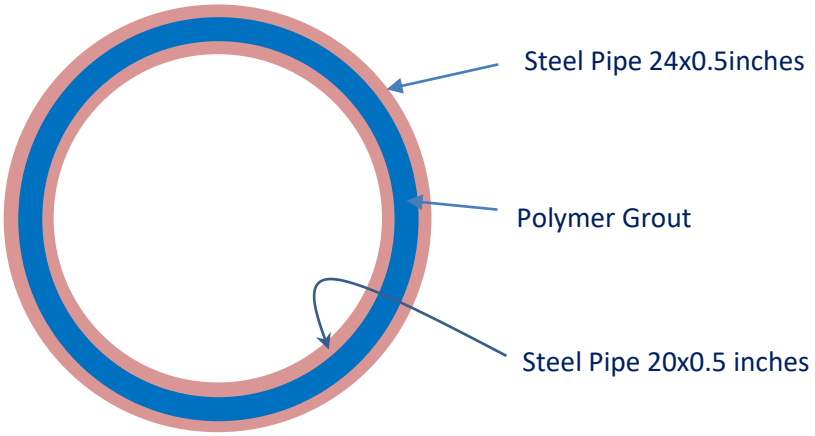

Figure 1.6 Steel-polymer-steel composite section

1.3 Finite Element Analysis Applications

- Polymer material used in this research is not yet available in the industry at the time of this research work. The polymer material is to be studied in future work. Hence, readily available FE packages use is advantageous to perform this research work.
- Using numerical hand calculation, it can take too long to solve the problems. Steel, polymer, cement, and clay materials in addition to complex boundary conditions, loads, different mesh sizes, and material surface interactions are involved in this research work, and it is not practical to solve using mathematical manual calculation. Hence, to have more productive results, FE analysis is used.
- FE analysis also serves as another source (independent) to give results that can be compared against literature or the experimental results. In addition, variables can be changed easily, and a different analysis can be performed easily. Hence this approach saves time and cost which is very crucial.

- Validations of several experimental results are performed in this research to ensure the validity and accuracy of the steel-polymer-steel FE analysis results.

1.4 Dissertation Layout

This research work consists of ten chapters. Chapter one earlier has described issues faced in pipeline due to earthquake and briefly stated composite pipe in offshore structures. It also stated the advantages of using FE analysis in this research.

Chapter 2 is the literature for this research work. This includes pile foundation displacement in offshore structure, failure in structures, single-wall pipe in clay, cement grout in concentric tubular, welding misalignment in tubular, wrinkling in the tubular pipe, pipe ovalization, strain limits of the pipeline, fracture and cracks propagation of single-wall pipeline, plastic deformation of the simply supported beam, soft clay foundation, and SPS composite pipe.

Chapter 3 includes design calculations. The calculations include the single-wall pipe strain limit and the limit of the offset. Chapter 4 includes portal beam FE tests verification with experimental results. This chapter also stated the benefits of using tubular pipes in offshore structures. Chapter 5 includes cement grout concentric tubular axial loadings FE tests and a comparison with the experimental results. Chapter 6 studies laterally loaded single-wall pipe in clay, double-wall pipe in clay, mesh size studies, and the same single-wall pipe thickness as the overall composite pipe in clay. Chapter 7 is a study on simply supported beam bending analysis of the single-wall and double-wall composite pipes in air and the investigations of their failures.

Chapter 8 documents the finding summary of the research. Chapter 9 includes conclusions based on the analysis findings. Chapter 10 is the recommendation for future research.

The graphical abstract of this research is shown in Figure 1.7.

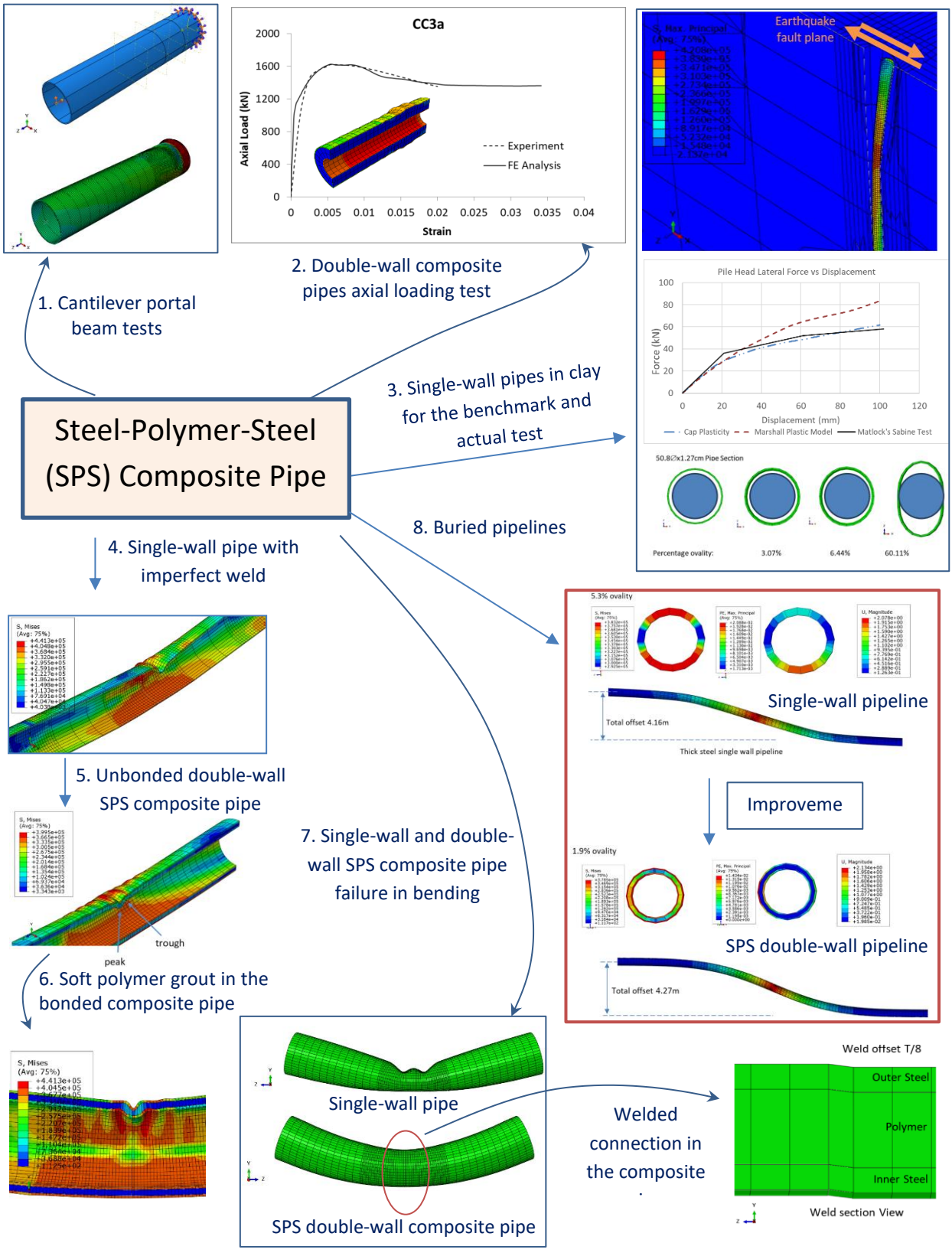

Figure 1.7 Abstract of the research

CHAPTER 2 LITERATURE REVIEW

The laterally loaded single and SPS double-wall composite pipes in this research are embedded in soft and medium clay. Piles and pipelines in the earthquake fault zone experience buckling and wrinkling due to large displacement. Ovalization, high strain, and fractures are found in single-wall pipes. Welding misalignment between two pipe connections may also contribute to buckling, wrinkling, and ovalization in the pipes. The single-wall pipe is embedded in soft and medium clay and laterally loaded at the top and the displacement capacity is observed. The SPS double-wall composite pipe is introduced in this research to mitigate or eliminate some failure modes found in the single-wall composite pipe. More detailed information on the literature found is documented in this chapter.

2.1 Offshore Structures

A large wave that is larger than the designed wave can impact the offshore platform. Water waves impacting the deck instead of supporting the structure will result in forces well in excess of the designed structure. Figure 2.1 shows wave forces acting on the structure. Offshore structures failure is more a problem of strength than one of stability (Marshall, 1982). Tubular struts provide lateral bracing for the structure, and these are designed as beam-columns. Primary axial load (P) must be resisted in the presence of bending due to lateral loads (Q). The loads come from wave forces, buoyancy, marine growth, and the structure's self-weight. The lateral loads are resisted by soil pressures at the base of the structure through tubular piles. These laterally loaded piles may represent portal beam-column that are subjected to bending due to shear load (Q), and axial loads (P). The portal beam column is a two-hinge failure mechanism as shown in Figure 2.1.

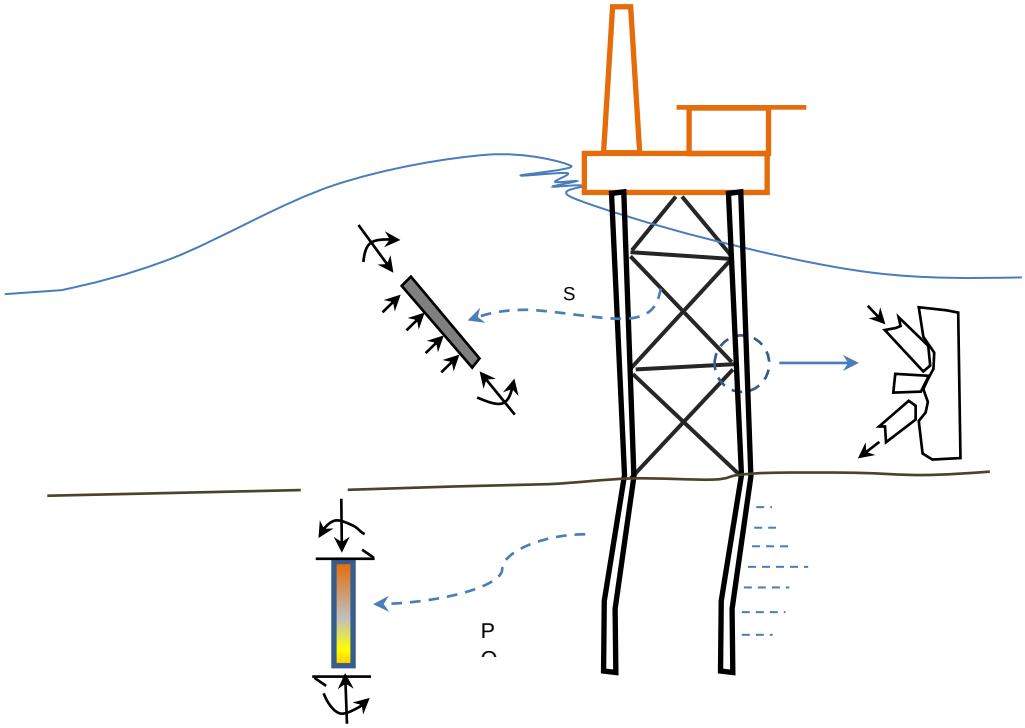

Figure 2.1 Wave loading on offshore jacket platform

(Marshall, 1982)

When lateral loads such as wind, wave, and current exceed the ultimate load capacity of the structure, collapse occurs because the loads are acting on the structure repeatedly. However, it is not the case for earthquakes. Forces due to earthquakes come from a structural response to ground motions. In earthquakes, the structure can exceed the elastic limit energy by factors of four or more without collapse (Marshall, 1982). Yielding may be helpful in limiting the applied forces, and ductility becomes important in measuring structural performance.

Figure 2.2 shows a large displacement due to an earthquake and the displacement is denoted as a big delta. The topside or deck gets left behind due to sudden displacement, and this causes the structure to be distorted. From the figure, it can be seen that the structure experiences yielding in the brace, buckling compression, and fracturing tension braces. In addition, the portal

mechanism occurs in the superstructure's legs and in the piling. However, the structure remains stable in the damaged condition because it has sufficient reserve strength. The earthquake may also be associated with ground distortion of several feet, and it is denoted at a small delta in the figure. This can produce several elastic stresses in piling, conductors, and pipelines. However, if there is sufficient ductility, the displacements can safely be accommodated in the plastic range. Marshall (1982) also stated different forms of local buckling.

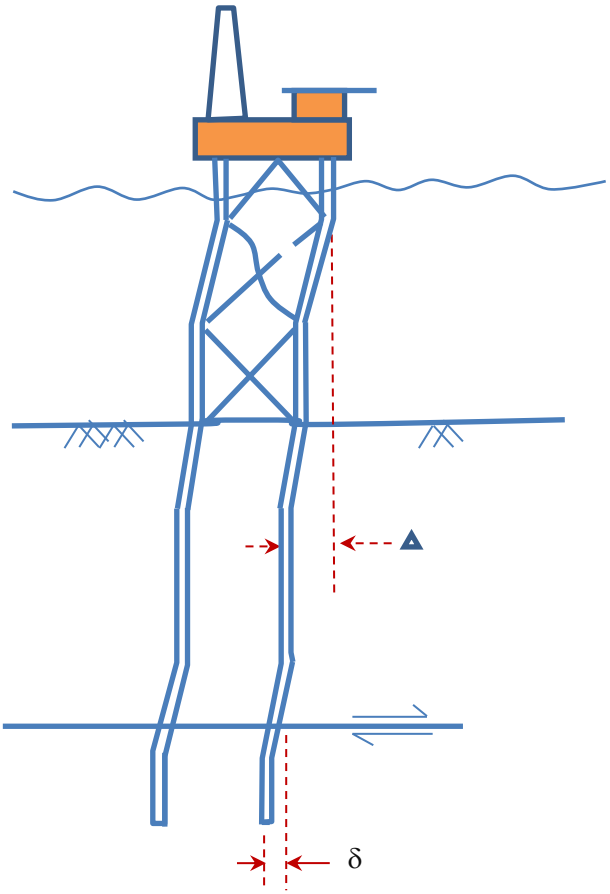

Figure 2.2 Displacement due to earthquake

(Marshall, 1982)

Sherman (1980) has conducted a series of over 100 tests of struts and portal type beam-columns at the University of Wisconsin-Milwaukee.

The allowable buckling stress, σ, of the long column is given by Beer, Johnston, Jr., & DeWolf (2006) as

$$\sigma = \frac{\pi^2 E}{\left(\frac{l}{r}\right)^2} \qquad (2.1)$$

where, l = length of the column

r = radius of gyration

E = modulus of elasticity

These portal piles are similar to portal beam tests to be performed in the objectives. In addition, the SPS double-wall composite pipe will also act as an enhancement to the single-wall pipes or piles.

2.2 Displacement of Single-wall Pipe in Clay

Marshall (1982) stated that the critical bending strain and plastic hinge rotation in single-wall tubular members are strongly dependent on the thickness or t/D. He calculated single-wall tubular displacement capacity and Table 2.1 shows his calculation results. Marshall (2004) used a very small value of strain, less than 0.005 for plastic clay, and medium clay compressive strength of 1200 psf. His single-wall pipe offsets calculation results are shown in Table 2.1.

Table 2.1 Marshall (2004) numerical results

Tubular size (in)	Critical strain	Hinge angle (degree)	Offset at failure
Original 20∅0.5 pipe	1.25%	2.5	1.3 ft
Heavier 20∅1.0 pipe	2.5%	6.2	3.4 ft

Marshall (1982) used the survivability behavior of piles shown in Figure 2.3 for his strain-based design calculations.

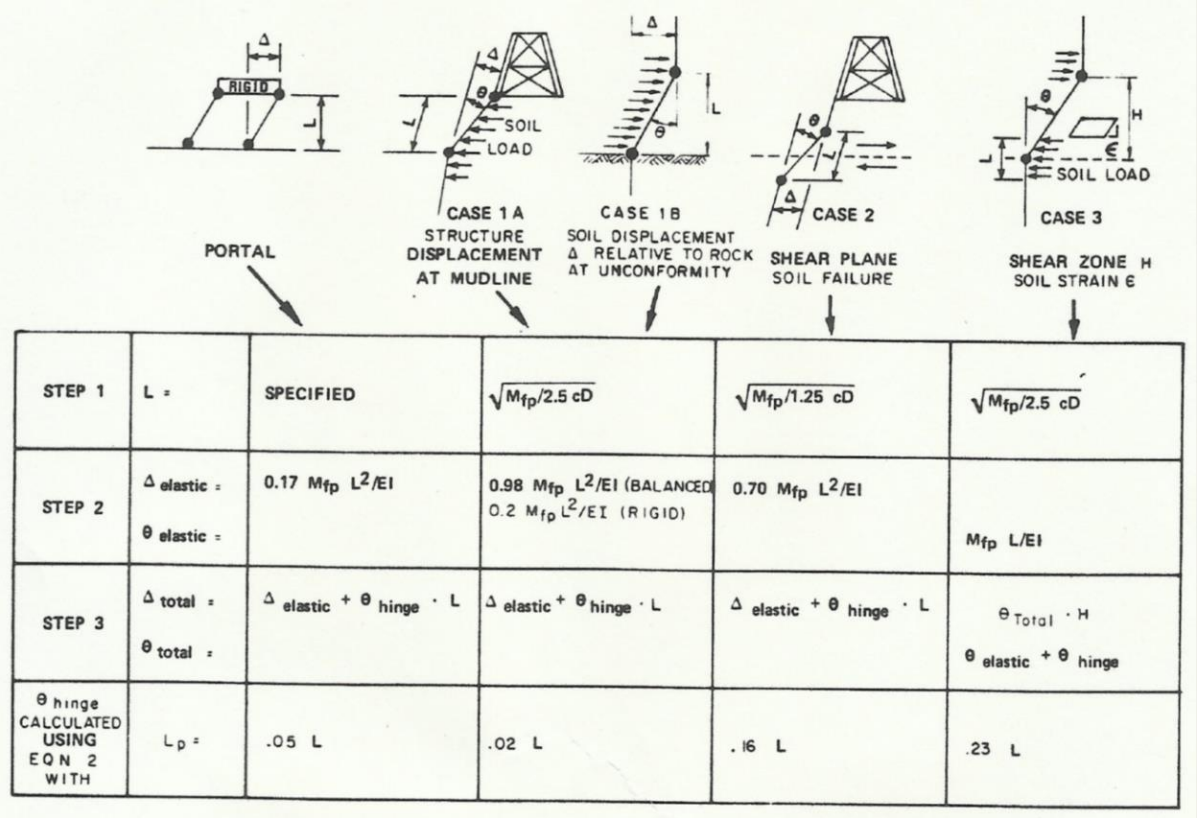

STEP 1	L =	SPECIFIED	$\sqrt{M_{fp}/2.5\ cD}$	$\sqrt{M_{fp}/1.25\ cD}$	$\sqrt{M_{fp}/2.5\ cD}$
STEP 2	Δ elastic = θ elastic =	0.17 $M_{fp}\ L^2/EI$	0.98 $M_{fp}\ L^2/EI$ (BALANCED) 0.2 $M_{fp}\ L^2/EI$ (RIGID)	0.70 $M_{fp}\ L^2/EI$	$M_{fp}\ L/EI$
STEP 3	Δ total = θ total =	Δ elastic + θ hinge · L	Δ elastic + θ hinge · L	Δ elastic + θ hinge · L	θ_{Total} · H θ elastic + θ hinge
θ hinge CALCULATED USING EQN 2 WITH	L_p =	.05 L	.02 L	.16 L	.23 L

Figure 2.3 Survivability behavior of piles

(Marshall, Gates, & Nahin, 1977)

The plastic hinge rotation is θ_p calculated by

$$\theta_p = (\phi_{cr} + \phi'_y)*(L_p + L_b) \qquad (2.2)$$

where

Critical curvature, $\phi_{cr} = 2*\varepsilon_{cr}/D$

Critical strain, $\varepsilon_{cr} = 0.5*t/D$, t is the tubular wall thickness, and D is the outer tubular diameter

Elastic curvature corresponding to fully plastic moment, $\phi'_y = 2.54\ \sigma_y / (D*E)$, σ_y is the allowable stress, and E is the modulus of elasticity.

Length of local buckling along the pipe axis, $L_b = 122\ (t/D)^{2.5}$ for classical local buckling

Moment persistent length, L_p is calculated as per the formula in Figure 2.3.

For a two-hinge plastic mechanism, total offset displacement is calculated by

Total offset displacement, $\Delta = \Delta_{elastic} + \theta_p L$ (2.3)

where,

L is the total length between the plastic hinges

$\Delta_{elastic}$ is the displacement which would be achieved by an elastic beam with moments up to the fully plastic moment. Formulas are shown in Figure 2.3.

For a pipeline crossing a fault, or a piling crossing a plane of soil displacement, a rigid plastic mechanism with hinges and similar soil on either side of the slip plane yields

$L = \text{sqrt}(8 M_{fp}/Q)$

Where,

M_{fp} is the fully plastic moment of the pipe

Q is the ultimate soil resistance to lateral pipe movement

$Q = 12 cD$

c is the shear strength of the soil

Marshall (2004) provided a sketch of the displaced offshore pipeline due to the earthquake as shown in Figure 2.4. It is relatively clear in the sketch as it shows the displacement or deflection in the pipe due to an earthquake fault. The strain-based method calculates the total displacement the pipe can withstand before fracture.

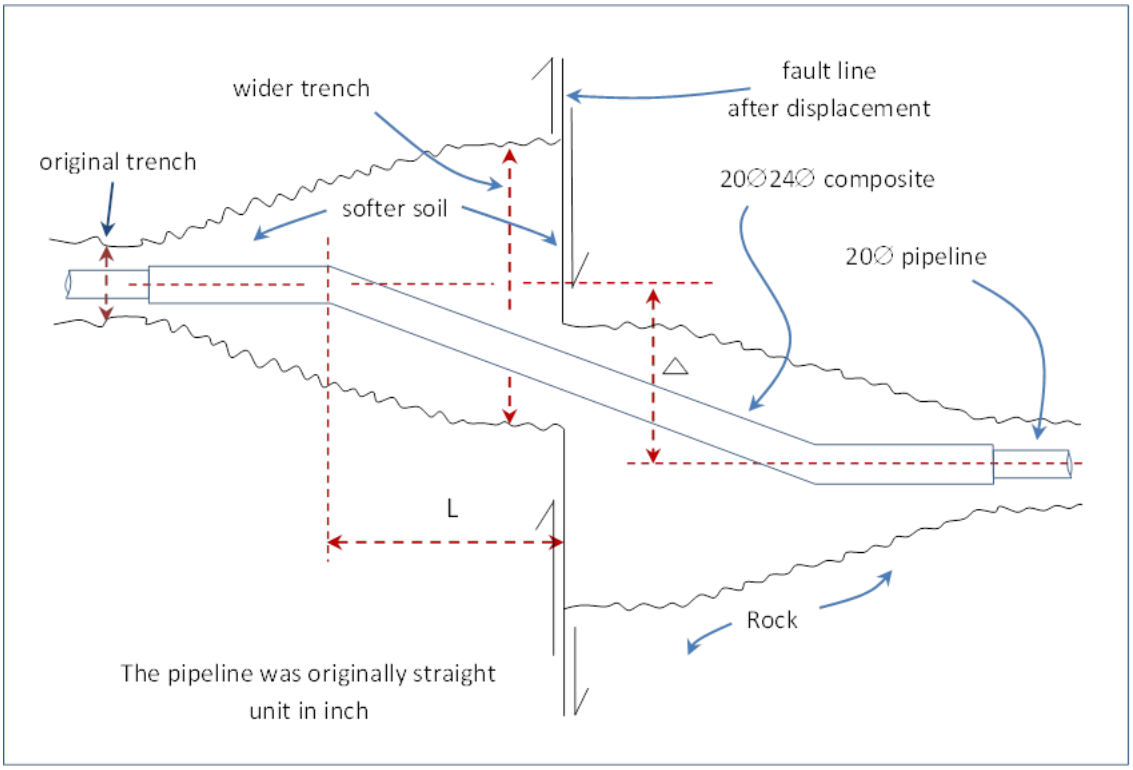

Figure 2.4 The offshore pipeline due to earthquake fault

(Marshall, 2004)

Luo, Pi, Gao, Bradford, & Hui (2015) also studied longer-term behavior and stability for concrete-filled steel tubular structures. They studied the effect of creep and shrinkage in concrete core in-plane deformation, internal forces, and in-plane buckling loads, checked the adequacy, and verified the FE results.

Using this literature, the numerical calculations are provided in chapter 3 as stated in the objective.

2.3 Portland Cement Grout in Double-wall Pipe

Double-wall composite, steel-concrete-steel tubular axial loading has been widely studied by many researchers. Tao et al. (2004) performed several concretes filled double skin steel tubular stub column tests and some of the test results are used to validate ABAQUS finite

element analysis results in this research. Hu and Su (2011), Pagoulatou et. al (2014), and Liang (2017) also performed FE analysis on concrete-filled double-wall steel tubular stub columns.

This literature will be used for the FE analysis verifications. It is crucial to verify the validity of FE analysis results.

The strain value of concrete, ε'_c, is taken as 0.003, and the Poisson ratio of 0.2 is used. Thang, Marshall, Brake, & Adam (2016) at Lamar University research used a Poisson ratio of 0.18. Different researchers have used strain values from 0.002-0.003. However, the strain value of 0.003 is selected in this research and it gives a better result than lower strain values.

Mander et al. (1988) suggested a confined concrete stress-strain curve using equations 2.4 and 2.5.

$$f'_{cc} = f_c + k_1 f_1 \quad (2.4)$$

$$\varepsilon'_{cc} = \varepsilon'_c\left(1 + k_2 \frac{f_1}{f_c}\right) \quad (2.5)$$

where,

f'_{cc} = confined concrete compressive strength

f_c = unconfined concrete cylinder compressive strength

ε'_{cc} = the confined strain corresponding to f'_{cc}

The lateral pressure coefficient, k_1, and k_2 are taken as 4.1 and 20.5 respectively based on test results from Richart et al. (1928). The stress-strain curve of confined concrete is shown in Figure 2.5.

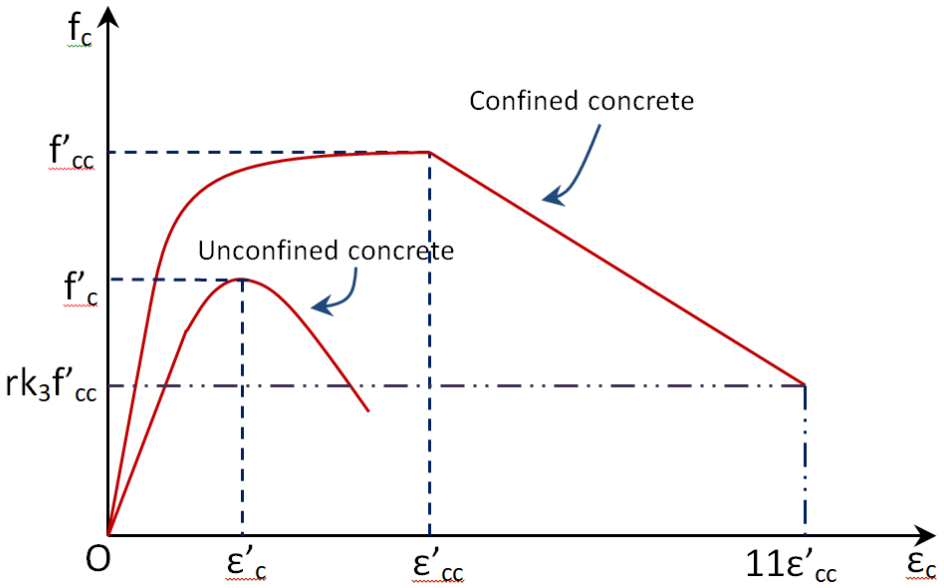

Figure 2.5 Confined and unconfined concrete stress-strain curve

(Mander et al.,1988)

The lateral confining pressure, f_1, is given by Hu and Su (2011) as

$$f_1 = 8.525 - 0.166\left(\frac{D_o}{t_o}\right) - 0.00897\left(\frac{D_i}{t_i}\right) + 0.00125\left(\frac{D_o}{t_o}\right)^2 + 0.00246\left(\frac{D_o}{t_o}\right) \times \left(\frac{D_i}{t_i}\right) - 0.00550\left(\frac{D_i}{t_i}\right)^2 \geq 0 \quad (2.6)$$

where,

D_o = diameter of outside tubular

t_o = wall thickness of outside tubular

D_i = diameter of inside tubular

t_i = wall thickness of inside tubular

Liang (2017) also suggested that Eq. 2.6 should be used for steel-concrete-steel sandwich short columns. Saenz (1964) suggested the nonlinear behavior of concrete by using the equation,

$$f_c = \frac{E_c \varepsilon_c}{1+(R+R_E-2)\left(\frac{\varepsilon_c}{\varepsilon'_{cc}}\right)-(2R-1)\left(\frac{\varepsilon_c}{\varepsilon'_{cc}}\right)^2+R\left(\frac{\varepsilon_c}{\varepsilon'_{cc}}\right)^3} \text{ (MPa)} \quad (2.7)$$

where $R = \frac{R_E(R_\sigma - 1)}{(R-1)^2} - \frac{1}{R_\varepsilon}$, $R_E = \frac{E_c \varepsilon'_{cc}}{f'_{cc}}$,

E_c = Modulus of elasticity of unconfined concrete

ε_c = Unconfined strain corresponding to f_c

R_E = Parameter related to the modulus of elasticity of concrete and the ratio of the confined strain ε_{cc} to the corresponding compressive strength f_{cc}

R_σ = Parameter in defining the stress-strain relationship of confined concrete

R_ε = Parameter in defining the stress-strain relationship of confined concrete

R = Parameter dependent upon R_E, $R\sigma$, and $R\varepsilon$

Hu and Schnobrich (1989) assumed $R_\sigma = R_\varepsilon = 4$. As per ACI 318, modulus of elasticity of normal weight concrete is

$$E_c = 4700\sqrt{f'_{cc}} \text{ (Mpa)} \quad (2.8)$$

The end point of confined concrete compressive stress on stress-strain curve beyond peak stress is taken as $rk_3f'_{cc}$ and the strain value at that point is $11\varepsilon_{cc}$, where the material degradation parameter, k_3, (Hu and Su, 2011) is given by

$$k_3 = 1.73916 - 0.00862\left(\frac{D_o}{t_o}\right) - 0.04731\left(\frac{D_i}{t_i}\right) + 0.00036\left(\frac{D_o}{t_o}\right)^2 + 0.00134\left(\frac{D_o}{t_o}\right) \times \left(\frac{D_i}{t_i}\right) - 0.0058\left(\frac{D_i}{t_i}\right)^2 \geq 0; \quad (2.9)$$

The reducing factor, r, is taken as unity for concrete cube strength up to 30 Mpa (Giakoumelis and Lam, 2004), 0.5 for 100 Mpa and higher strength is used (Tomii, 1991; Mursi & Uy, 2003). The reducing factor in between can be calculated by interpolation and the method is also adopted by Pagoulatou et al. (2014).

1.2 Steel Materials

Bilinear stress-strain curve as shown in Figure 2.6 is used, as adopted by Han et al. (2002).

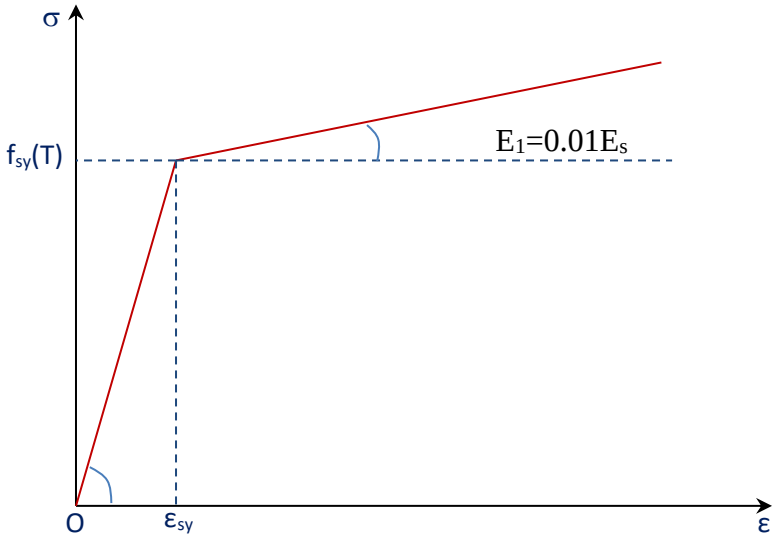

Figure 2.6 Steel bilinear stress-strain curve

(Han et al., 2006)

The elastic part of the steel is calculated using equations below for the plastic region.

$$\sigma_i = E_s(T) \times \varepsilon \quad for\ \ \varepsilon \leq \varepsilon_{sy}(T) \tag{2.10}$$

$$\sigma_i = f_{sy}(T) + E_1(T) \times \left(\varepsilon - \varepsilon_{sy}(T)\right) \quad for\ \ \varepsilon > \varepsilon_{sy}(T) \tag{2.11}$$

where f_{sy} (T) is yield strength of the steel at a given temperature T. ε_{sy} (T) given in Eq. 2.10 is the corresponding strain and it can be calculated by

$$\varepsilon_{sy}(T) = \frac{f_{sy}(T)}{E_s(T)}$$

In this research, the temperature is taken as room or normal temperature and hence there is no temperature effect considered.

Modulus of elasticity, $E_s(T)$, is taken as 200,000 N/mm^2, $E_1(T)$ is taken as 0.01 Es(T), and Poisson's ratio of 0.3 is used. The modulus of elasticity and Poisson ratio used is widely accepted and used by researchers for mild carbon steel. Normal temperature condition is used for this analysis and hence temperature does not affect the analysis results.

2.4 Misalignment Resulted from Welding

Imperfection in pipe connection has been studied by several researchers. For example, weld misalignment is a major concern in pipe connection as it can significantly affect the steel pipe capacity. Especially, in fatigue analysis, it can significantly amplify the stress concentration factor and hence it can severely impact the fatigue lives. Marshall & Thang (2014) studied the welding effect and hot spot stress on the tubular welded connection. Zhao, Lie, & Zhang (2018) studied weld misalignments such as weld misalignment with equal thicknesses and unequal diameter, and weld misalignment with unequal thicknesses and aligned inside surface. They used centerline offset (e) of 0.15T, where T is the pipe thickness. The first connection unequal thickness. An unequal diameter connection with T/8 is used to connect imperfect pipes in this research. T/8 centerline offset weld is also recommended by API 579-1/ASME FFS-1 (2007). Figure 2.7 shows a schematic diagram used in this research. Thang et al. (2022) published a part of this work in Reviews of Advanced Materials Science journal.

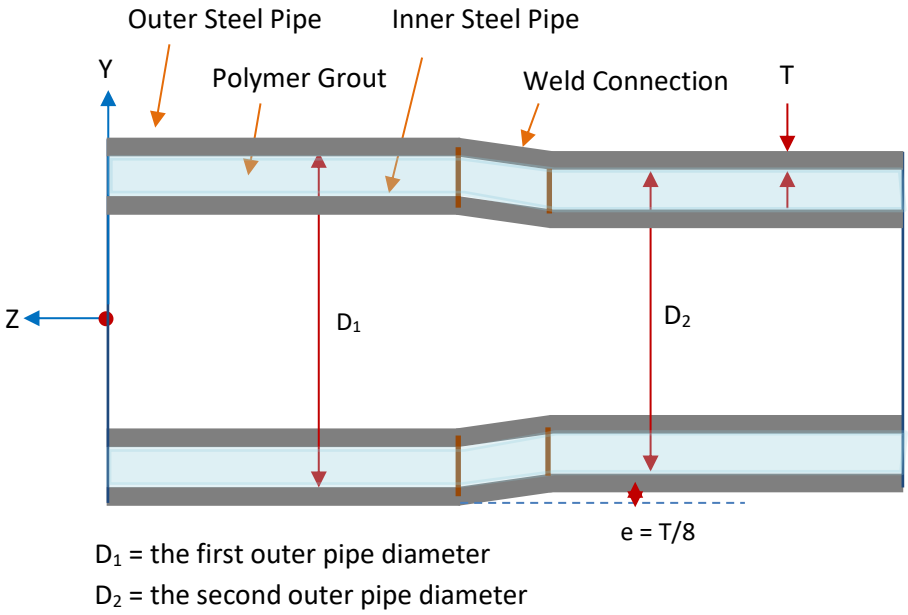

Figure 2.7 Tubular weld misalignment with weld offset

2.5 Wrinkling in Tubular Pipe

Wrinkles are another issue in the pipeline. They can reduce the pipe opening diameter and hence this can prevent pipe services such as pigging. Papadaki, Karamanos, Chatzopoulou, & Sarvanis (2018) studied and performed experimental work on imperfect single-wall pipe and they found wrinkles and bucking failures on the tubular beam test. Arjomandi & Taheri (2012) also studied sandwich pipes that Marshall (2004) invented, with polymer materials grouted for deepwater on the effect of core ratio, polymer stiffness to steel's stiffness ratio of the composite pipe. Their studies results show wrinkles on the compression side of the sandwich pipe. Uckan et al. (2015) studied a single-wall pipeline crossing a fault and using FE analysis model. Figure 2.8 shows a 2.2m diameter crossing a fault plane that failed by buckling and wrinkling.

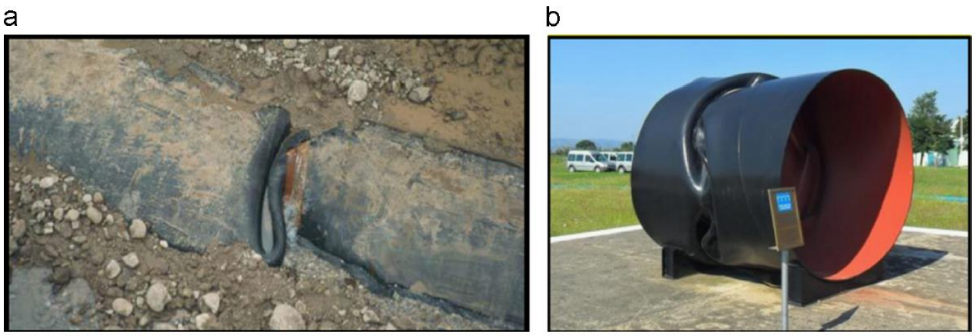

Fig. 1. (a) Wrinkling of a 2.2 m diameter steel water pipe at a fault crossing in Kullar, Izmit in the 1999 Kocaeli Earthquake [6]; (b) a close up view to the wrinkled pipe in Kullar (Uckan, E.).

Figure 2.8 Wrinkling of a tubular pipe at a fault crossing

(Uckan et al., 2015)

Barnes, Hejazi, & Karrech (2018) studied the instability of mechanically lined pipelines under large deformation shown in Figure 2.9 using the FE analysis method. They introduced a pre-stress method to reduce pipeline wrinkling.

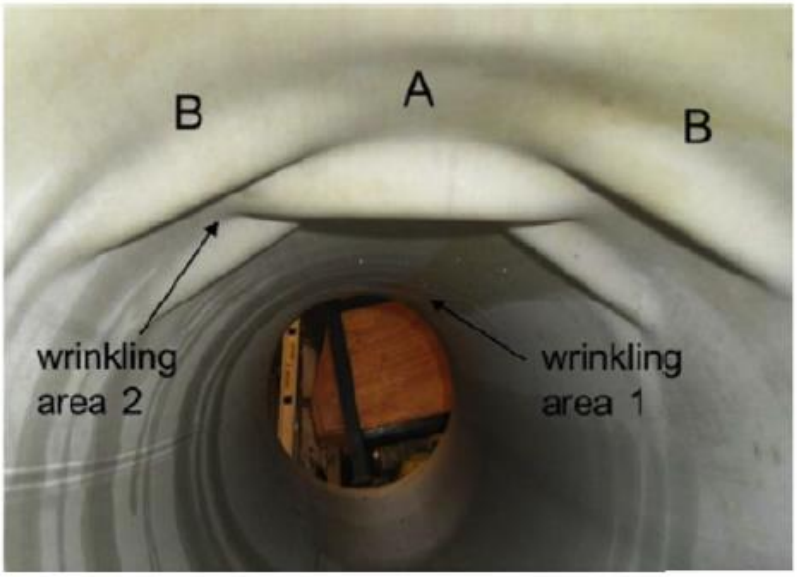

Figure 2.9 Test results of a pipe showing wrinkles

(Barnes, Hejazi, & Karrech, 2018)

The objective of this research is to eliminate wrinkles in the single-wall pipe such as this by using SPS double double-wall composite pipe with polymer grout in the annulus.

2.6 Pipe Ovalization

Buried pipeline plastic ovalization should be limited. It is because excessive ovalization could hinder passage of devices in the pipe such as pigging. Ovalizaion can cause large strain in plastic which can eventually cause fracture. In addition, large out-of-roundness can cause issue with girth welding. Different codes provide different method of ovality calculations and limits. API RP 1111 gives the ovality limit, δ, as

$$\delta = \frac{D_{max} - D_{min}}{D_{max} + D_{min}} \tag{2.12}$$

where

D_{max} = the maximum diameter at any given cross-section

D_{min} = the minimum diameter at any given cross-section

As per the API Specification 5L, out-of-roundness for pipe except end is 2% and pipe end is 1.5% for pipe diameter 50.8cm (20 inches). The ovality issue occurs within the pipe, not the end. Thus, the larger ovality of 2% is applicable.

Ovality limit stated in (DNV-OS-F101, 2013) is 3%. The equation to calculate ovality, f_0, is:

$$f_0 = \frac{D_{max} - D_{min}}{D} \tag{2.13}$$

The strain limit is taken as 2%. (DNV-OS-F101, 2013; ASCE, 2005).

Fatigue and fracture of the pipeline can be a major concern where the pipeline experience free span vortex-induced vibration and cyclic thermal loading (Bai and Bai, 2014). Berardo et al. (2000) also stated that longitudinal ductile fracture propagation can be one of the worst failures a pipeline can experience in a pipeline life span. However, Mohr (2007) stated that pipe bend testing results show buckles on the compression side rather than fracture.

The use of SPS double double-wall composite pipe in this research is to enhance and improve ovality in the single-wall pipe.

2.7 Strain Limit

Normal strain, ε, under axial loading (Beer, Johnston, Jr., & DeWolf, 2006) is given:

$$\varepsilon = \frac{\Delta l}{L} \tag{2.14}$$

where, Δl is the deformation, and L is the length

Marshall (2004) stated that pipes that are not subjected to elastic local buckling (D/t <60), the critical strain ε_{cr} may be calculated as

$$\varepsilon_{cr} = 0.5\frac{t}{D} \tag{2.15}$$

where t is the thickness, and D is the diameter of the tube.

For the pipe-in-pipe deepwater flowlines, greater thickness, higher strength steel (up to 490 MPa), and lower diameter/thickness ratio conspire to make tensile fracture governed. Here, biaxial stress and softened heat-affected zones exacerbate the problem of strain-based design (Mohr, 2007). The strain limit of 2% is suggested by API RP 1111 (1999) and the ASCE (2005). Liu, Liu, and Zhang (2009) suggested a strain limit of 2% for the inner flow line and up to 4% for the outer jacket. They documented ovality limits and ranges acceptance by different industry code in Table 2.2.

Table 2.2. Single-wall pipe ovality limit
(Liu et al., 2009)

Criteria	Ovalization Limit/%
CSA-Z662-07 App.C	3.0(6.0)[a]
DNV-OS-F101 (2000)	3.0
API 1111-1999	5.5 ~ 6.2
Murray et al. (Murray, & Bilston, 1992)	4.3 ~ 6.5[b]

[a] Number in brackets indicates upper bound of behavior if it can be demonstrated that the behavior does not affect pipeline operation or maintenance or promote failure.

[b] Ovality which produces the yield level hoop stresses in the pipe, assuming a yield strength of 480 MPa and a wall thickness of 10 mm.

Due to wrinkles in the pipe, the single-wall pipe experiences higher strain. The introduction of SPS double-wall composite pipe is expected to reduce the strain as it no longer has wrinkles. Hence the double-wall composite pipe can accommodate a larger displacement.

2.8 Fracture and Crack Propagation

Many researchers have studied fracture in the steel. Crack propagation in steel pipe can be catastrophic. Demofonti & Spinelli (2011) studied short crack and long crack of anthropogenic carbon dioxide pipeline shown in Figure 2.10. In case of a leakage, due to sudden pressure loss in the pipe there is a considerable temperature drop in the area. As a result, the pipeline may show brittle behavior and experience high residual stress which causes the leak to break and introduce fracture propagation.

Figure 2.10 Fracture and crack propagation of pipelines

(Demofonti & Spinelli, 2011)

Marshall, Thang, & Brake (2014) studied fracture propagation of a concrete beam. They found that crack in concrete is more like a heated affected zone of welded steel. Marshall (1990) also explained about fracture control procedures for deepwater offshore towers.

Internal pressure in the pipe causes high tensile stress in the pipe and hence pipe fracture can occur. Fracture normally orient in the axial direction because they grow perpendicular to the direction of the largest tensile stress which is usually the hoop stress (Baker Jr & Fessler, 2008). Figure 2.11 shows fracture in the pipe due to corrosion. The SPS double-wall composite pipe is expected to mitigate or eliminate the crack issue in the single-wall pipe.

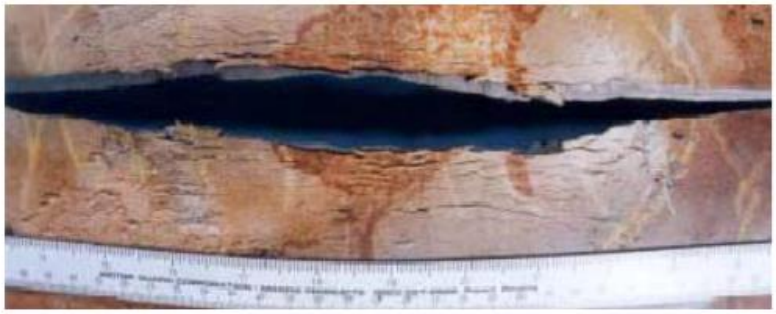

Figure 3.14 – *SCC colony on a large-diameter, high-pressure transmission gas pipeline (Source: http://www.corrosioncost.com/pdf/gasliquid.pdf)*

Figure 2.11 Crack due to internal pressure of the pipe with corrosion in the pipe (Baker Jr & Fessler, 2008)

2.9 Plastic Deformation of a Simply Supported Beam

In collapse mechanism of a beam, 3 hinges are formed – at two ends and at a mid-point of a beam. Hinge angle at mid-point is 2 times hinge angles at ends of the beam. Figure 2.12 shows collapse mechanism of a beam.

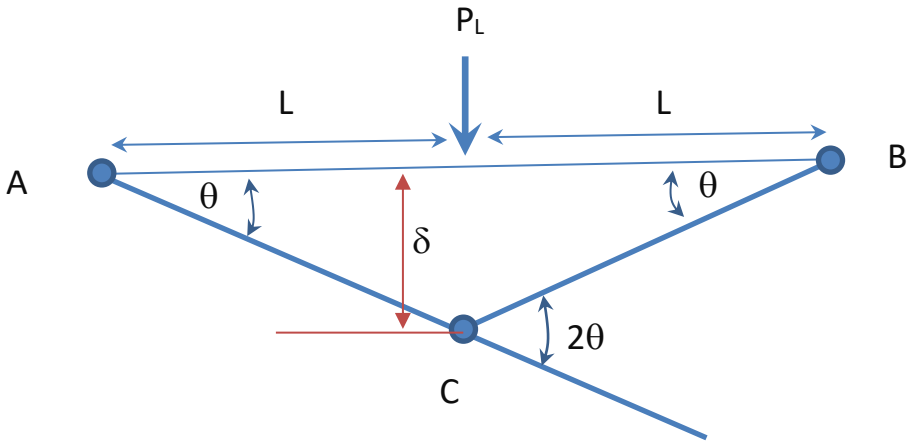

Figure 2.12 Collapse mechanism of the simply supported beam

The work done by the load P_L during plastic collapse is $P_L\delta$ (Nash, 1998). The fully plastic moment M_p develops at the hinge point B and C. Work-energy balance requires that for the beam collapse load, P_L is

$$P_L \delta = [M_P \theta]_A + [M_p(2\theta)]_C \quad (2.16)$$

$$P_L(L/2\ \theta) = 3M_p \theta$$

Hence, $P_L = 6M_p/L$

where δ = deflection, and θ = rotation at plastic hinge.

In simply supported beam bending, plasticity occurs at the middle of the pipe and a hinge is formed before the beam fails. Beam bending test in the air have failures similar to this literature.

2.10 Clay Foundation and laterally loaded pile

Reese & Impe (2011) stated that soft clay is less than 1000 psf with strain value of 0.02, and medium clay is between 1000 psf to 2000 psf with strain value of 0.01. Reese at el. (2006) stated that soft clay is between 250 psf to 500 psf with strain value of 0.02, and medium clay is between 500 psf to 1000 psf with strain value of 0.01. Meyer & Reese (1979) recommended strain values for different types of clay and they are shown in Table 2.3.

Table 2.3 Recommended Values for ε_{50}

Consistency of Clay, psf	**Undrained Shear Strength kPa**	**ε_{50} (%)**
250 – 500	> 12	2
500 - 1000	12 - 24	1
1000 - 2000	24-48	0.7
2000 - 4000	48-96	0.5
4000 - 8000	96-192	0.4
	< 92	

Matlock (1970) stated, for most clays E_c/c fall between 50and 200, and ε_c may be assumed between 0.005 and 0.02. E_c is secant modulus of elasticity of the clay. Matlock also states that smaller ε_c are applicable to brittle or sensitive clays and the larger to disturbed or remolded soil or unconsolidated sediments, and an intermediate value of 0.01 is probably satisfactory for most purposes.

The differential equation of the deflection curve of a beam supported on an elastic foundation derivation was provided by Hetenyi (1946) and the equation is given as

$$EI\frac{d^4y}{dx^4} + K_h y = 0 \qquad (2.17)$$

Where EI is the flexural stiffness of the pile, x is length along the pile, y is the lateral deflection of the pile, and K_h is the modulus of the subgrade reaction.

The soil resistance per unit length of the pile, *p*, is given by Broom (1964) is

$$p = K_h\, y \qquad (2.18)$$

The laterally loaded single and SPS double-wall composite pipes in this research are embedded in the soft and medium clay.

2.11 SPS Double-wall Composite Pipe

To eliminate the issues found in the single-wall steel pipeline or to significantly improve it, Thang, Marshall, & Hui (2020) conducted research and performed FE analysis at the University of New Orleans. They studied double-wall composite pipes, bonded and unbonded between steel and polymer behavior, and enhanced composite pipeline in clay. Arjomandi & Taheri (2012) also studied SPS sandwich composited pipe, investigating different stiffnesses of the polymer grout and wrinkles.

2.12 Summary of the Literature

In this research, the pile displacement and pipeline due to the earthquake fault in the literature are simulated as a pipe/pile embedded in a block of clay, and the top of the pipe is laterally displaced. The displacement represents half of the pipeline displacement. Double-wall steel-concrete-steel is also modeled in FE software and the analysis results are used for the FE analysis results verifications. A cone is placed between the two pipe connections to simulate the welding misalignment in the literature and simply supported pipe bending analysis is performed. Then, the analysis result is compared against the intact composite pipe. The welding effect is studied on both single and SPS double-wall composite pipes to see wrinkling, ovalization, and the strain effect. Different loadings methods are applied for simply supported beam analysis in the air for four-point bending and rotation. Rotational loading is not possible on soft polymer as the loading point at the end of the beam can be distorted due to the softer polymer grout in the annulus.

CHAPTER 3 DESIGN CALCULATIONS OF PLASTIC HINGE ANGLE AND OFFSET FAILURE

This part of the research verifies the offsets calculation of the single-wall composite pipe using available literature. Marshall (2004) calculated offsets for the single and double-wall pipes at the earthquake fault plane using a rigid plastic model. The calculations in this chapter are compared against the literature.

3.1 Numerical Calculation of Plastic Hinge Angle and Offset Failure

The numerical calculations are shown in Table 3.1. This shows the detailed calculation of the hinge angle and offsets failure and comparison with Marshall (2004). Case 2 of Figure 2.3 is used in the verification calculation.

Table 3.1 Calculation of plastic hinge angle and offset failure

Notation	Description	Single-wall tubular			
		Thang	Marshall	Thang	Marshall
D (in)	Tubular Diameter	20.00		20.00	
t (in)	Wall Thickness	0.50		1.00	
σ_y (ksi)	Allowable Stress	50.00		50.00	
E (ksi)	Young's Modulus	29000.00		29000.00	
I (in^4)	Moment of Inertia	1456.86		2700.98	
ϕ'_y (in^{-1})	$2.54*\sigma y/(D*E)$	0.000219		0.000219	
Z_p (in^3)	$(D_o^3-D_i^3)/6$	190.17		361.33	
M_{fp} (kip-in)	σ_y*Z	9508.33		18066.67	
c (ksi)	-	0.0083		0.0083	
Q (kip/in)	12 c*D	2.00		2.00	
L (in)	$\sqrt{(8*M_{fp}/Q)}$	195.02		268.82	
L_b (in)	$122*(t/D)^{2.5}$	0.0121		0.0682	
L_p (in)	0.16 L	31.20		43.01	
ε_{cr}	0.5 t/D	0.0125	0.0125	0.025	0.025
ϕ_{cr}	$2\ \varepsilon_{cr}/D$	0.00125		0.0025	
θ_p (Rad.)	$(\phi_{cr}+\phi'_y)*(L_p+L_b)$	0.046		0.117	
θ_p (Deg.)		2.63	2.50	6.71	6.20
$\Delta_{elastic}$ (ft)	$0.7*M_{fp}*L^2/EI$	0.499		0.972	
Δ (ft)	$\Delta_{elastic} + \theta_P*L$	1.245	1.300	3.596	3.400

The calculation results above are relatively close to that of Marshall's, 4% to 8 % off for plastic hinge rotation and 4% to 5% off for the offset failure.

CHAPTER 4 NUMERICAL ANALYSIS AND VALIDATION

In this chapter, portal tubular beams are laterally loaded in the presence of axial loads using FE analysis. This represents portal piling in offshore structures. The buckling failure FE analysis results are compared against the experimental results. The FE analysis results are used to validate the experimental results. The mesh size effects are also studied. The benefits of hollow pipe in place of solid rods are also included.

Deformable, 3D solid elements are used in the pipe model. Due to having curved behavior in the pipe, the deformable solid elements can also be taken as shell elements. Mesh element types used are C3D8R, an 8-node linear brick, reduced integration, and hourglass control.

4.1 Single-wall Pipe

Five series of the portal beam, namely, PA, PB, PC, and PD are tested using FE analysis, and the results are compared with that of Sherman's experimental results at the University of Wisconsin – Milwaukee in 1980-81. In the model, one end is fixed (Encastre) and the other end is free.

The beam is partitioned into 3 parts. Two parts near the fixity, 3 inches each. Very fine meshes are used for the section at fixity, the same size as the tube's thickness. The middle section has a mesh size two times the thickness, and the free end mesh is ten times coarser. This is to save analysis time and the beam testing result is governed by buckling at the fixed end. Fine mesh 3 inches from the fixpoint is sufficient for result accuracy. More detailed information such as section properties, the material properties are also provided. The beam model is shown in Figure 4.1.

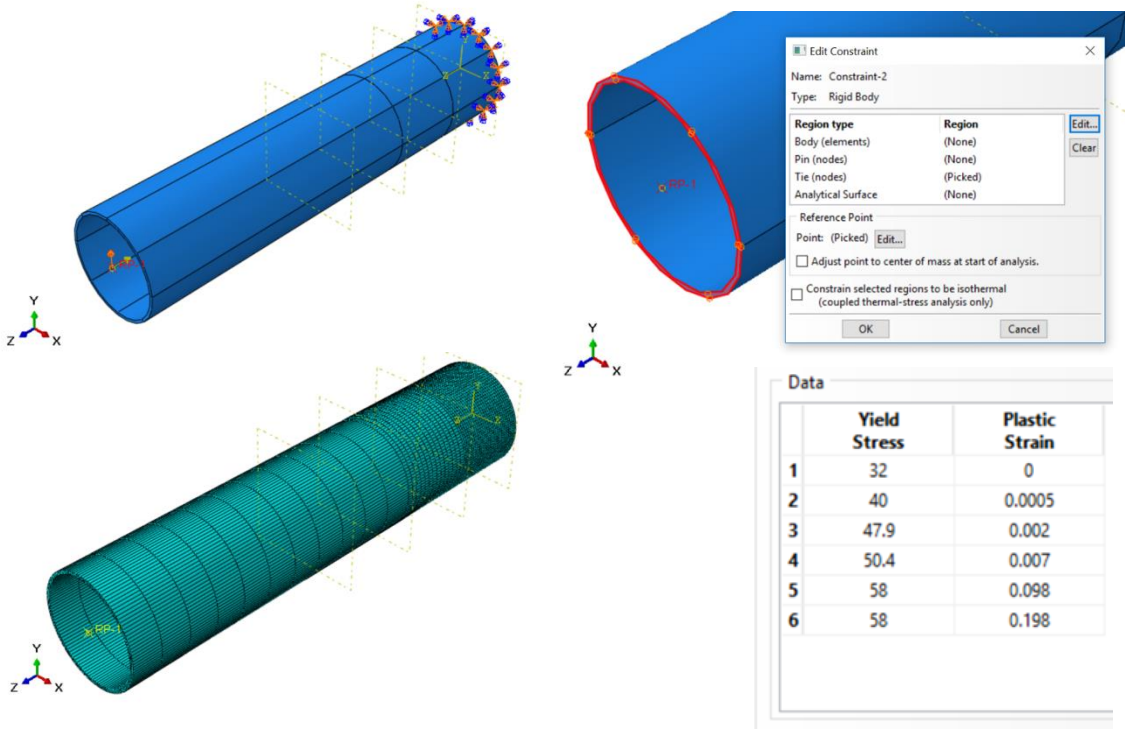

Figure 4.1 FEA model – boundary condition, mesh, and plastic strain

A reference point was created at the center of the tube at the tip. The section of the tip was tied to the reference point using the 'Rigid Body' constraint type. Lateral displacement and axial loads of different tests are applied on the reference point.

4.2 PA Series Test

The stress-strain curves used in the analysis are shown in Table 4.1.

Table 4.1 Stress-strain data for difference steel tube sections

4 Inch Tube		4.5 Inch Tube		6 Inch Tube	
Stress (ksi)	Strain	Stress (ksi)	Strain	Stress (ksi)	Strain
0.0	0.0000	0.0	0.0000	0.0	0.0000
32.0	0.0000	20.0	0.0000	40.0	0.0000
40.0	0.0005	36.0	0.0005	52.0	0.0003
47.9	0.0020	42.0	0.0020	53.0	0.0020
50.4	0.0070	43.0	0.0060	54.0	0.0060
58.0	0.0980	51.0	0.1000	69.0	0.1000
58.0	0.1980	51.0	0.2000	69.0	0.2000

Plot of the stress strain curves are shown in Figure 4.2. The data in Table 4.1 are used to plot the curves.

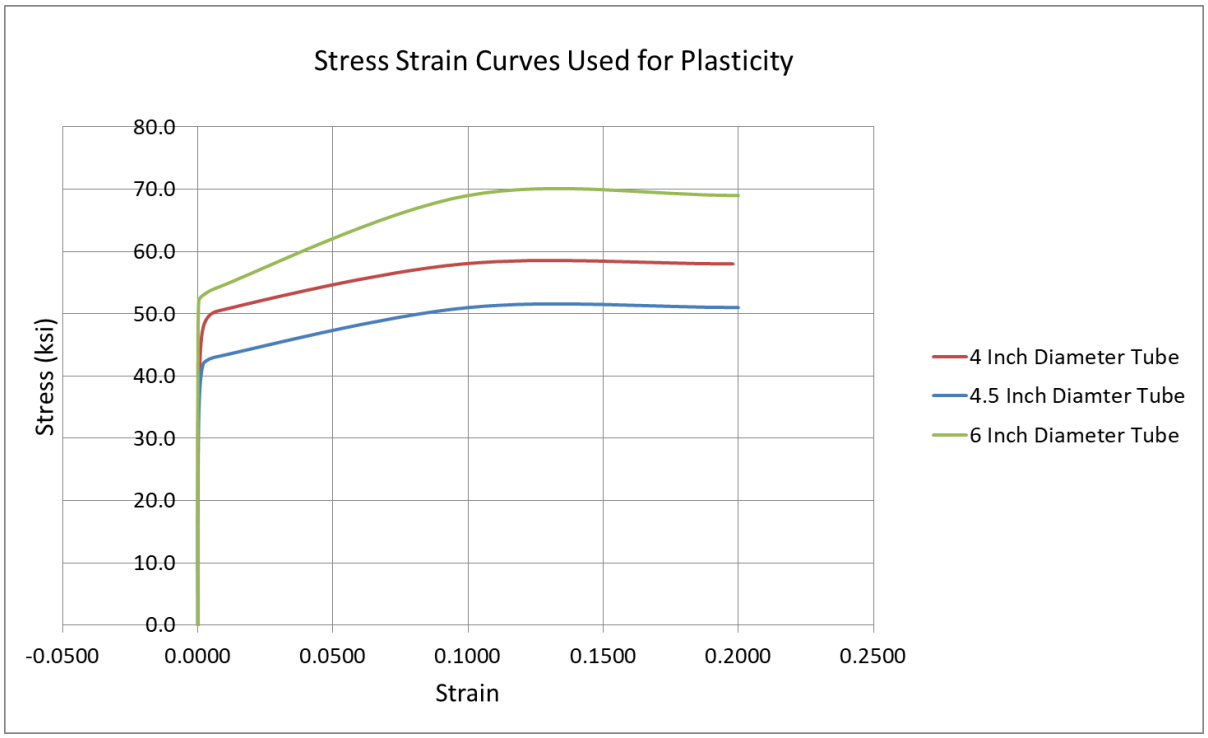

Figure 4.2 Plot of plastic stress-strain curve

The beam is a steel pipe, and the section properties are shown in Table 4.2.

Table 4.2 Section properties and loads

Code	Lateral Displacement (in)	Axial Load (kip)	Young's Modulus (ksi)	Poisson's Ratio (-)	Diameter (in)	Thickness (in)	Length (in)
PA-1	3.0	0.0	29000	0.3	4.0	0.106	18
PA-2	2.0	10.7	29000	0.3	4.0	0.106	18
PA-3	1.6	21.5	29000	0.3	4.0	0.106	18
PA-4	1.5	32.2	29000	0.3	4.0	0.106	18
PA-5	1.2	42.9	29000	0.3	4.0	0.106	18

The stress analysis results are summarized in Table 4.3 below.

Table 4.3 Stress Analysis Results

Code	Max. Principle Stress (ksi)	Min. Principle Stress (ksi)	Von Mises Stress (ksi)
PA-1	83.23	93.22	58.0
PA-2	83.23	93.22	58.0
PA-3	82.21	85.00	58.0
PA-4	72.06	85.80	58.0
PA-5	62.54	70.87	58.0

Plots of lateral forces against lateral displacements are shown in Figure 4.3 for all the PA portal beam series.

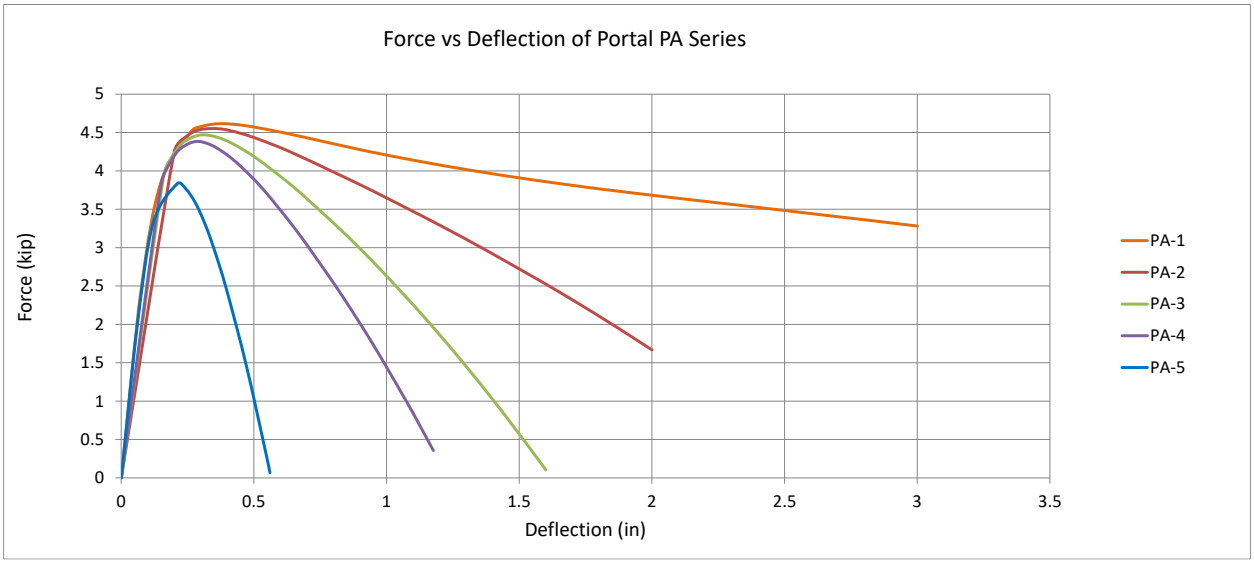

Figure 4.3 FE test results for portal PA series

Plot comparisons for each of the portal beam experimental and FE test results are shown in Figure 4.4.

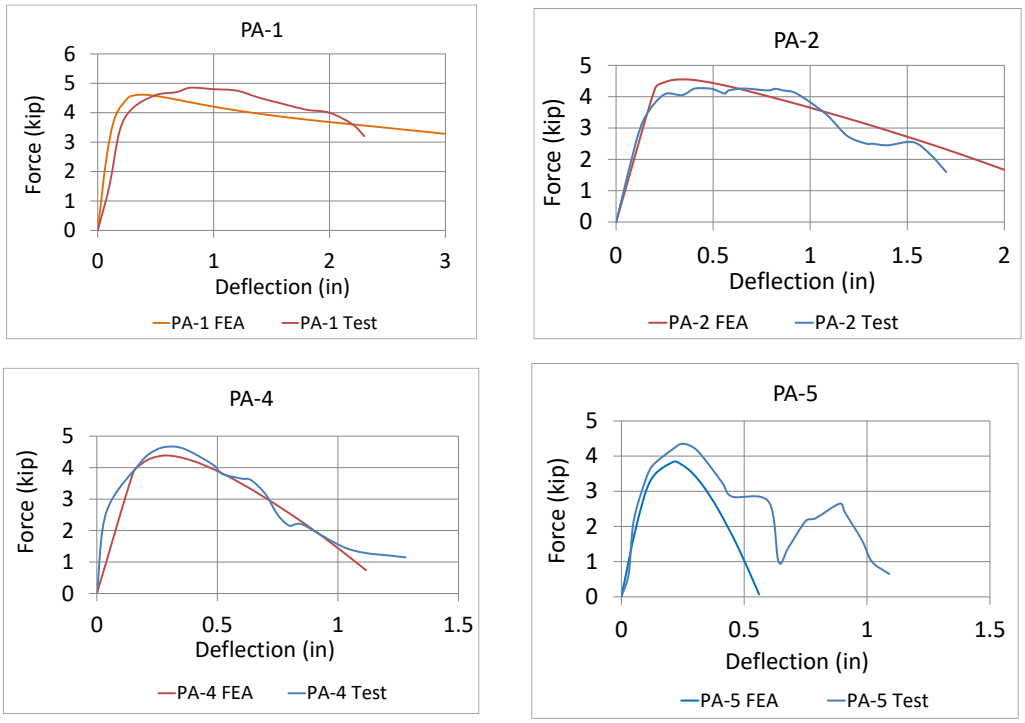

Figure 4.4 Comparison between experimental and FE test results for PA series

Figure 4.5 shows graphical analysis results of the experimental and FE analysis. Both experimental and FE analysis tubular failure patterns are found to be the same.

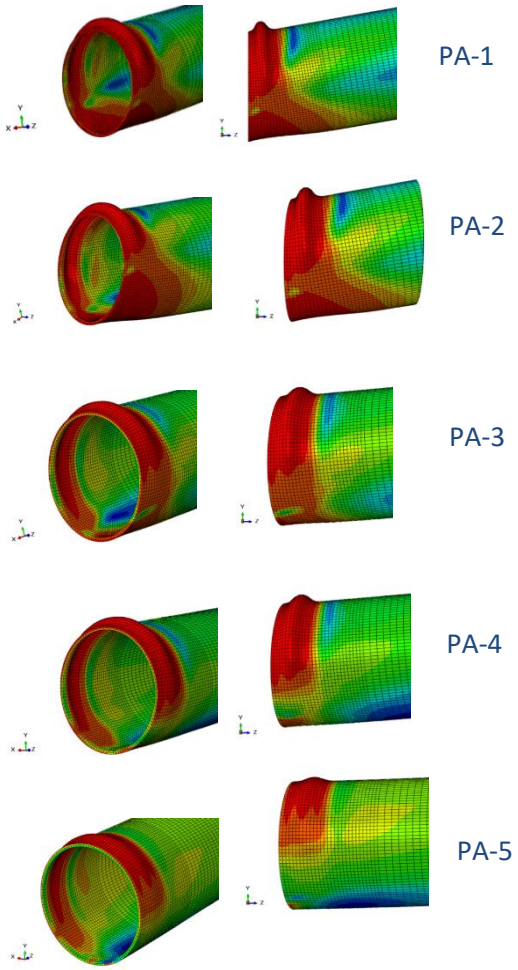

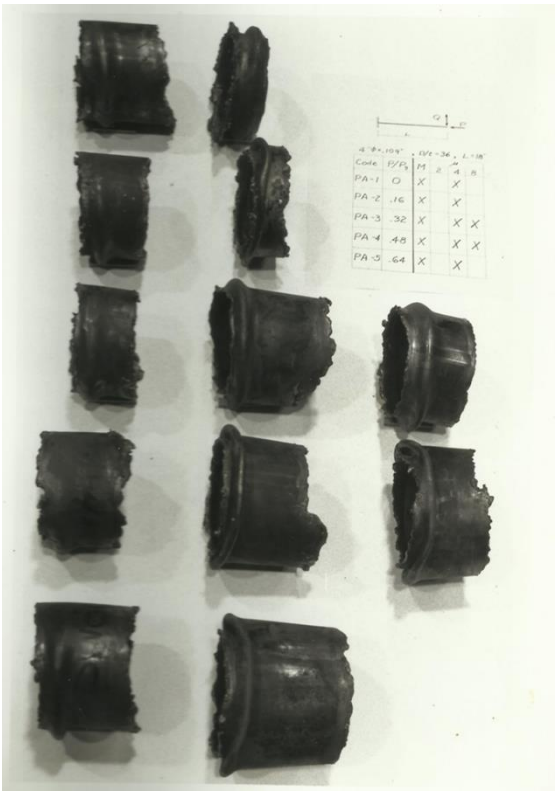

(Sherman, 1980)

Figure 4.5 FE Test results and buckles at termination of PA series tests

4.2.1 Discussion for PA Series Test

Qualitatively, FE analysis and experimental results are matching. This can be seen in Figures 4.3 and 4.4, for example. Each portal beam test comparison plot in Figure 4.4 shows that the test and FEA results are relatively close. Similar deflection can be seen as well. However, Test PA-2 and PA-5 exhibit a different load-deflection curve from the other two Tests. PA-3 experimental test result was not available. PA-1 and PA-4 tests are almost identical to FE analysis results. FE analysis uses a wall thickness of 0.106 inch which is different from the thickness in test 0.109 inch. So, having a small lesser capacity is expected. It is questionable

why experimental test PA-2 and PA-5 are behaving differently from the other two, whether material imperfection or experimental setup or both caused the behavior. On the contrary, the FE analysis has difficulty matching the plateau of the experimental results. The experimental results show the same capacity continues for certain displacement before the capacity reduces. However, the FE analysis does not exhibit this behaving. The capacity almost immediately reduces after reaching the peak load.

The failure modes of the beams from Von Mises stress result are displayed in Figure 4.6. Comparing these against the test results shows failure modes of the Test results and FEA results exhibit the same pattern. The test results show buckling of the tube very close to the fixity. In FE analysis, as the applied load increases the beam deflects larger and local buckling appears near fixity. The same buckling and buckle failure pattern can be seen in experimental analysis results, as shown in Figure 4.7.

4.2.2 Mesh Size Study

FE mesh study was also performed on portal beam, PA-4, mesh size the same as the thickness of tubular beam and mesh size two times smaller than the thickness of the tube. Mesh size which is the same as the thickness of the tube gives a sufficiently accurate result, and a finer mesh than this does not show a better result. Figure 4.6 and Figure 4.7 show the analysis results. Moreover, the analysis time takes significantly more with finer mesh and this it is not productive, and perhaps costly especially for the larger model. According to the FE analysis results, the TxT mesh used in the analysis is relatively close to the testing result. In addition, the experimental results and FE analysis failure patterns are identical. Therefore, it can be concluded that the FE analysis results are reliable.

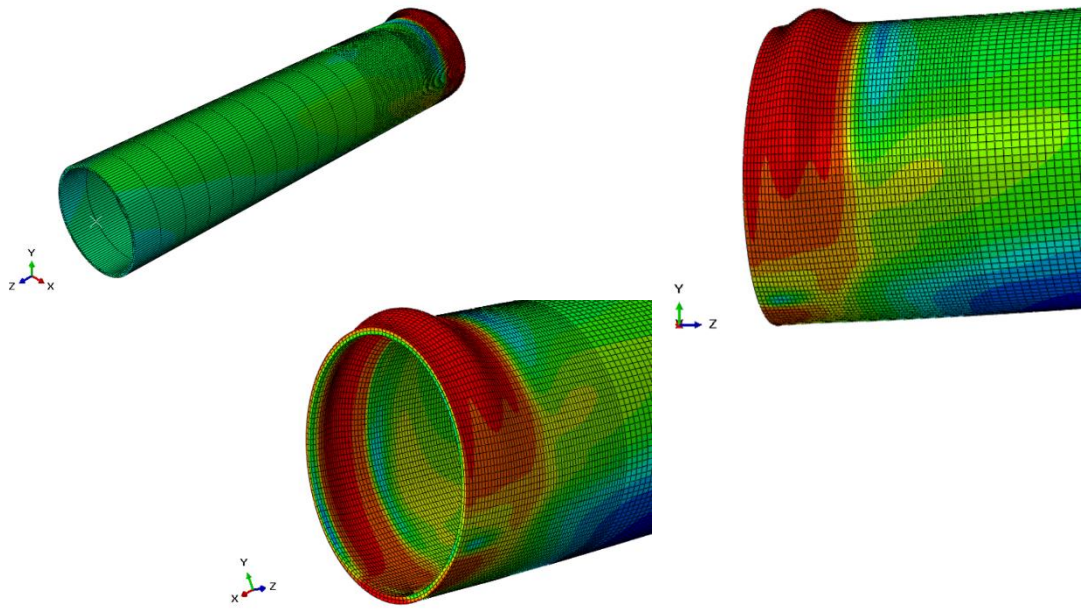

Figure 4.6 PA-4 Failure mode with finer mesh (0.053 inch mesh size)

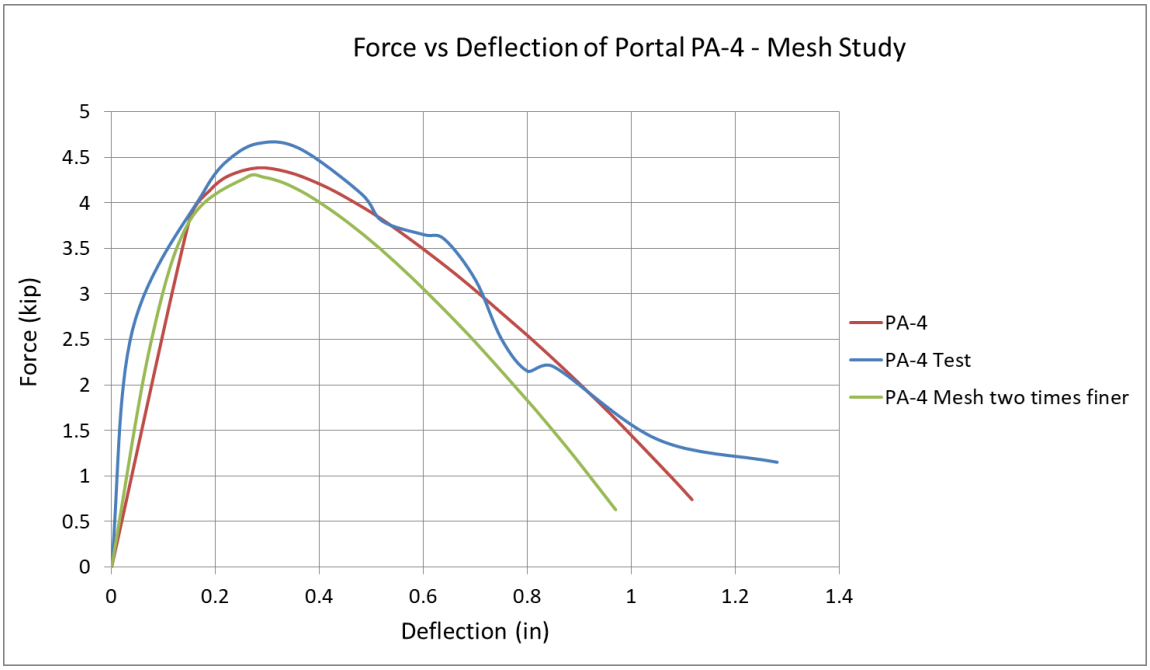

Figure 4.7 Different mesh size load-deflection plot of PA-4 portal beam

4.3 PB Series Test Results and Discussion

The beam is a steel tube, and the section properties are shown in Table 4.4.

Table 4.4 Section properties of the test

Code	Section (in)	Lateral Displacement (in)	Axial Load (kip)	Young's Modulus (ksi)	Poisson's Ratio (-)	Length (in)
PB-1	4.5" x 0.094"	6.00	0.0	29000	0.3	20
PB-2	4.5" x 0.094"	2.50	9.9	29000	0.3	20
PB-3	4.5" x 0.094"	1.25	19.7	29000	0.3	20
PB-4	4.5" x 0.094"	0.80	29.6	29000	0.3	20
PB-5	4.5" x 0.094"	0.35	39.5	29000	0.3	20

PB series FE analysis results are shown in Table 4.5.

Table 4.5 PB series FE analysis results

Code	Max. Principle Stress (ksi)	Min. Principle Stress (ksi)	Von Mises Stress (ksi)	Tresca Stress (ksi)
PB-1	80.83	86.97	51.0	58.89
PB-2	74.26	79.75	51.0	58.88
PB-3	66.08	67.62	51.0	58.80
PB-4	56.27	62.58	51.0	58.81
PB-5	45.35	58.74	51.0	54.82

Figure 4.8 shows plot of FE analysis results. Stress strain curve used for the analysis is the same as that of PA Series.

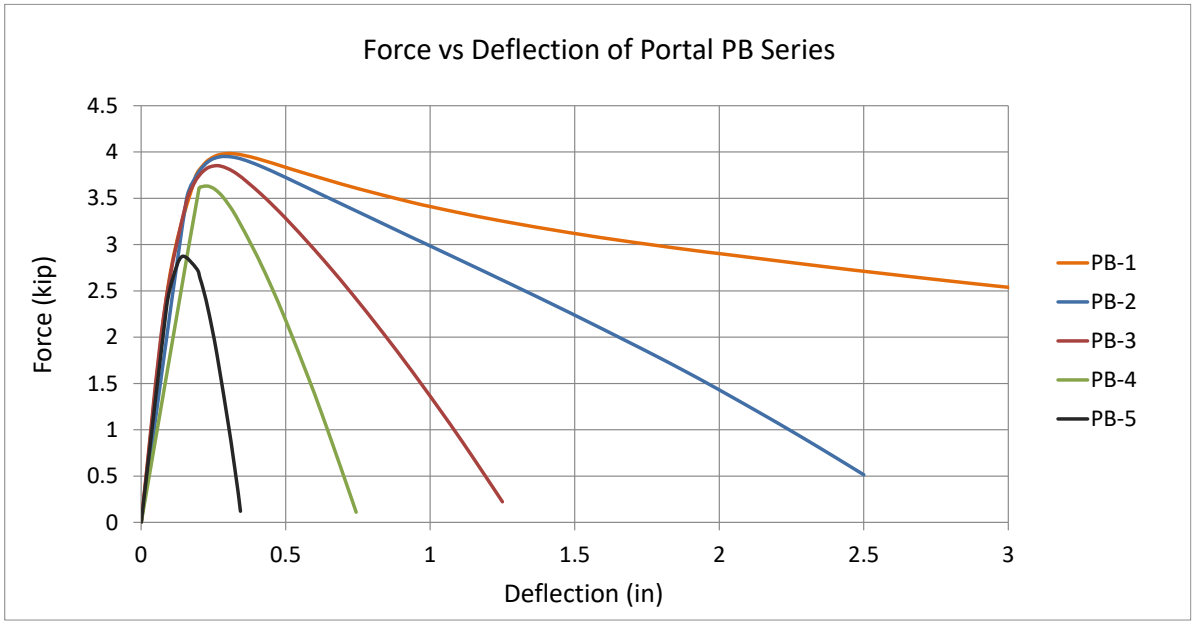

Figure 4.8 FE analysis result of PB portal series

Individual test result comparison of FE analysis and experimental results are shown in Figure 4.9. Figure 4.10 shows the FE test and experimental results comparison.

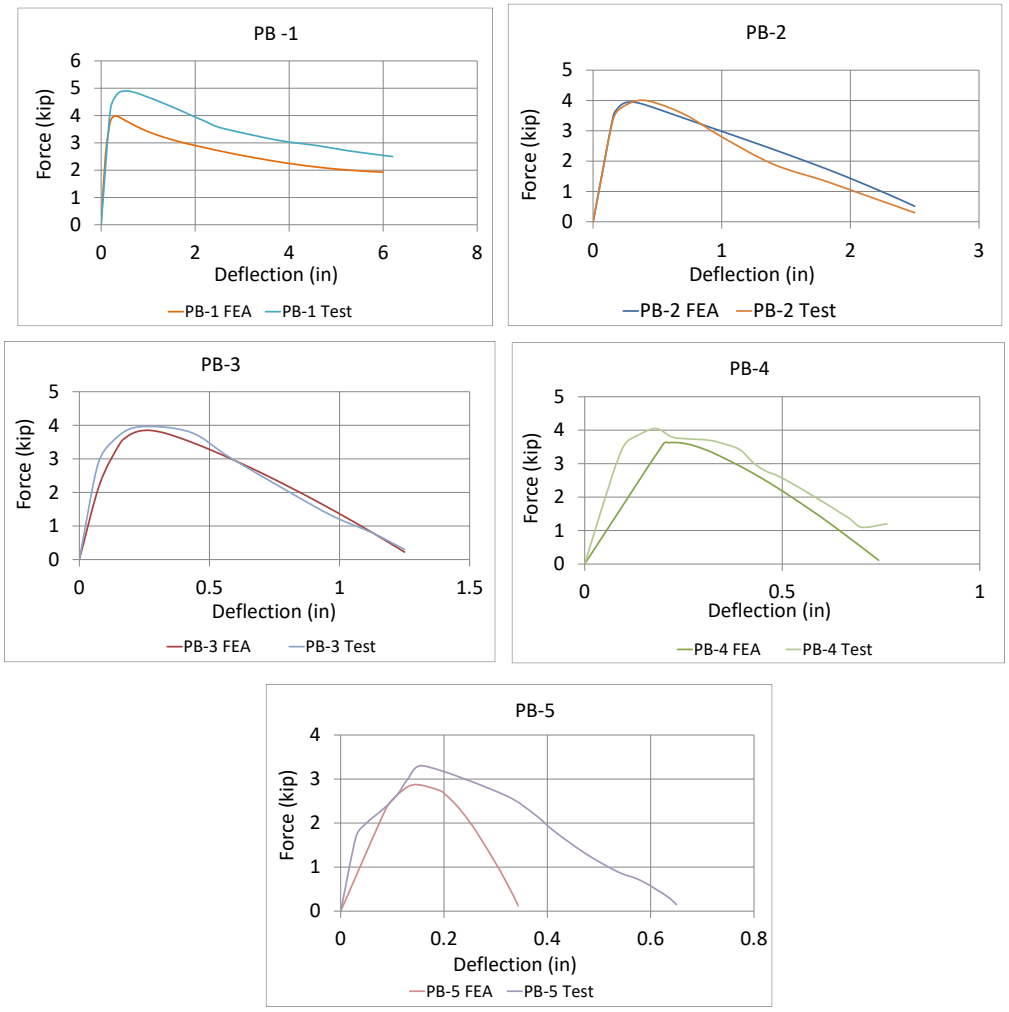

Figure 4.9 Comparison of the stress analysis results

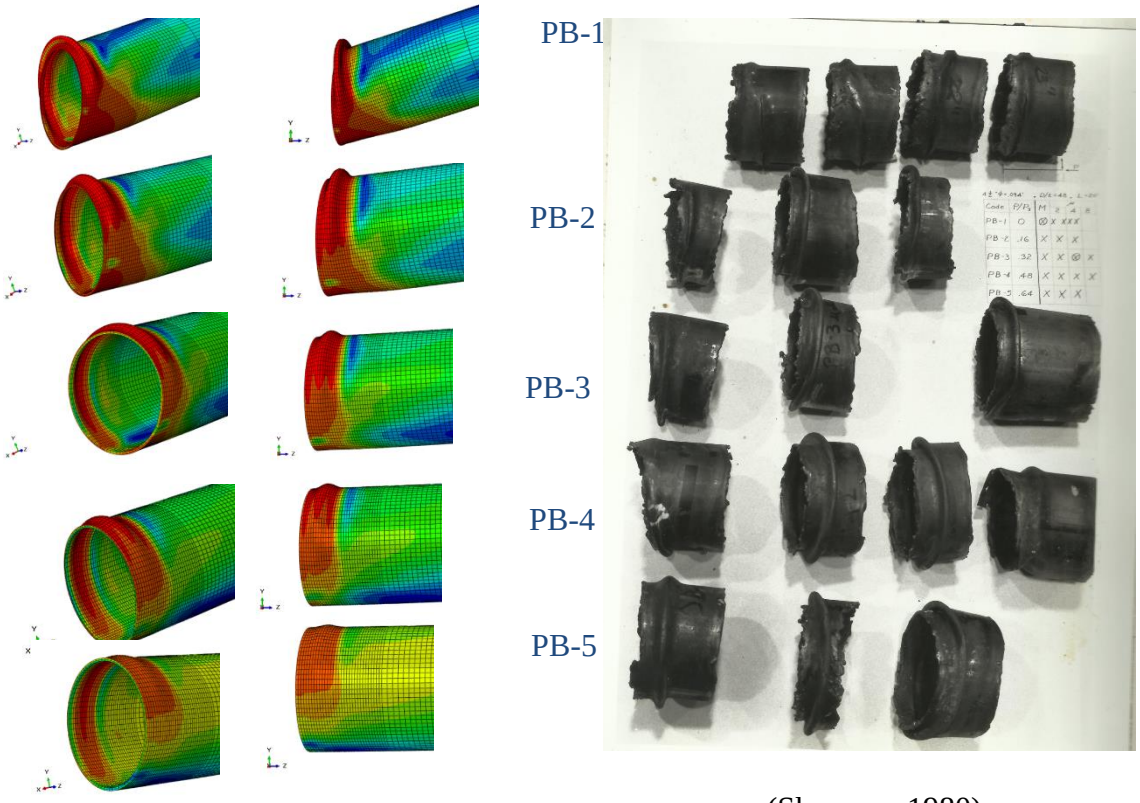

(Sherman, 1980)

Figure 4.10 Experimental local buckling failure pattern failure pattern of PB portal series experimental results

Both experimental and FE analysis results match qualitatively. The maximum capacity of principle stresses decreases from PB-1 to PB-5. Axial load from PB-1 to PB-5 increases. As axial load increases, lateral load capacity decreases. PB-2 and PB-3 load-deflection plots appear to be matching for FEA and experiment. However, experimental load capacities appear to be slightly larger in the other three PB series test results. Buckling failure for all five analysis results is the same as a test failure.

4.4 PC Series Test Results and Discussion

PC Series portal test properties, FE analysis results, comparison of FE and experimental test results, and failure pattern of FE analysis are shown in this section. However, failure modes of the actual test photos are not available for this series. Table 4.6 shows the section properties of the test for PC series. Table 4.7 shows the FE test results.

Table 4.6 Section properties of the test

Code	Section (in)	Axial Load (kip)	Young's Modulus (ksi)	Poisson's Ratio (-)	Length (in)
PC-1	4.5" x 0.094"	0.0	29000	0.3	50
PC-2	4.5" x 0.094"	9.9	29000	0.3	50
PC-3	4.5" x 0.094"	19.7	29000	0.3	50
PC-4	4.5" x 0.094"	29.6	29000	0.3	50
PC-5	4.5" x 0.094"	39.5	29000	0.3	50

Table 4.7 Portal PC series analysis results

Code	Max. Principle Stress (ksi)	Min. Principle Stress (ksi)	Von Mises Stress (ksi)	Tresca Stress (ksi)
PC-1	71.05	77.72	51.0	58.89
PC-2	70.39	65.51	51.0	58.54
PC-3	60.46	64.15	51.0	58.55
PC-4	58.47	56.59	50.9	54.31
PC-5	15.76	48.19	51.0	45.53

Figures 4.11 and 4.12 show graph of the analysis and Figure 4.13 shows the qualitative failure plot.

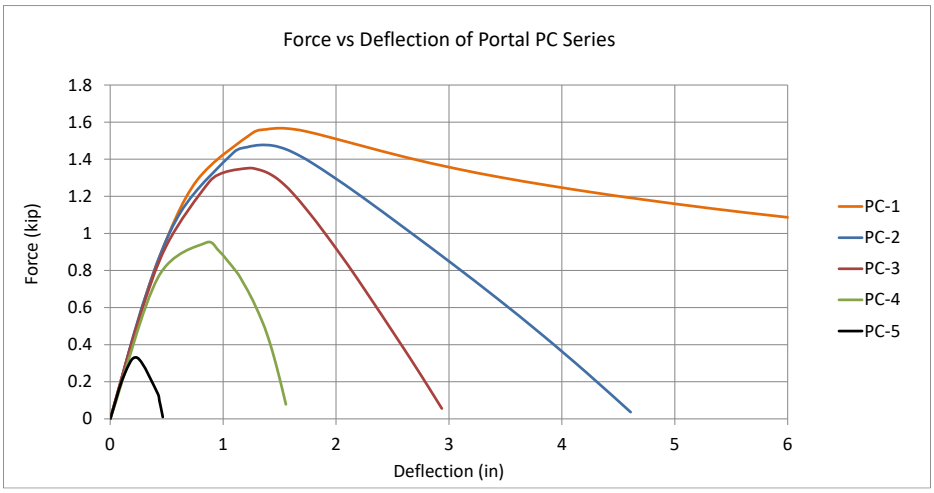

Figure 4.11 FE analysis results for portal PC series

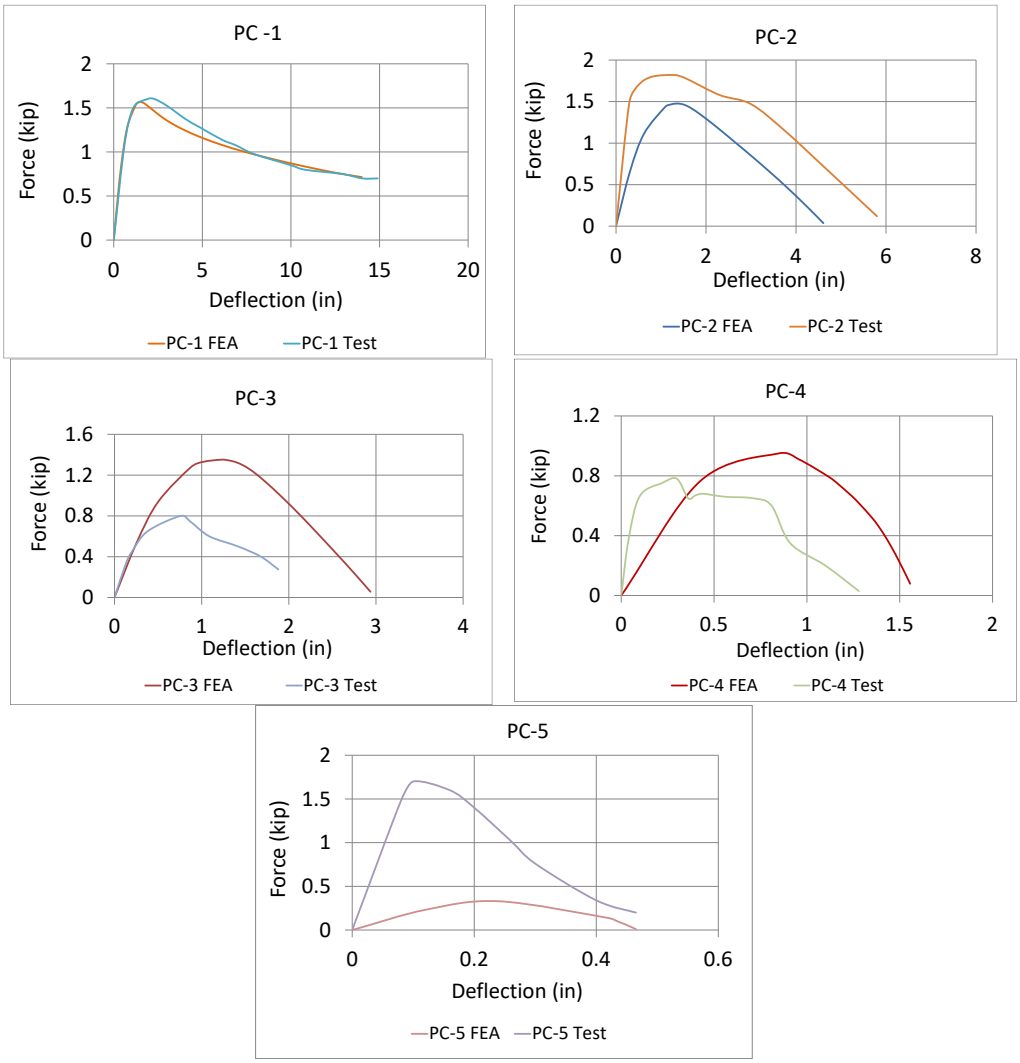

Figure 4.12 Comparison of FE and experimental analysis results for portal PC series

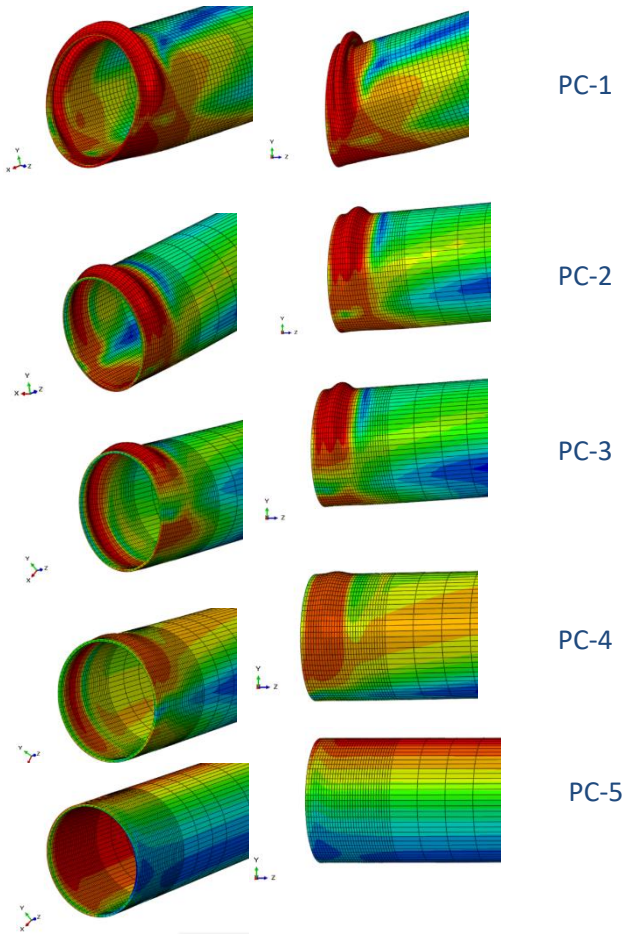

Figure 4.13 FE analysis failure pattern of portal PC series

PC-5 experimental results deviate from the rest of the PC series. It has the largest axial load and therefore it is expected that its lateral load capacity should be the least. However, this is not the case here. The reliability of the test result is questionable.

4.5 PD Series Test Results and Discussion

Section properties used for portal PD series, FE analysis results, comparison between FE, and experimental results are shown in this section. Table 4.8 shows the section properties and Table 4.9 shows the analysis results.

Table 4.8 Section properties of portal PD series

Code	Section (in)	Axial Load (kip)	Young's Modulus (ksi)	Poisson's Ratio (-)	Length (in)
PD-1	6" x 0.075"	0.0	29000	0.3	26
PD-2	6" x 0.075"	13.6	29000	0.3	26
PD-3	6" x 0.075"	27.2	29000	0.3	26
PD-4	6" x 0.075"	40.8	29000	0.3	26
PD-5	6" x 0.075"	54.4	29000	0.3	26

Table 4.9 Portal PD series FE analysis results

Code	Max. Principle Stress (ksi)	Min. Principle Stress (ksi)	Von Mises Stress (ksi)	Tresca Stress (ksi)
PD-1	65.10	76.31	64.3	70.32
PD-2	54.73	66.66	62.1	68.3
PD-3	58.18	59.93	69.0	79.45
PD-4	77.50	82.97	69.0	79.59
PD-5	69.93	81.23	69.0	79.67

Figure 4.14 and Figure 4.15 show the analysis results for PD series.

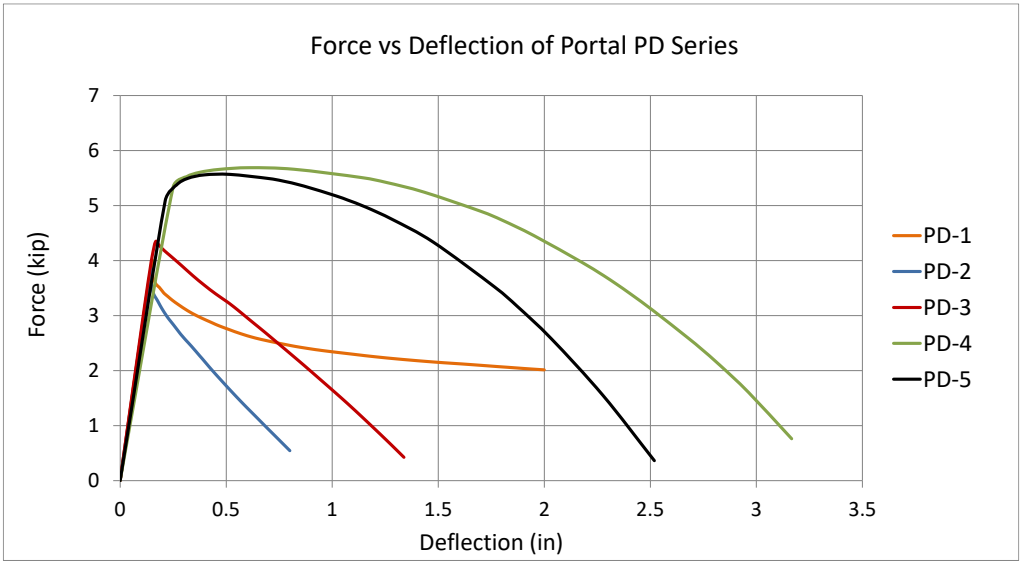

Figure 4.14 Experimental results of portal PD series

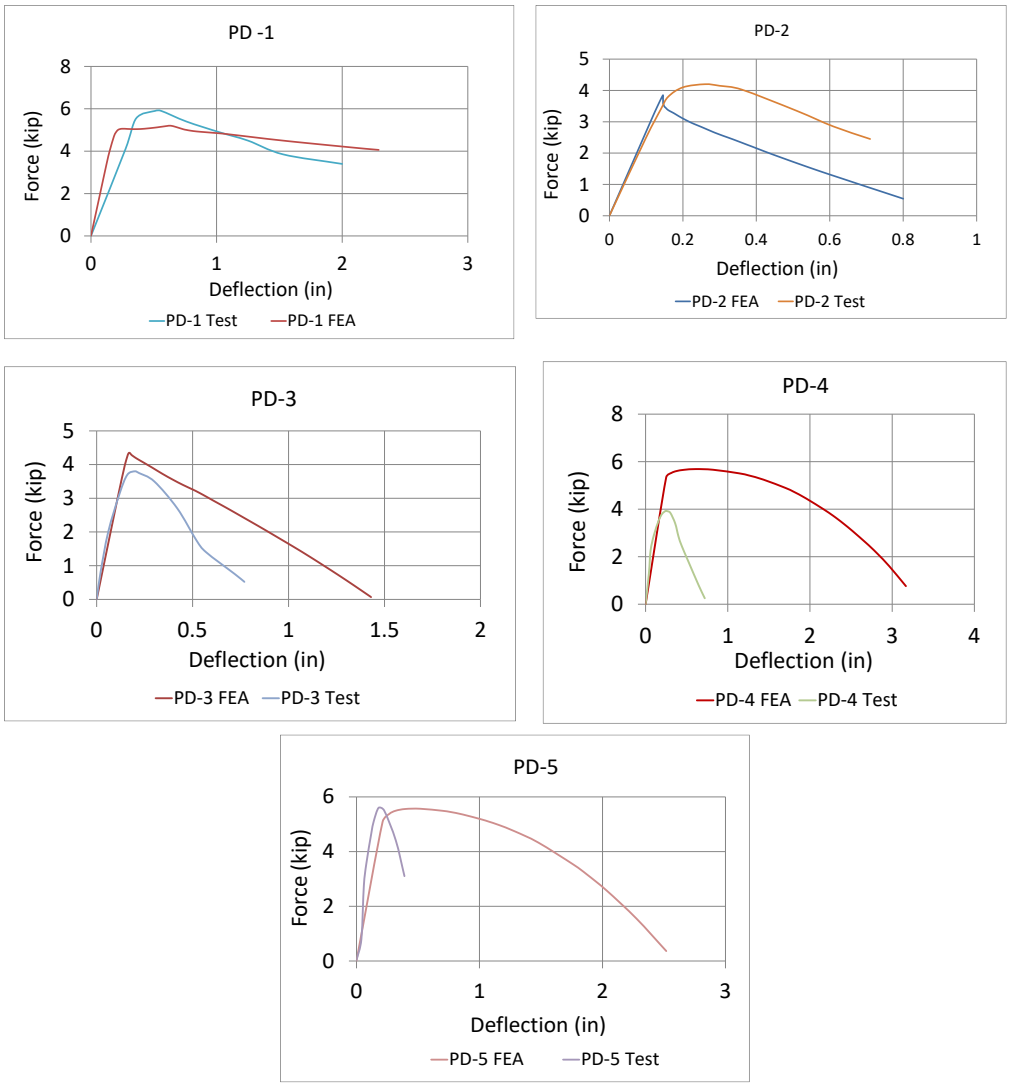

Figure 4.15 Comparison of FE and experimental analysis results for portal PD series

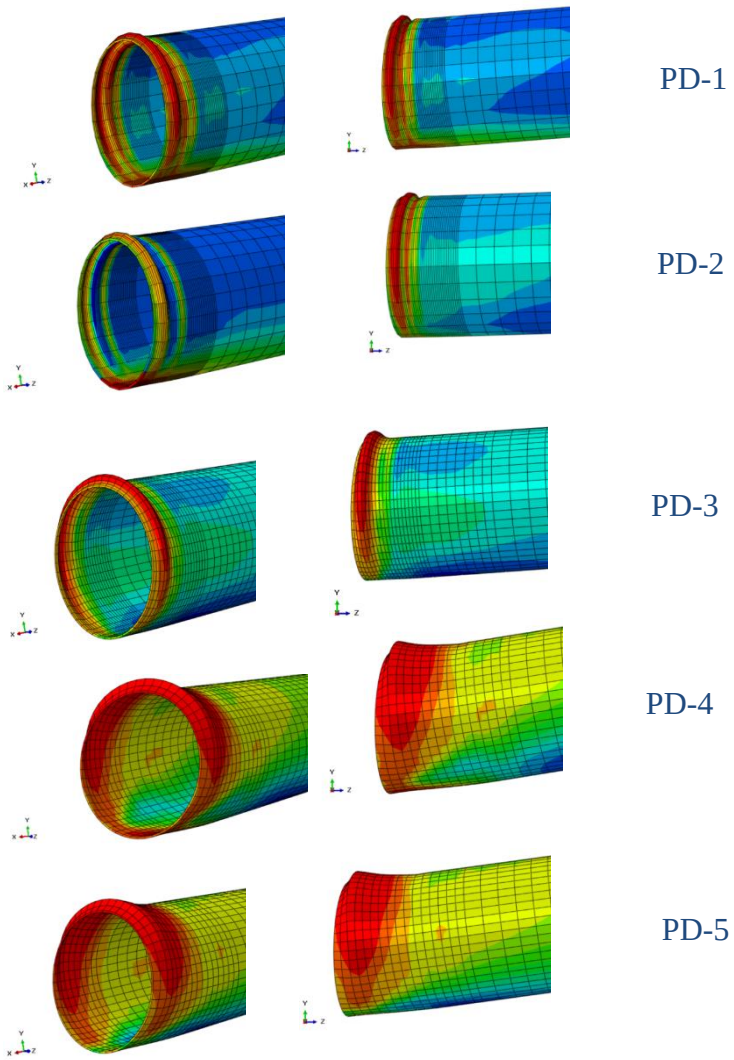

Figure 4.16 FE analysis failure pattern of portal PD series

The mesh has a role in the analysis results. PD-4 and PD-5 have coarse mesh analysis results. It is because too fine mesh has issues with the analysis convergence, especially for the large axial load. A good example is shown in Figure 4.17. The mesh size of PD-1 was changed to 0.375x0.375 inch at the base and coarser at the tip. Being a coarse result shows higher load capacity compared to a finer mesh in PD-1 earlier. 0.45x0.45 mesh-size at the fixity analysis results is also observed. The question is how fine the analysis has to be in order to get accurate results. However, it can also be seen from the results in some cases, for TxT mesh size, FE

analysis results, and experimental analysis results are perfectly matching. From FE analysis point of view, the finer the mesh, the more accurate the result is, as long as there is no convergence issue.

From previous test results, Test 1 load capacity is always the highest as there is no axial load in the test. The axial load increases from Test 2 to Test 5. Thus, Test 5 lateral load capacity of the tube should be the lowest. In PD series, Test 4 and 5 capacities are higher than Test 1-3. Thus, the validity of the test results is doubtful especially for Test 5. Figure 4.17 and Figure 4.18 show plots of the results.

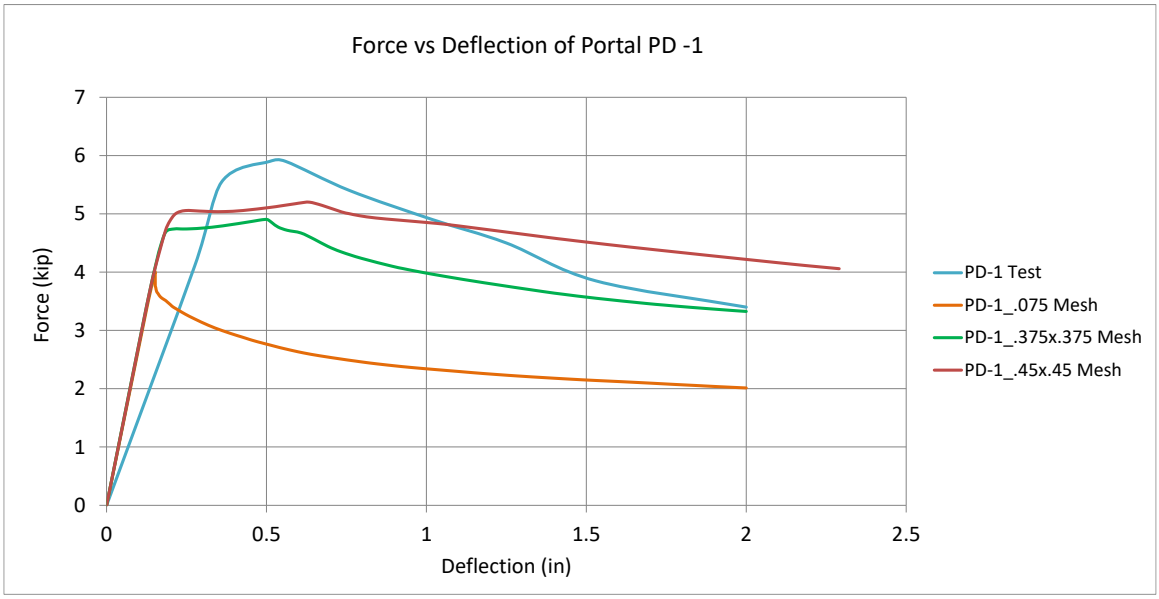

Figure 4.17 Mesh size analysis results of portal PD series

PD-1 Mesh size .375x.375 inch Failure

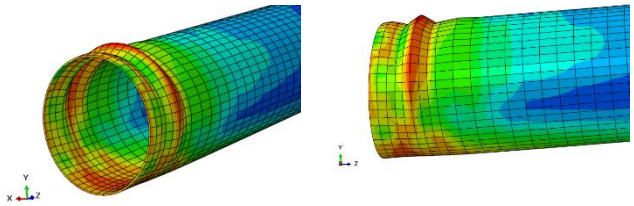

PD-1 0.45x0.45 inch Mesh Stress Failure Results

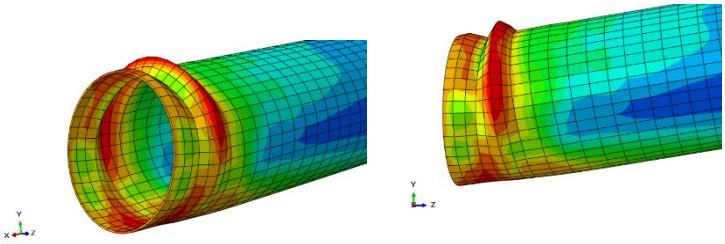

Figure 4.18 Portal PD-1 failure pattern of different mesh size

4.6 Benefits of Using Thin Pipes in Offshore Structures

Hollow pipes are widely used in offshore structures. Hollow pipes are good in resisting torsion. Imagine a stress distribution of moment or torsion for a tubular section within the elastic range, there are small stresses in the mid-section of the solid pipe. In addition, consider the slenderness ratio of l/r. Using a solid pipe or a very thick section will have larger l/r, causing smaller allowable buckling stress. Let us see an example of a beam column or beam subjected to axial and lateral loading. The beam setup is shown in Figure 4.19. Assume, solid pipe 50.8cm (20-inch) is used. The weight is increased by 10 times from 0.5-inch-thick hollow pipe, and this means the material cost is increased by 10 times, ignoring the construction cost and other materials' cost that need to support this element. The vertical displacement of 20cm is applied at the tip of 5m cantilever beam with an axial load-displacement of 1.27cm. The base is fixed and the tip was partially restrained, allowing axial and X-direction displacement.

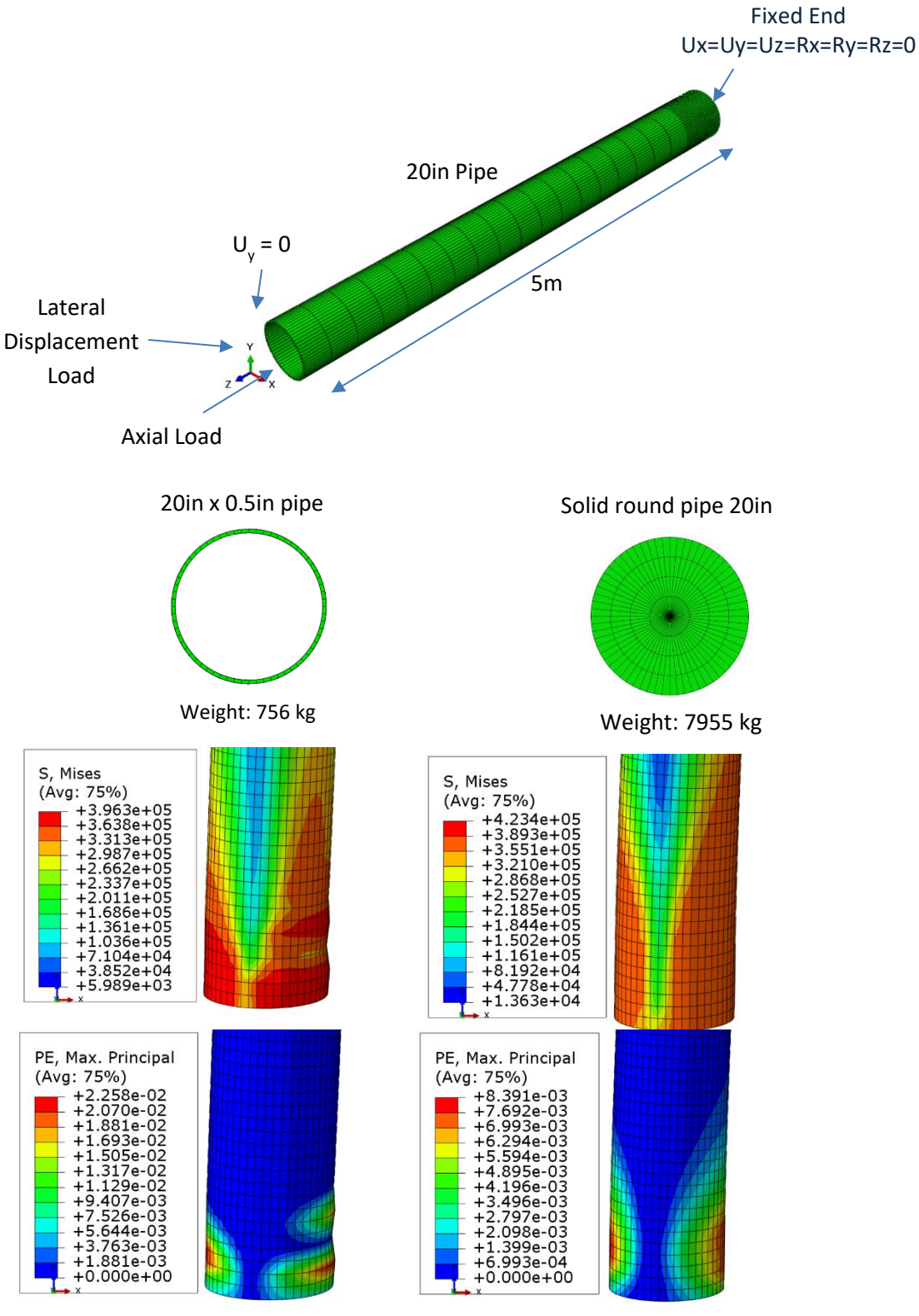

Figure 4.19 Beam column analysis of hollow and solid pipes

The stress in solid pipe increased by 7% and the strain reduces by 62% compared to the hollow pipe. So, in terms of stress, there is no significant improvement from thin pipe to solid pipe. The weight of solid pipe increased by 10 times, and this will cause much more problems in construction and will add much weight to the structure. The solid pipe itself can bring catastrophic to the overall integrity of the ocean structure. Hence, pipes with reasonable thickness are more beneficial to offshore structures than very thick pipes in terms of structural integrity and cost.

CHAPTER 5 CEMENT GROUT DOUBLE-WALL COMPOSITE PIPE

Earlier in chapter 2, the use of composite pipe in offshore structures were explained. The annulus of double-wall composite pipe is grouted with cement. This chapter includes FE analysis of the double-wall composite pipe with cement grout. The FE analysis is then compared against experimental results. The FE analysis results are used for the validation of composite pipe experimental results since steel-polymer-steel experimental literature is not available.

5.1 FE Model of Cement Grout Double-wall Composite

The composite section consists of the outer steel section, cement grout, and inner steel section. To ensure that the displacement load is uniformly applied at the tip, a cap plate of 10mm is attached at the tip of the composite pipe. The base surface is pinned, the surface is a restraint against X, Y, and Z translation. The cap plate surface is restrained against X and Y translation and displacement load is applied along the axial, opposite to Z direction. Deformable 3D solid elements are used for both steel tubes and concrete grout. Figure 5.1 shows the FE meshed model of the composite pipe.

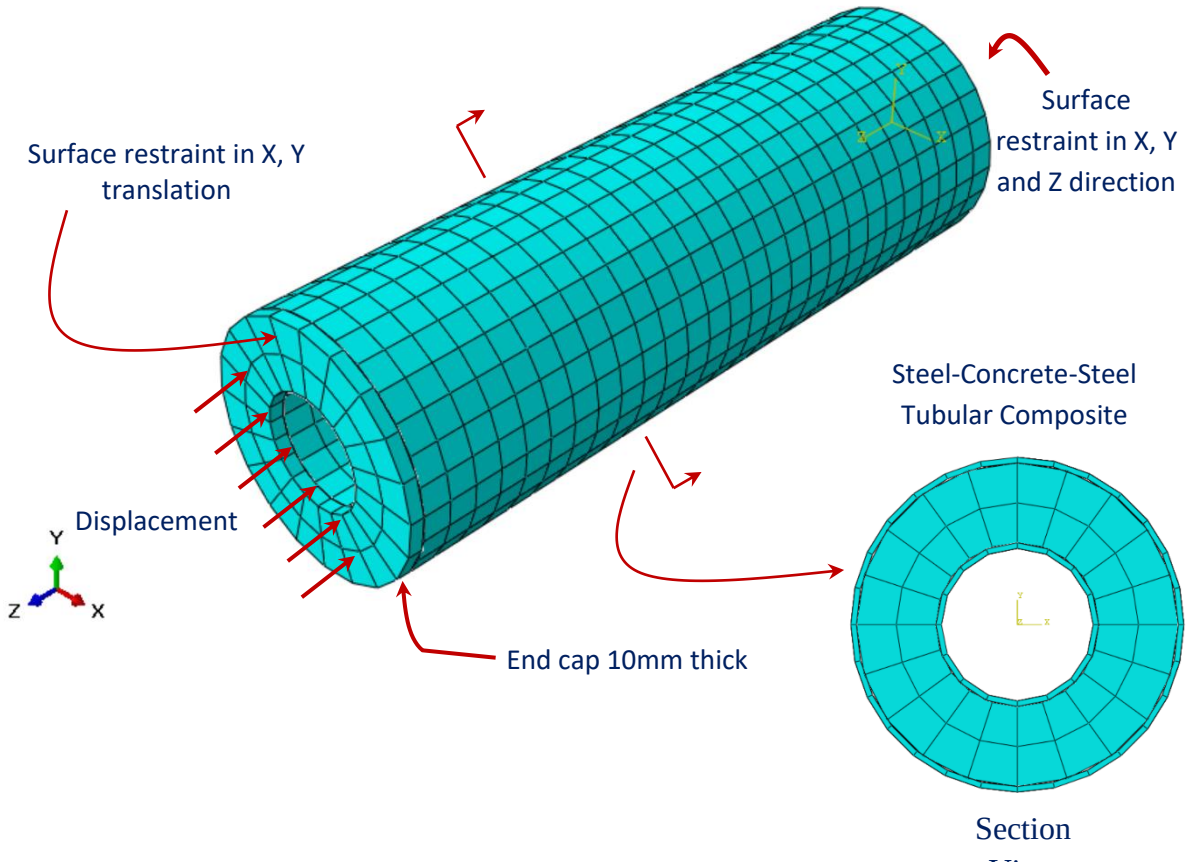

Figure 5.1 FE meshed model the tubular sandwich composite

For cement grout, elastic and Drucker Prager plastic properties are entered for grout material. As an FE analysis performed by Pagoulatou et al. (2014), the angle of friction and flow stress ratio are 20 and 0.8 respectively. The calculated grout plastic stress-strain curve using Eq. 2.7 is entered in Drucker Prager hardening suboptions for compression. The elasticity of cement grout is calculated using Eq. 2.8.

Elastic and plastic material properties are used for steel. The steel plastic stress-strain curve is calculated using Eq.2.11 for inner and outer tubular. Elastic property only is used for the end cap, and the modulus of elasticity used is 1000 times higher than normal steel so that it does not deform and thus the load is uniformly applied on the composite tube section.

For interaction properties, the primary-secondary surface to surface discretization is used between steel and cement grout with steel being the primary and cement grout surface being the secondary. As the primary element moves the secondary follows. Lam et al., (2012) used 'tangential behavior' with the friction of 0.3 and 'hard contact' for 'normal behavior'. The same interaction properties are used herein. 'Hard contact' interaction minimizes the secondary surface penetrating into the primary surface. Pressure can be transmitted when in contact and separated when there is no pressure. Small friction values have an issue with convergence. However, 0.3 friction value provides satisfactory results, and hence more studies are not conducted. The same primary-secondary interaction is used for the end cap and composite tube with the end cap being the primary and the composite tube being the secondary. Large tangential behavior for friction .99 is used for the cap contacts. The base end surface of the composite tube is pinned. The end cap is a restraint against X and Y direction. Displacement loading is applied on the end cap along the negative Z axial direction.

5.2 FE Analysis Results

A qualitative comparison of FE results and Test failure image in Figure 5.2 shows local buckling failure occurs at a region along the composite column. In this study, the same strength of cement is used for all three analyses. For smaller steel tube outer diameter with 180mm, local buckling failure occurs near the base with pinned fixity. CC2a has thicker grout of 63mm compared to CC3a with a thickness of 43mm, however, the location of failure for both composite tube is the same and have identical failure. For a larger tubular diameter such as CC6a, local buckling failure is near end cap loading. Overall, the failure pattern for the composite tube is the same regardless of the change in steel tubes diameter with larger tube diameter appears to have lesser buckling failure compared to the smaller composite tube diameter. Both steel and cement

grout materials have reached their ultimate strength as shown in von Mises stresses in Figure 5.2. Figure 5.3 shows the experimental results.

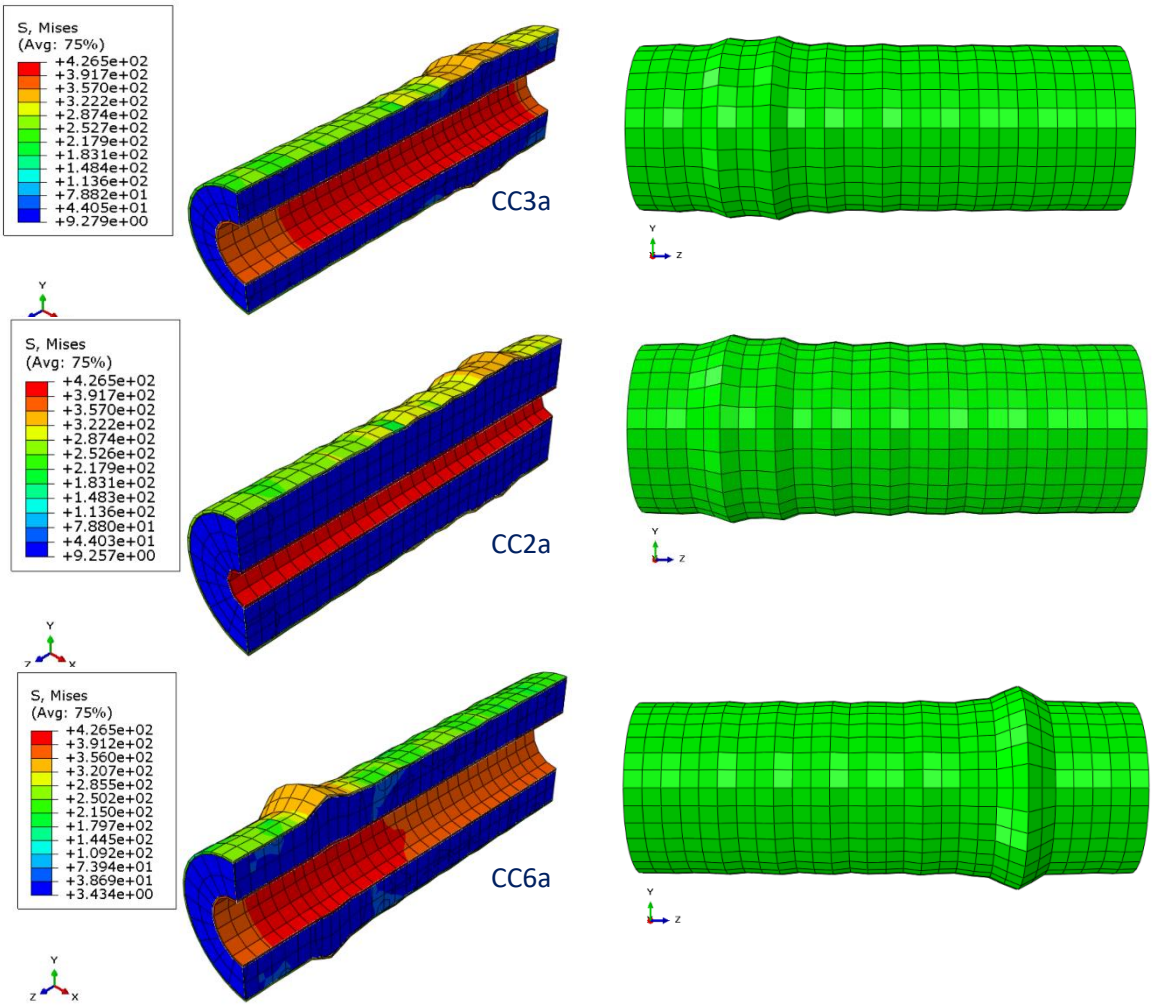

Figure 5.2 FEA failure modes and stresses

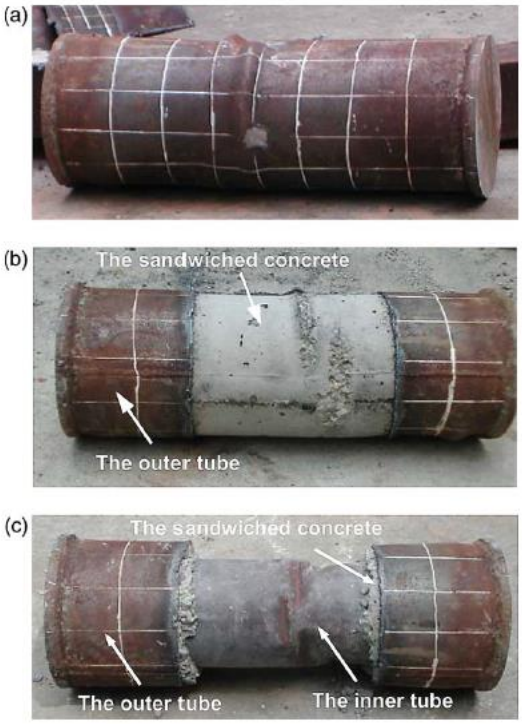

Fig. 2. Typical failure mode of CFDST stub columns; (a) typical specimen after testing; (b) after removal of partial outer steel tube; (c) failure mode of the inner CHA in CFDST.

Figure 5.3 Typical test failure mode of steel-concrete-steel composite tube

Tao et al. (2004)

Quantitative FE results comparison with test results are shown in Figure 5.4. FE analysis results are closely matching with test results. It can also be deduced that load capacity is reduced much faster for a larger diameter with the composite tube. CC2a and CC3a analysis result shows load reduces slowly with an increase in the strain, whereas load reduction is more rapid in larger diameter CC6a.

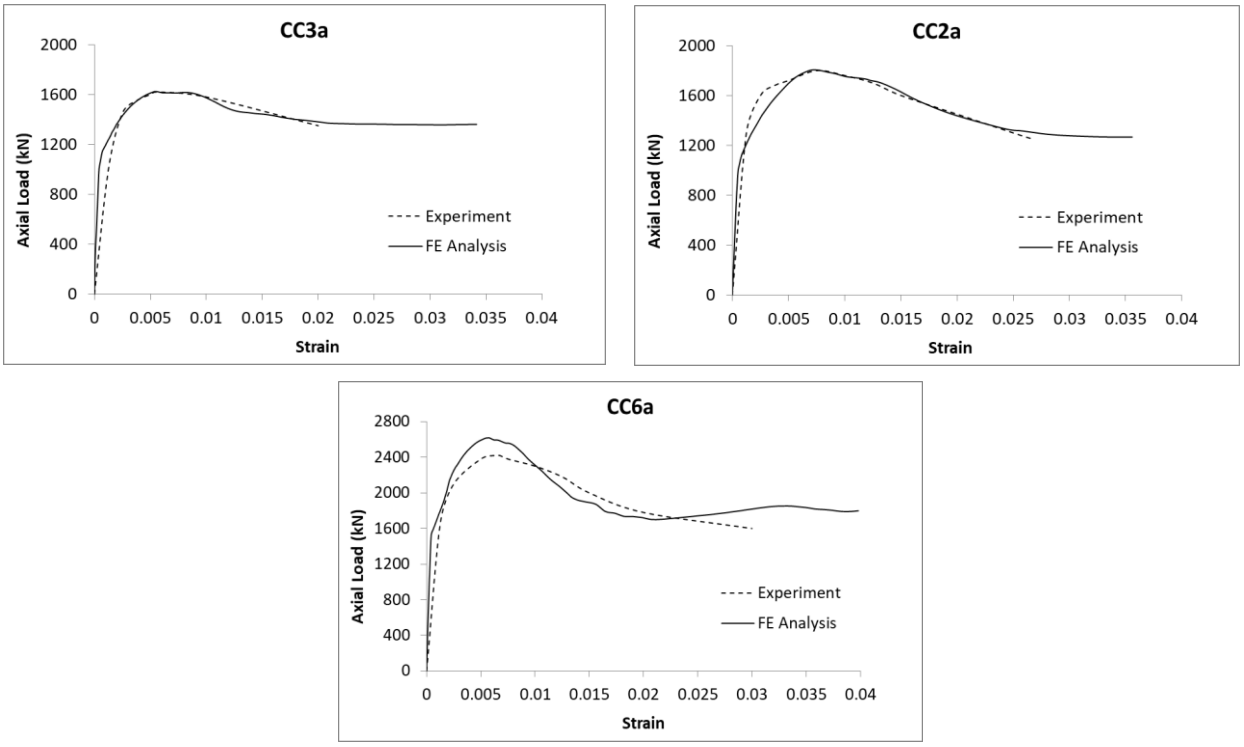

Figure 5.4 FE analysis result comparison with published test results

5.3 Mesh Size Factor

Mesh size is not influencing the analysis results for the composite section. Hu and Su (2011) also stated this. Several trials have been run for this research until the reliable result is achieved and a result of one parameter is documented herein. For example, a mesh size of 20mm was used for the composite section with an outer tubular diameter of 180mm, and 25mm for the composite section with an outer pipe diameter of 240mm. A finer mesh than this does not change the analysis result. In addition, finer mesh requires a longer time for the analysis and hence it is unproductive. Moreover, the too fine mesh also causes analysis divergence. One way to resolve this is to increase the number of increment steps and it requires even more time to run the analysis. On the contrary, too much coarse mesh does not have good results beyond peak load as shown in Figure 5.5. For example, the nonlinear degradation post-peak load can be above the actual curve (almost horizontal straight line beyond peak load) and thus failure

behavior beyond peak load cannot be captured correctly. However, the peak load is not much affected by coarser mesh. Mesh sizes used herein are less than 4% of the outside steel tube circumference this gives satisfactory analysis results. Much finer than this mesh size does not affect the analysis result accuracy.

Results of coarser mesh size of 25mm, finer mesh sizes, and mesh size used for this research which is 20mm for CC3a section are plotted in Figure 5.5 comparison with test curve. Finer mesh sizes used are 15mm for the inner tube, 18mm for the outer tube, and 20mm for the concrete grout. It can be seen from the plot and failure modes shown in Figure 5.5 that finer mesh does not have more contribution to the accuracy of the analysis results.

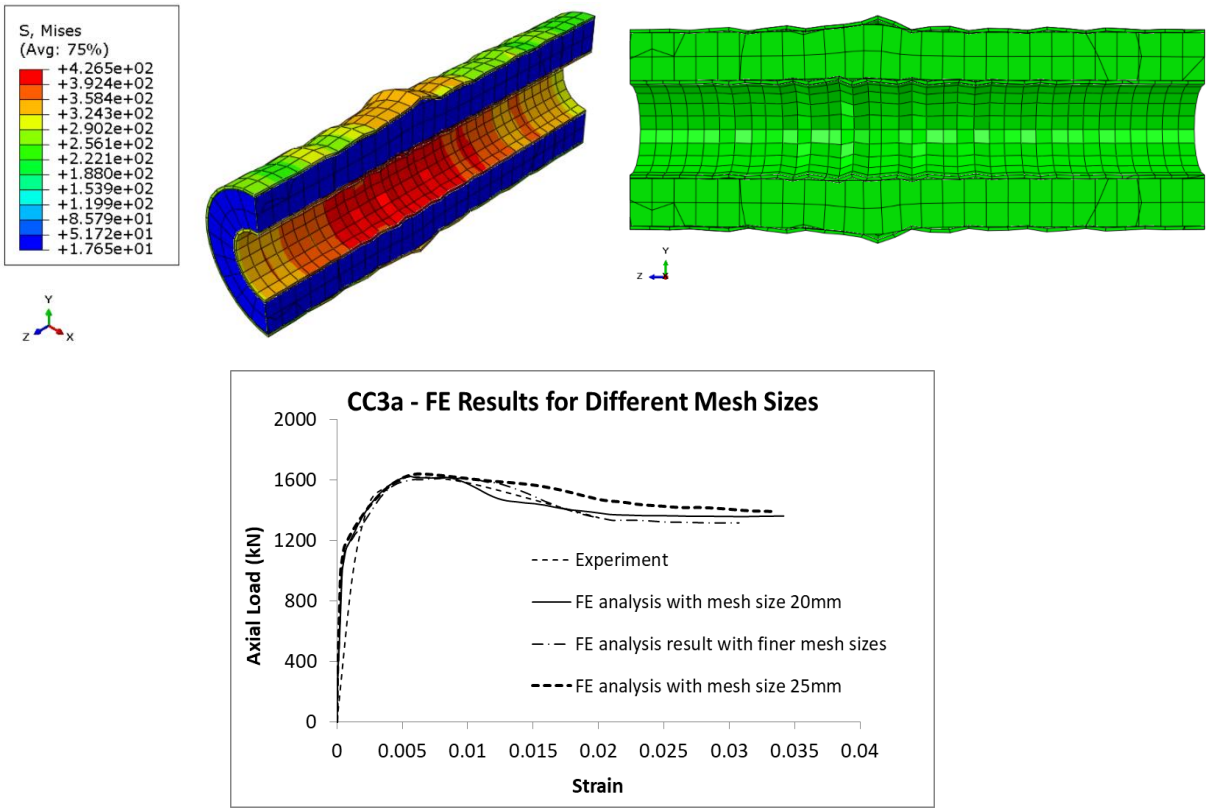

Figure 5.5 Results of different mesh sizes

5.4 Analysis Results of Different Sections

Analysis results of different sections of the composite tubes are analyzed. Plots of load against strain are presented in Figure 5.6.

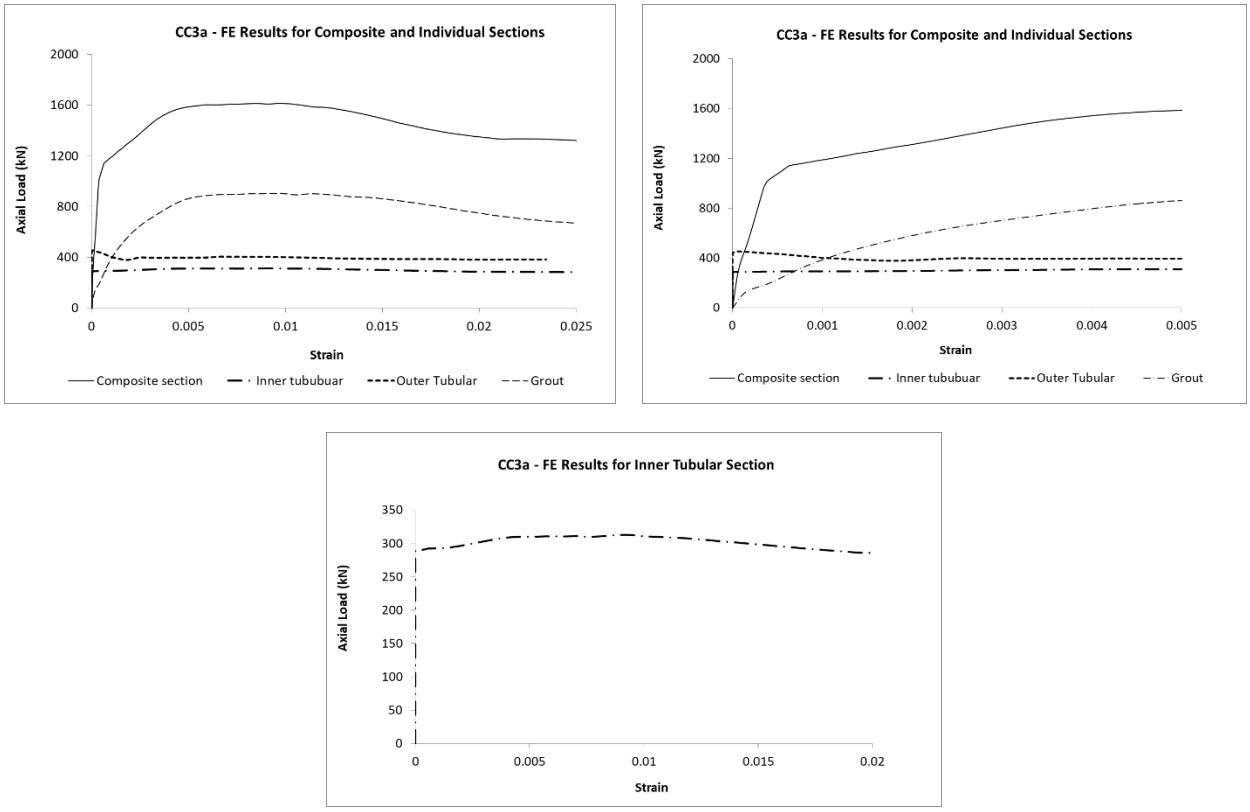

Figure 5.6 Load against strain plot of individual and composite section

Peak load and its strain of the individual and composite sections are extracted and tabulated in Table 5.1.

Table 5.1 Summary of Peak Load and Strain Values

Section/Layer	**Peak Load**	**Strain at peak load (kN)**
Outer tubular	0.0000646	453.29
Inner tubular	0.0090231	312.43
Grout	0.0112232	899.65
Combined section	0.0096385	1614.45

From the analysis results, inner and outer tubes do not take much compression load as expected since steel is weak in compression. The inner tube exhibits strain rapid increase up to the elastic limit and then slowly increases in the plastic region until peak capacity is reached at a strain value of about 0.01. Then, the load and strain decrease gradually. Similar to the inner tubular, the outer tubular instantly reached its peak load capacity at a very small strain value of 0.0000646. Thereafter, the outer section experiences sudden failure into the plastic region. At this failure point, the inner tubular is carrying the compressive load of 288 kN and it slowly continues to pick up the load up to 312 kN with a gradual increase in strain. From the analysis results, the outer tubular steel section experiences failure much earlier than the inner tubular section in terms of strain. The concrete grout is strong in compression, able to take axial load much higher than the steel. The grout load capacity is 899 kN and its strain is 0.011. The grout strain increase is sudden up to elastic, gradually increases up to the peak load in the plastic region, and then degraded even more slowly post-peak load.

Using the strain formula, for the composite section length of 540mm, the outer tubular section buckles at axial deformation of 0.348mm whereas the inner tubular experiences buckling at the deformation of 4.985mm. Strain is directly proportional to deformation. Inner tubular being higher strain able to take deformation approximately 140 times more than the outer tubular. This is good news for steel-grout-steel application in engineering as the outer tubular experiences failure earlier than the inner tubular. At any time, the outer tube experiences strain or buckling, the inner tubular section experiences 140 times lesser.

CHAPTER 6 THE ANALYSIS OF BURIED PIPELINE

This chapter includes the analysis of single-wall and double-wall composite pipes in clay using FE analysis. The stress, strain, and ovality of the pipes are analyzed and compared against the industry acceptance. Verification of laterally loaded pile in clay is performed using FE analysis and the results are compared against the experimental results. The laterally loaded pile represents the half-pipe of the full pipe, and the displacement load represents earthquake loads at the fault plane. Mesh size effects are also studied. The equivalent single-wall pipes are also analyzed, and the results are compared against the double-wall composite pipe. Different methods of FE analyses are used such as cap plasticity and rigid plastic analysis methods, and the analysis results are compare against the experimental results.

6.1 Single-wall Pipe and Its Properties

Tow single-wall pipes were tested. Two different pipe sections 50.8∅x2.54 cm and 50.8∅x1.27 cm were embedded in the solid model which represents clay properties. This represents a pile foundation of a fixed offshore structure or half of a buried seafloor pipeline. The results were compared against Marshall's (2004) published results. In addition to the strains, stresses, and lateral displacements, ovalizing of the pipe is also observed and compared against acceptable industry limits. From the research, it was found that pipeline has more stringent governing factors compared to a pile foundation of fixed structure such as jacket structure.

Figure 6.1 shows the solid clay, pile, and boundary condition of the model as stated by Helwany (2007). The base is pinned in all DOF. The soil top surface is restrained against the Y direction, modeled as if the fault plane is slick and soil is not allowed to cross it. The pile and clay interface are a separable contact surface with friction. The soil mesh size around the pile

circumference is kept 20 – 25 cm. The pile mesh sizes are 6-7 cm. The vertical mesh size of the clay is 2 meters in the area of interest, and elsewhere the mesh sizes are 5 meters.

Displacement controlled load is applied laterally at the top of the pile until the pile is yielded to the ultimate limit strength. Lesser lateral deflections are also investigated until acceptable analysis results are found. The mesh size used in the analysis is sufficiently fine enough for analysis result accuracy. Too coarse analysis results can affect analysis results accuracy. On the contrary, the too fine mesh will take a much longer time to compute the analysis and it will take up more hard disk space. In addition, it also affects the analysis convergence. Hence, the mesh size here used is sufficient to accurately calculate the analysis. In figure 6.1 below, the mesh around the pile in the middle regions is finer than the other part of the model because the finer mesh is required in the point of interest. The other part meshes are coarser because these regions do not affect analysis results accuracy as the stresses are around the pile in the middle regions. Mesh size study results will also be present later in this chapter.

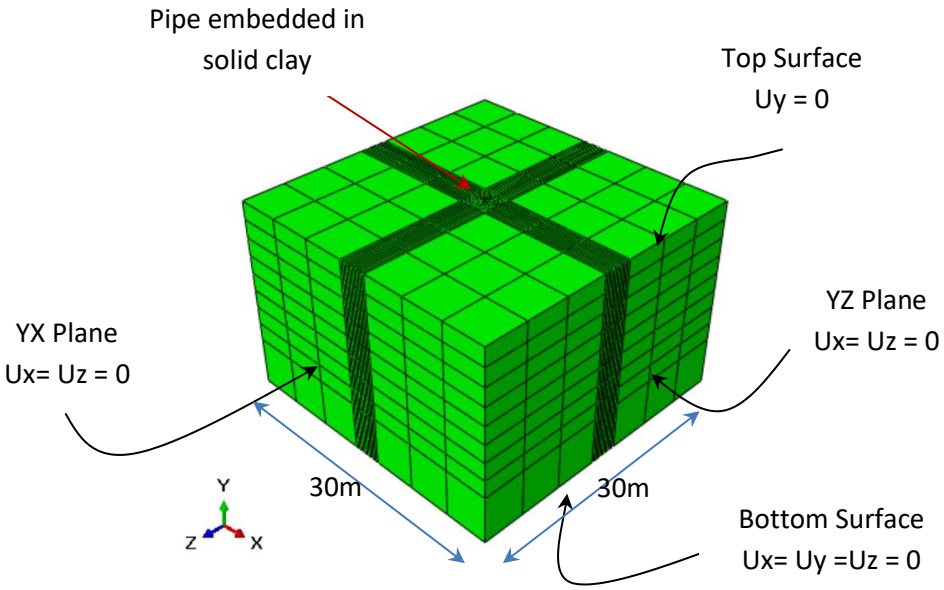

Figure 6.1 Boundary condition of the solid clay and pile model

Steel Modulus of Elasticity is taken as 200,000,000 kN/m^2 and Poisson's ratio is 0.3. Figure 6.2 shows the plastic stress strain curve used for the steel pipes.

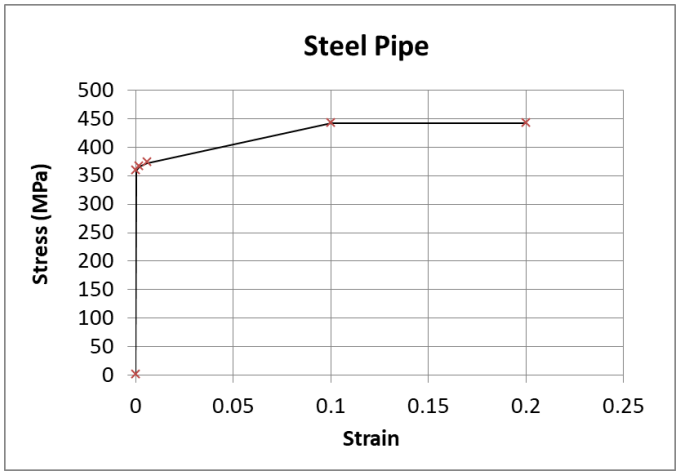

Figure 6.2 Steel stress-strain curve

Clay elastic modulus is the 7000 kN/m^2 and Poisson's ratio is 0.4. Figure 6.3 shows the stress-strain curve used for clay properties. This soil is a medium clay model used in Marshall (2004).

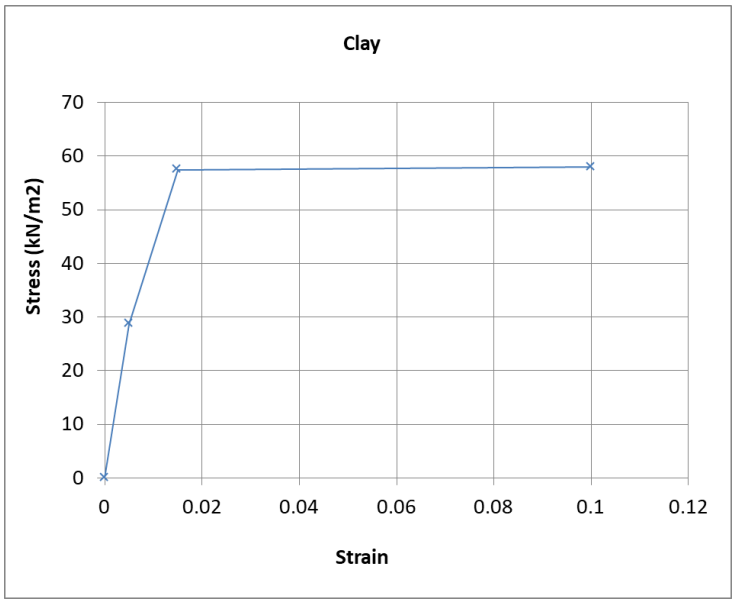

Figure 6.3 Clay stress-strain curve

6.2 Analysis Results

Figure 6.4 shows force- deflection of the two pipes, steel stress and soil mesh deformation. The thicker pipes being higher stiffness is able to take higher load.

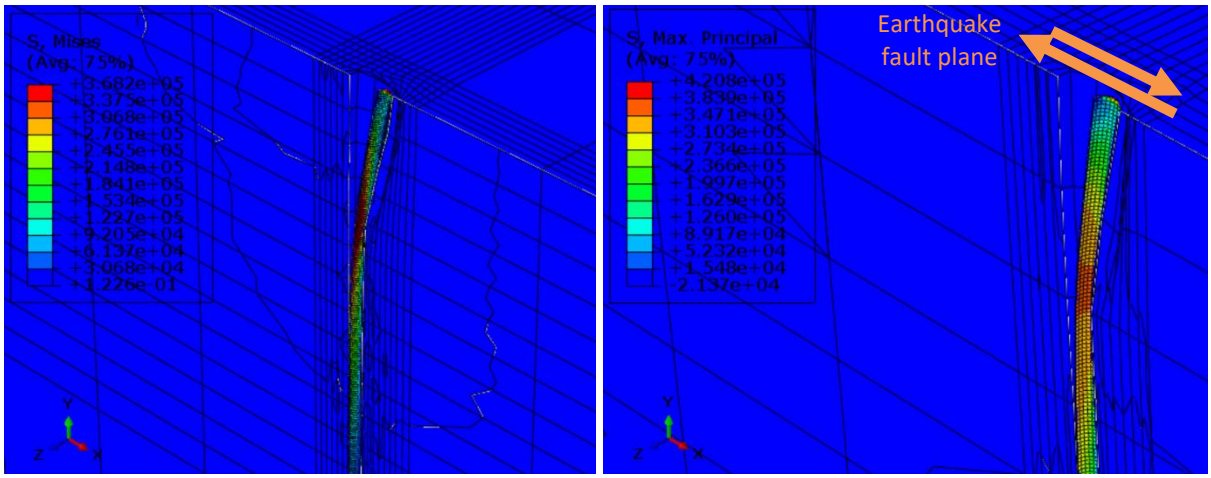

50.8∅x2.54 cm Pipe
Pile head displacement 104cm

50.8∅x1.27 cm Pipe
Pile head displacement 80cm

Figure 6.4 Steel stress and soil mesh deformation

Figure 6.5 shows progressive ovalization at the maximum bending point. The is set to ensure that the pipeline remains piggable. This limit is reached at a displacement of 20 cm for the thinner pile, and 52 cm for the thicker pile, or 0.40m and 1.04m for the pipeline at a fault.

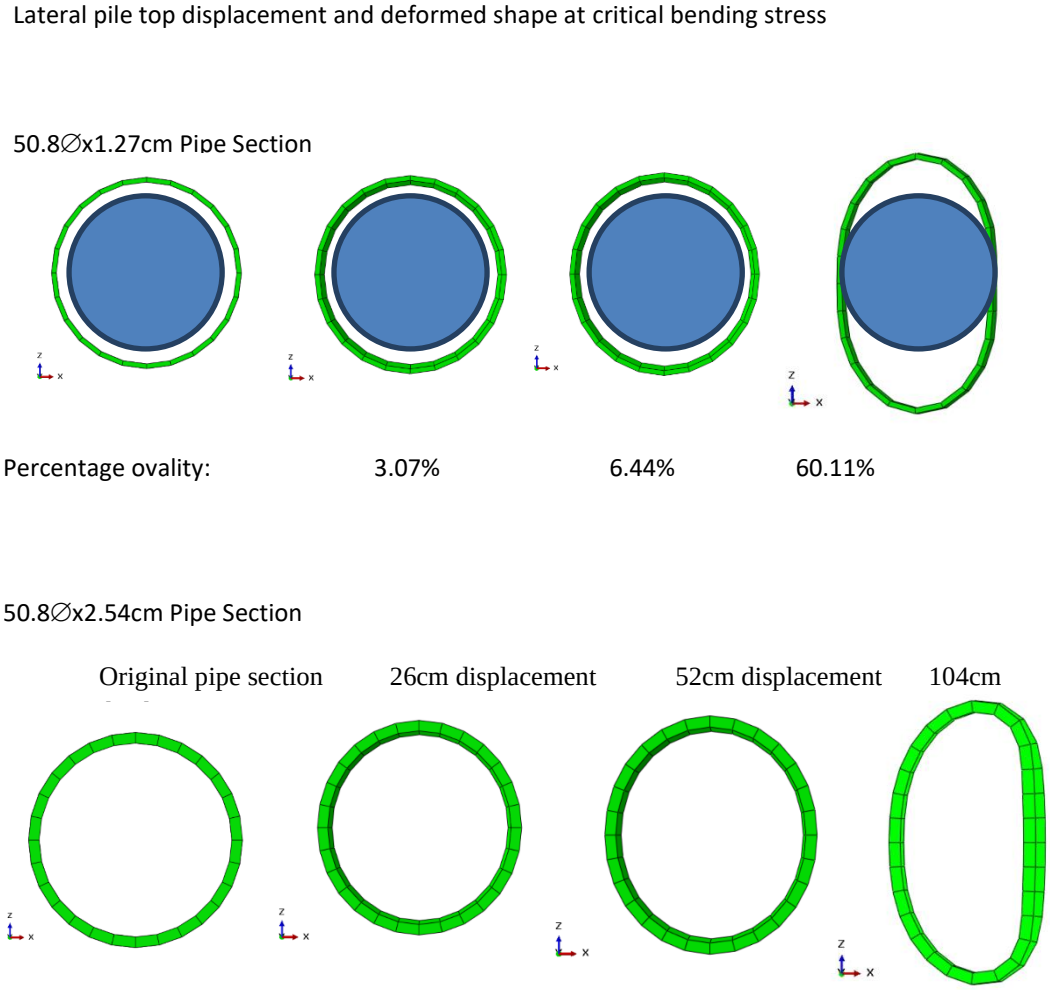

Figure 6.5 Progressive ovalization and a pigging device in the pipe

Figure 6.6 shows the progression of deformation and steel stress for the pile or half-pipeline. The thick pipe appears skinnier because a longer length is shown. 3% (DNV-OS-F101) or 2% (API RP 1111) ovality is the usual limit, however, 6% can be tolerated for special circumstances if pigging can still be done. Maximum and minimum diameter differences should not exceed 8% (ASME-B31.1, 2001).

50.8∅x1.27cm Pipe Section

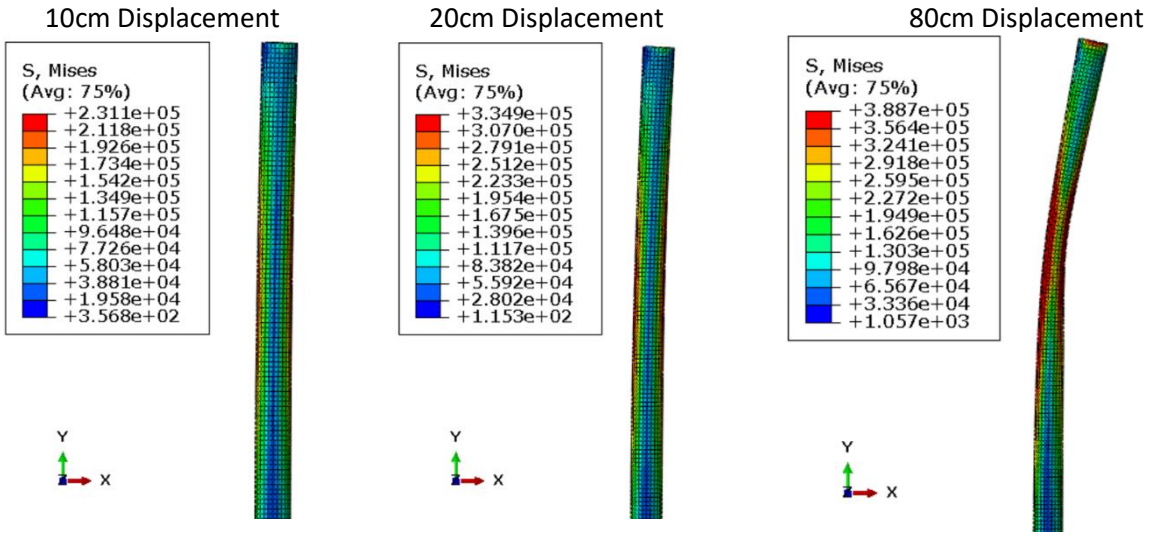

50.8∅x2.54cm Pipe Section

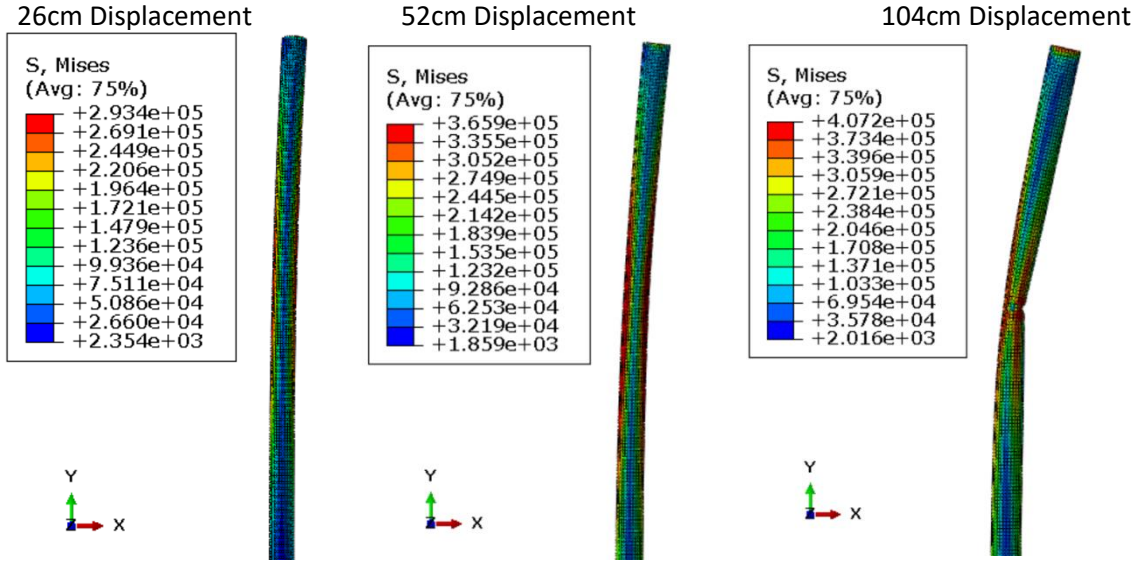

Figure 6.6 Pipe stresses and deformation

Von Mises stresses along the pipe for one inch and half inch thick pipes are shown in Figure 6.7.

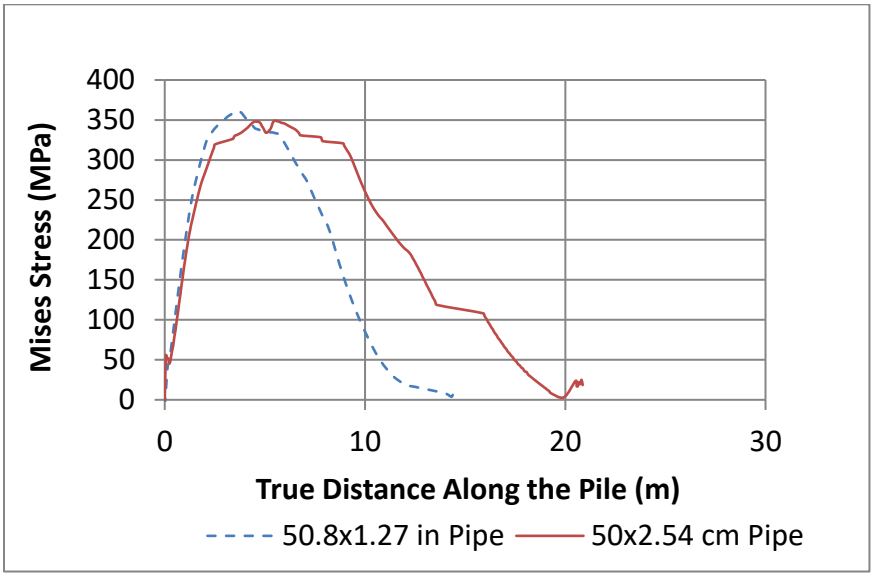

Figure 6.7 Pipe stresses along the pipe

Figure 6.8 shows how two pile models are combined to show both antisymmetric halves of a pipeline crossing a fault. The pipeline displacement is twice that of the pile model in Figure 6.8. Plastic hinge location is qualitatively similar to that predicted by the rigid-plastic model (Broms 1964, Marshall 2004). Because of uniform lateral soil resistance along with the pile, the plastic bending is not all concentrated at the hinge, but it is spread out along the pile length. This allows the tubular member to achieve more rotation and displacement for a given bending strain limit.

The pipes are displaced to failure. Qualitative failure modes are shown in Figure 6.8.

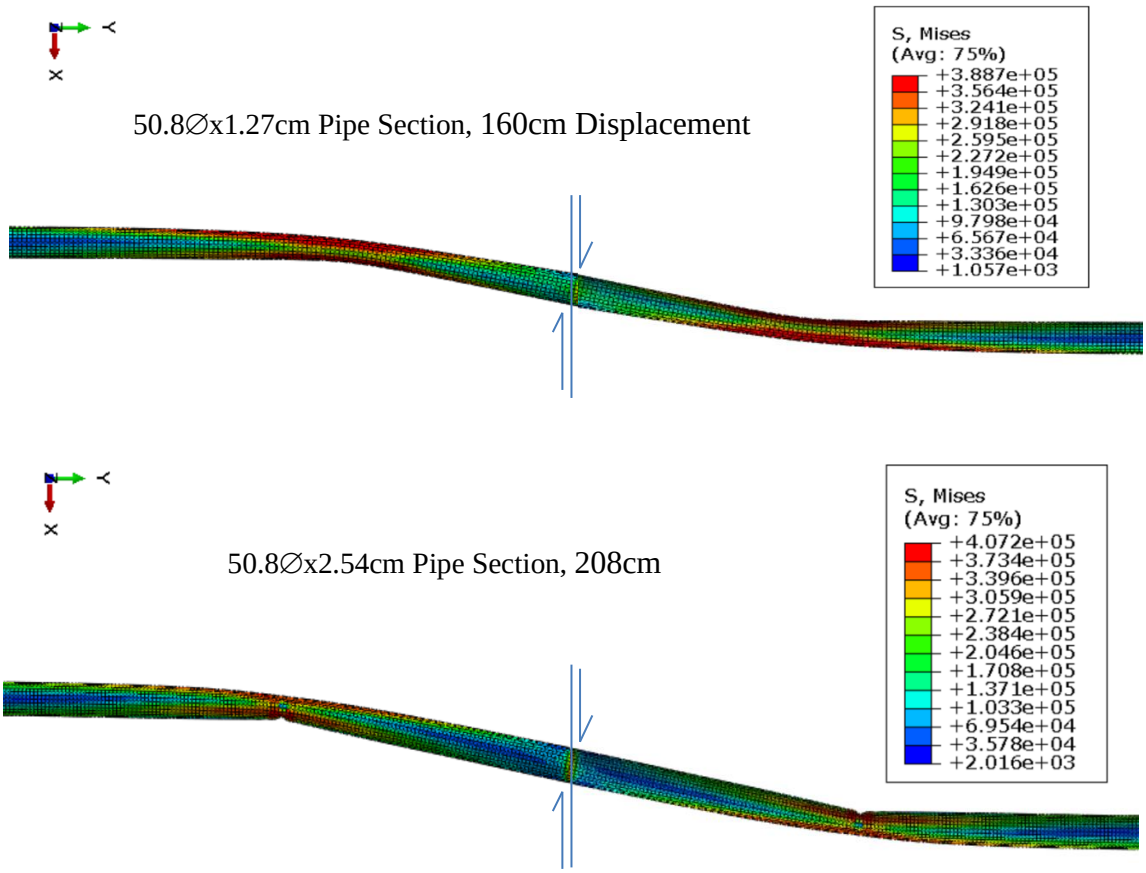

Figure 6.8 Pipeline failure modes at a fault

Result summary of the single-wall pipe analysis are tabulated in Table 6.1.

Table 6.1 Analysis results of the single-wall pipe for half and one inch wall thicknesses

50.8cm Single Wall Pipe Diameter	Thickness (cm)							Limit	
	1.27			2.54				API-5L/ ASCE	DNV-OS-F101
Deflection (cm)	20	40	160	30	52	104	208		
D_{max}	51.5407	52.3464	62.7093	51.2893	51.939	53.5196	60.99		
D_{min}	50.0042	49.119	32.6075	50.02827	49.634	47.8271	36.63		
Ovality (API RP 1111), %δ	1.5131	3.1808	31.5808	1.2446	2.2693	5.6169	24.9539	2% (API)	-
% Ovality, % Out -of-roundness	3.07	6.44	60.11	2.52	4.60	11.37	48.64	-	3%
Strain, ε	0	0.0001858	0.02842	0.02842	0.00006289	0.001466	0.04248	2% (ASCE)	2%
von Mises Stress (MPa)	231.1	334.9	388.7	208.7	293.4	365.9	407.2		
Pipe Length (m)	15	15	15	15	15	15	15		
Crital stress location on pipe measured from ground surface (m)	2.8	3.7	3.6	4.56	5	4.6	4.5		
Load (kN)	333.435	465.95	858.085	468.451	626.684	899.869	1052.33		

6.3 Double-wall Pipe

Analysis results of the double-wall composite pipe is shown in Figure 6.9

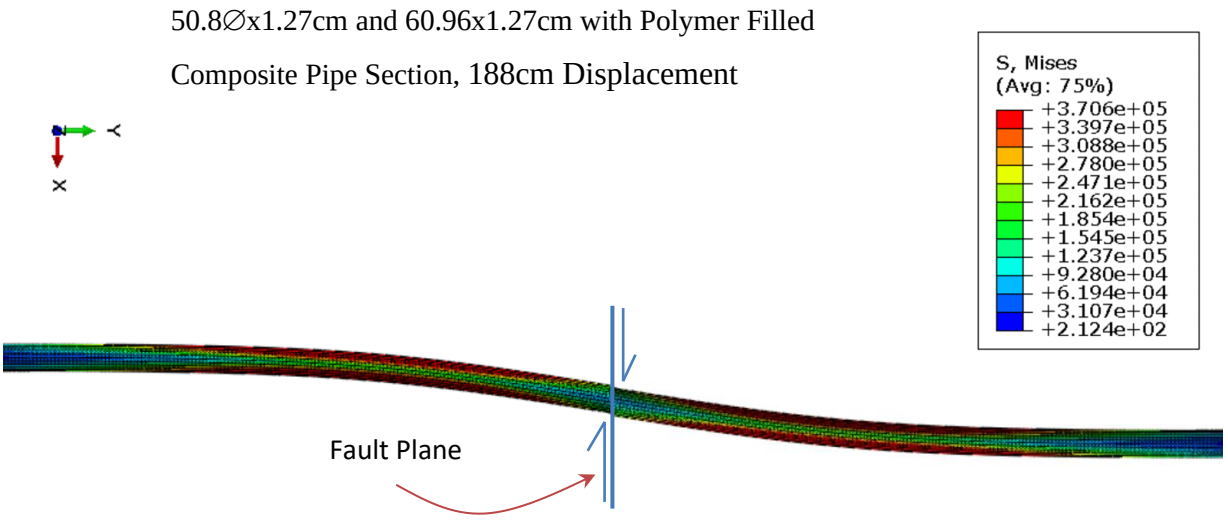

Figure 6.9 Pipe offsets at fault plane

6.3.1 Single-wall and Double-wall Pipe Analysis Comparison

This section of the research documents the bending, strain, and ovalizing of the single and double-wall composite pipeline.

Table 6.2 Analysis results of single-wall pipes with half in thicknesses

Double Wall Composite Section	Pipe Section - Full Pipes		Pipe Section - Half Pipes		Limit			Limit	
	50.8x1.27cm	60.96x1.27cm	50.8x1.27cm	60.96x1.27cm	API-5L/ ASCE	DNV-OS-F101		API-5L/ ASCE	DNV-OS-F101
Deflection (cm)	188	188	343.53	343.53					
D_{max}	50.8173	60.9763	48.2406	60.9376					
D_{min}	50.56	60.6787	48.14954	60.617					
Ovality (API RP 1111), %δ	0.2538	0.2446	0.0945	0.2637	2% (API)	-		2% (API)	-
% Ovality, % Out -of-roundness	0.51	0.49	0.15	0.53	-	3%		-	3%
Strain, ε	0.0037	0.004978	0.005659	0.005659	2% (ASCE)	2%		2% (ASCE)	2%
von Mises Stress (MPa)	370.6	370.6	370.6	370.6					
Pipe Length (m)	25	25	25	25					
Crital stress location on pipe measured from ground surface (m)	5	5		8.15					
Load (kN)	1342.55	1342.55	1958.26	1958.26					

6.3.2 Effects of Axial Tension and Internal Pressure

From the analysis result, it can be seen that failure does not occur even at 3.43 meters (11.25 ft). Marshall (2004) stated that a double-wall composite section can go displacement 2.4 meters (7.8 ft). From FE analysis result, it is observed that at 3.43m displacement, ovality and strain are within tolerance for the composite section. The stress is still in elastic range.

The effects are both favorable for increasing the bending strain at which local buckling occurs. However, a buckled pipe will fracture in tension more readily than an intact one. If a gas pipeline is depressured but not filled with seawater, a net external pressure develops, which is detrimental. These issues are left for further study.

5.4 Verification of laterally loaded pile in clay

Matlock (1970) performed a laterally loaded pile in soft clay, near the mouth of Sabine River. The clay's vane shear strength was 14.4 kPa (300 psf).

FE analyses were performed using 2 methods and they were compared with the test result. The first method was the modified Drucker-Prager/ Cap model. The second method was Marshall's plastic clay model.

The clay unit weight was taken as 20 kN/m^3. The modulus of elasticity of the clay was taken as 2150 kPa. This value was used because E_c/c was taken as 150, the value of this ranges from 50 to 200 (Matlock, 1970). The pile diameter was 31.9cm and the wall thickness was 1.27cm (12.6 in OD x 0.5 in thick). Pile embedded length was 12.8m (40 ft). Figure 6.10 shows the clay model with pile embedded. The pile stick-out is 6.36mm. Lateral displacement is being applied at the pile top.

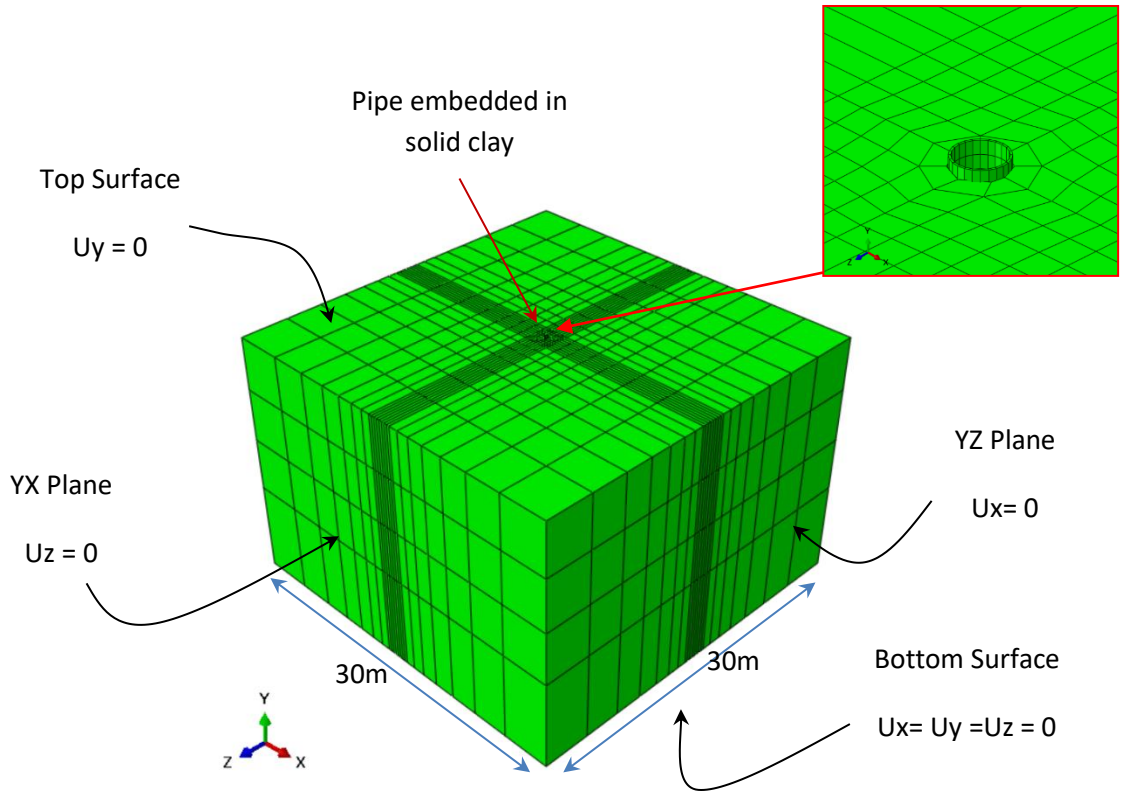

Figure 6.10 Pile embedded in clay, meshed model with the boundary conditions

6.4 Pipe in Clay Analysis and Benchmark Test – Cap Model and Marshall's Plastic Model

Pile cap plasticity analysis was performed, and the results were compared against experimental results and Marshall's plastic model.

For the cap model, the strain value of the clay was taken as 0.02 for ε_{50} and 0.06 for $3\varepsilon_{50}$. Cap plasticity and cap hardening parameters are required. Figure 6.3 shows the input data used. Cap hardening input used was similar to the plastic stress-strain curve used for Marshall's plastic model but the strain values used are different. Each parameter explanation are provided in the last column.

Table 6.3 Clay parameters input for cap plasticity model

Clap plasticity of the model input data	**Input used**	**Note:**
Elastic modulus (kPa)	2150	Ec/c = 50 ~ 200
Poisson's ratio	0.4	This value can be 0.3 ~ 0.45
Angle of friction (degrees)	20	Typical angle of friction for clay
Cap eccentricity	0.1	Cap eccentricity parameter, *R*. Its value must be greater than zero (typically $0.0001 \leq R \leq 1000.0$)
Initial yield surface	0	Initial yield surface size, α_0 (units of FL^{-2}). Abaqus ignores this data item if you have specified a value for Intercept.
Transition surface radius	0	Transition surface radius parameter, α. Its value should be a small number compared to unity. If you leave this field blank, the default is 0.0 (i.e., no transition surface). If you include creep properties in the material model, you must set α equal to zero.
Flow stress ratio	1.0	Ratio of the flow stress in triaxial tension to the flow stress in triaxial compression, *K*. $0.778 \leq K \leq 1.0$. If this value is left blank or set to zero, a value of 1.0 is assumed.

Cap hardening is sub-cap plasticity. Yield stress and volumetric plastic strain in the cap hardening were entered for the cap plasticity. The values used are shown in Table 6.4. The strain is extracted from values suggested in several papers and soil mechanics books, including

Matlock (1970). Very soft clay strain values are suggested as 0.02. The clay capacity was obtained from the Sabine River mouth's vane shear strength of 14.4 kPa (300 psf).

Table 6.4 Yield stress and volumetric plastic strain

Yield Stress (kPa)	Vol Plas Strain
7.2	0
14.4	0.02
28.73	0.06
28.74	0.18

Note:

Yield Stress - Value of the hydrostatic pressure stress at yield, p_c.

Vol Plas Strain - Absolute value of the corresponding volumetric plastic strain.

For Marshall's plastic model, the strain value of the clay was taken as 0.005 for ε_{50} and 0.015 for $3\varepsilon_{50}$. Compressive strength of the clay was the same as that of Matlock's Sabine clay, 28.74 kPa. The cap hardening stress-strain and plastic stress-strain curves used for cap plasticity and Marshall's plastic model respectively are shown in Figure 6.11

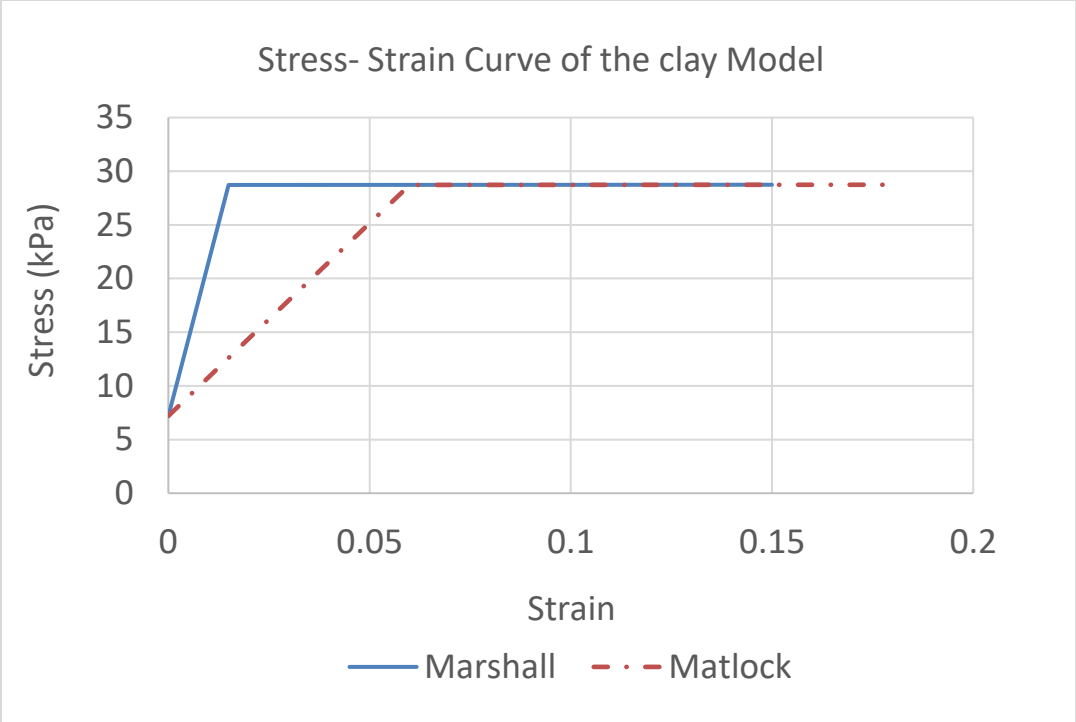

Figure 6.11 Stress strain curve for the plastic clay model

6.5 Mesh Size Study

A finer and coarser mesh of pile in clay was studied. For the finer mesh model, the mesh size around the pile was 6cm wide and 10cm long, 16 elements around the pile for pile diameter 31.9cm with a thickness of 1.27cm. Pile length was 12.8m (40 ft). Mesh size in the clay model around the pile was 20cm. For a coarser mesh model, there are 12 elements around the pile (10cm) and the length of the mesh size along the pipe was 20cm. Mesh size in the clay model around the pile was 25cm. C3D8R 8-node linear brick elements are used. FE analyses for different mesh sizes were performed using cap plasticity of clay model and the results are plotted in Figure 6.12.

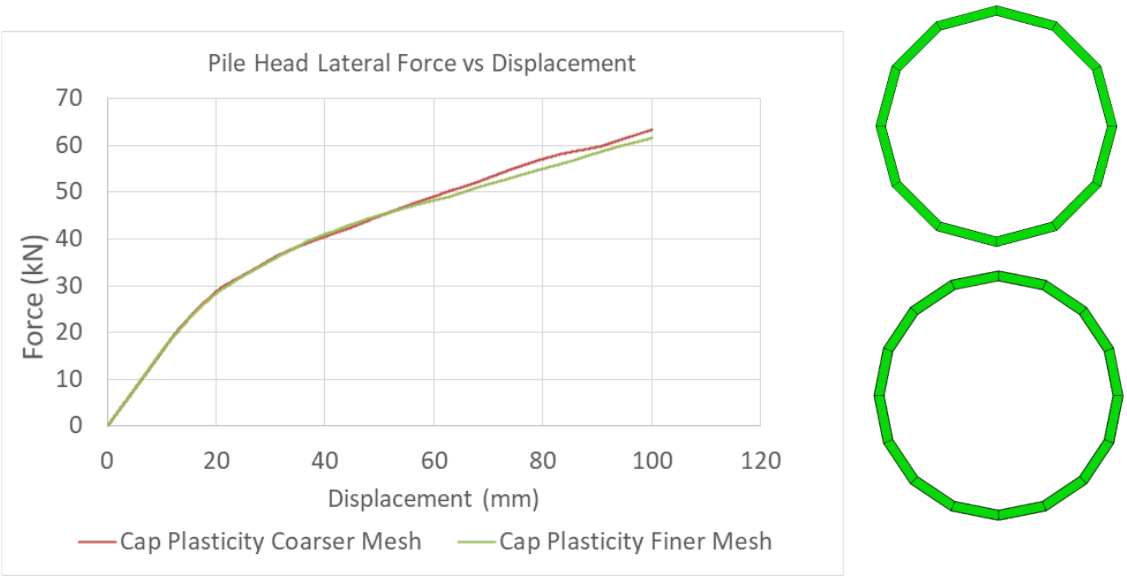

Figure 6.12 Force-displacement analysis results of different mesh sizes

Stress analysis results of different mesh sizes are also shown in Figure 6.13.

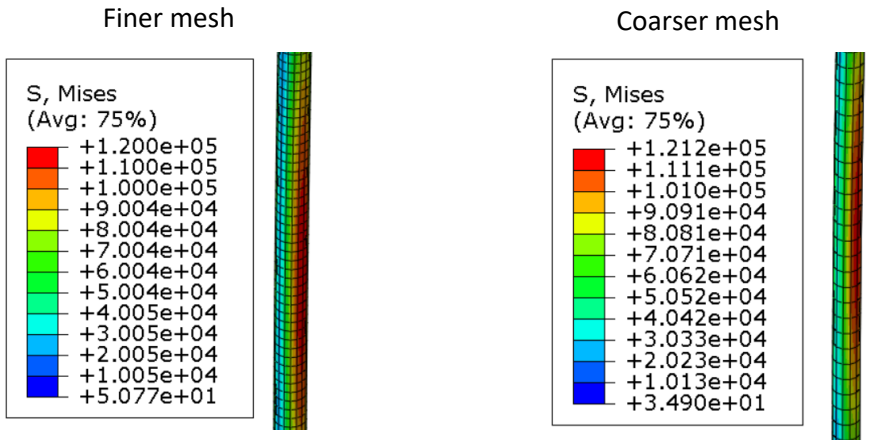

Figure 6.13 Stress analysis results of different mesh size

It can be seen from the lateral force vs displacement plot that finer mesh and coarser mesh sizes do not have much difference in analysis results. This is also the same for stresses – both coarse and finer mesh sizes show comparable analysis results. Rather, the finer mesh consumed a significant amount and time and caused several convergence issues. To resolve the

issues, loads increments, analysis times, mesh, etc. need to be adjusted. Thus, it can be concluded that, as long as the mesh size (width) is lesser than or equal to 10% of the tubular circumference, the load-deflection result is acceptable. The length of the mesh size can be 2 times the width. Stresses developed in the piles also appear to be comparable for the two mesh sizes.

The analysis was further performed using the finer mesh sizes for both the cap plasticity model and Marshall's plastic model. The analysis results are plotted in Figure 6.14.

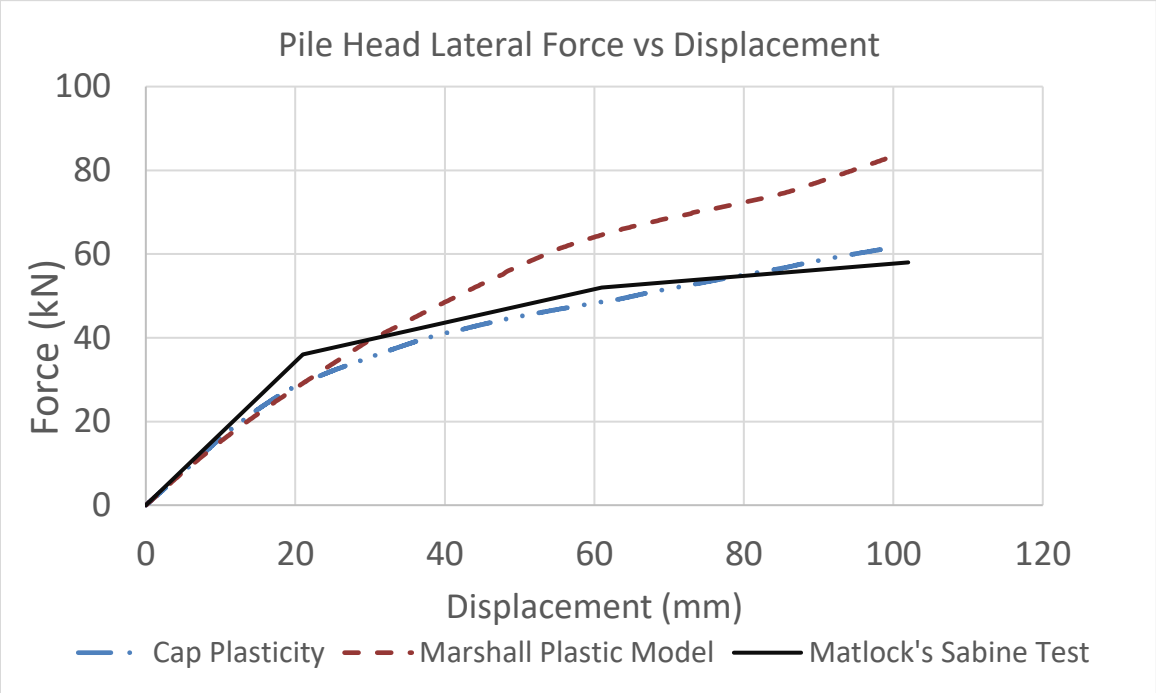

Figure 6.14 Analysis results for cap plasticity model and Marshall's plastic model

FE analysis with Marshall's plastic model appears to have a much larger displacement capacity compared to the test result as the applied load increases. The lateral load capacity is 40% larger than Matlock's test at 10cm pile head displacement. The difference in capacity appeared to start to deviate when the clay's stresses reached the elasticity limit. The clay plastic model appears to be almost perfectly matching the test result but slightly higher as the load

increases. The initial stiffness is well predicted with no imperfection included. However, the slight deviation results could also be due to the clay modus of elasticity ranges of choices, and the stress-strain curve model of the plastic soil. One of the reasons Marshall's clay capacity has a much larger lateral capacity is because the strain values used were small and these strain values represent stiff clay in several papers and books. On the other hand, the cap model used soft clay strain values which represent the actual strain value in the soft clay test.

6.6 Studies on Different Clay Stiffnesses

The composite section was tested in different clay stiffnesses, which are stiff clay, medium clay, and soft clay. The stiff clay was 4000 psf, medium clay was 1200 psf and soft clay was 120 psf. The results were plotted in Figure 6.15 and Figure 6.16. The von Mises stresses here are in megapascal.

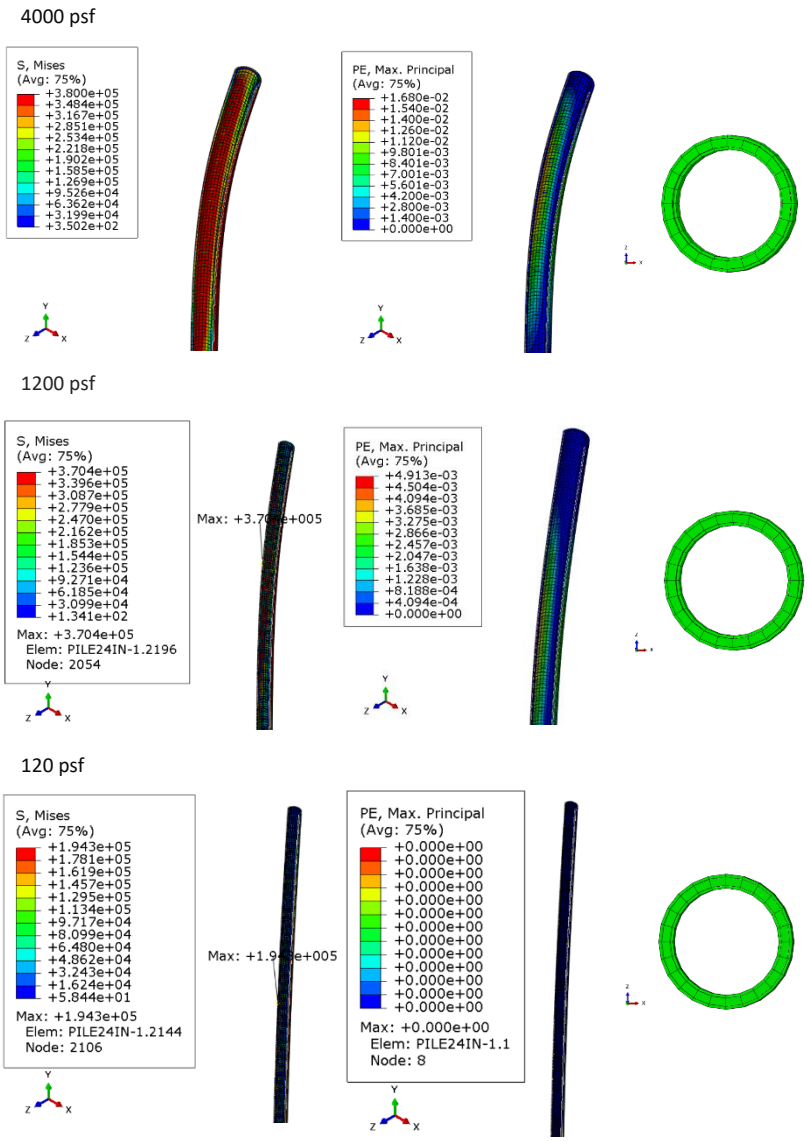

Figure 6.15 Analysis results in different clay stiffness

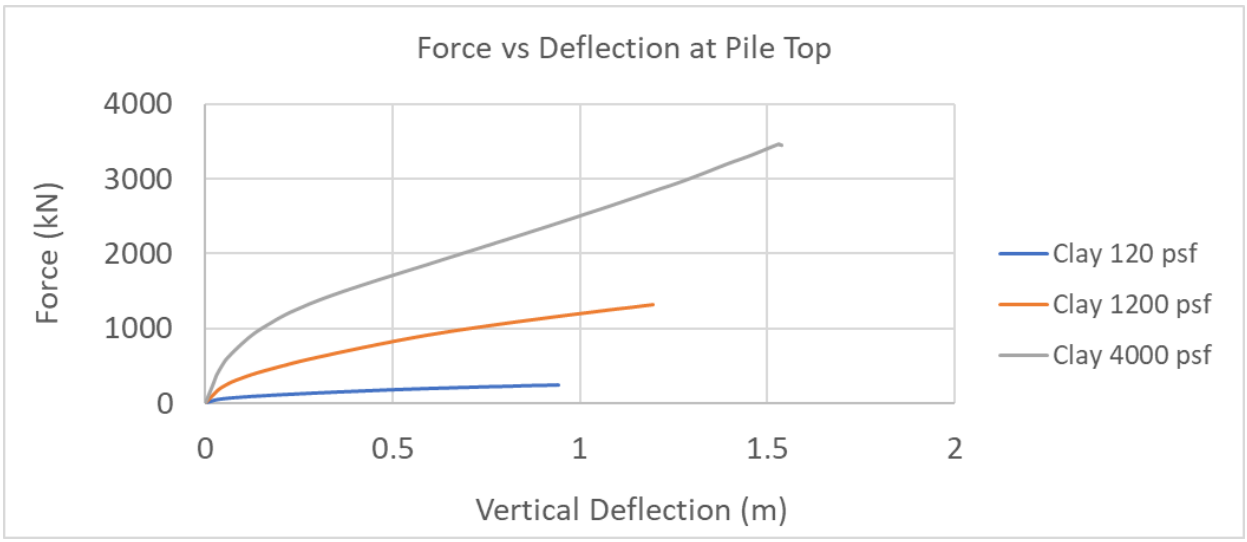

Figure 6.16 Analysis results comparison in different stiffness

Using the equation for API RP 1111 (1999), ovality can be calculated as

$$\delta = \frac{D_{max} - D_{min}}{D_{max} + D_{min}}$$

The inner pipe maximum inside open diameter was 48.3545cm and the minimum distance was 47.3671cm. Ovality for the biggest load capacity with stiff clay 4000 psf was 1.03%. For 4000 psf, the strain value in steel is 6.8% close to that of Marshall's (2004) calculation. However, ovality is still small. The stiffness of the polymer used here is a tenth of that of steel's Young modulus. Smaller than this value does not really add overall stiffness to the composite. This result was found when the clay compressive strength was kept constant at 1200 psf and when the stiffnesses of polymer varied.

It can be seen from the plot above that the pipe-in-pipe with polymer-filled composite performs very well in stiff clay or stiff soil. The FE analysis has a convergence issue in softer clay. It could be due to failure in the clay which causes the structure to be unstable.

6.7 Composite Double-wall Pipes in Clay

Double-wall composite pipe 24x0.5inch and 20x0.5in was re-analyzed for the same as equivalent single-wall pipe, using slightly coarser mesh. The stress, strain, and deflection of the pipe are shown below. The stress in steel is 378.5MPa and the strain is 1.43%. The halfpipe deflection is 2.134m. The total offset when the two composite pipes are connected is 4.27m as shown in Figure 6.17. The deformation shown for the pipe displacement is two times the actual deformation so that the comparison with single-wall pipe will be the same ratio.

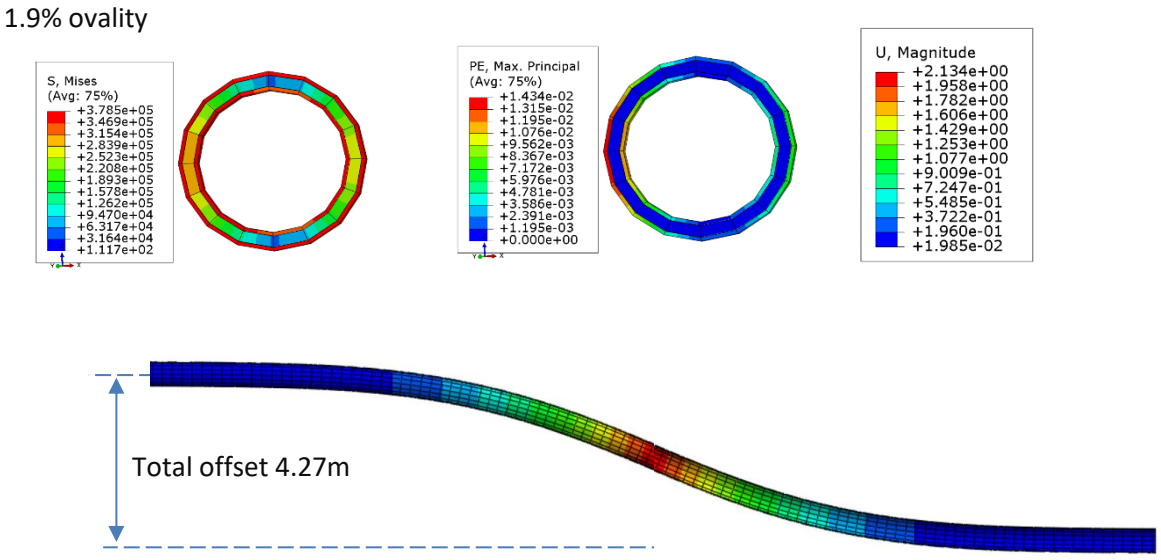

Figure 6.17 Double-wall composite pipe in clay analysis result

6.8 Single-wall Pipes in Clay

Single-wall pipe with a thickness 6.35cm which is the same as the total thickness of SPS section was also analyzed. The strain was limited at 2% and at this stage, and the total pipeline deflection was 4.16m. The pipe ovality was 5.3% and the steel section was in the plastic stage. The stress analysis result is shown in Figure 6.18.

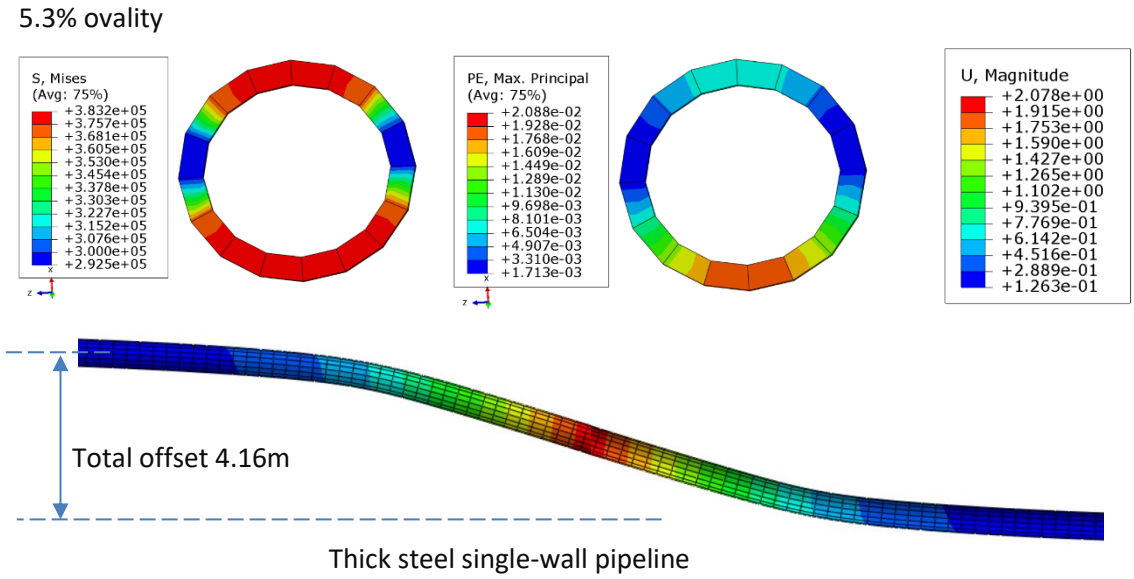

Figure 6.18 Laterally loaded single-wall pipe analysis results in clay

CHAPTER 7 BEAM ANALYSIS IN AIR

In this chapter, simply supported beams are analyzed without clay for the single and double-wall composite pipes. Four points loadings and rotations are applied for the beam bending. These analyses are necessary because the pipe embedded in clay in Chapter 6 did not have sufficient fine mesh. Thus, failures such as wrinkles were not observed. This beam analysis in the air without clay allows to have finer mesh size and the beam can also rotate larger until it fails. Hence, the detailed failure of the beams can be observed.

In the analysis, composite beams are analyzed as unbonded between steel-polymer-steel materials, bonded between steel-polymer-steel materials, different stiffnesses of the polymer grout, change of annulus thicknesses of the composite pipes, and the equivalent section of the single-wall pipes are analyzed, comparison of double-wall composite pipes and single-wall pipe analysis are investigated, and the FE analysis results are observed in areas such as ovality, stress, strain, and wrinkles.

7.1 Single-wall Pipe

The simply supported beam was tested and the analysis failure was observed.

7.1.1 Four Points Loads Test on Imperfect Welded Tubular 50.8x1.27cm

This study is a hinge angle on an imperfect weld connection on a steel pipe. Two sections of single-wall pipes were connected by weld. A cone is modeled between the pipe that represents weld. The cone length is 1.27cm, the same thickness as the pipe. The first section is 50.8cm and the second section is 0.5% smaller. This is to create a real construction scenario of an offshore pipeline. In the Abaqus model, the connections between pipes were tied. Reference points were created at the center of the pipes at each end. The reference point is tied to a pipe

section using the rigid body. One end is pinned (111000) and the other end is a roller (110000). Lateral movement in the X direction is restrained along the pipes. Vertical displacements in the Y direction at a third point in two locations were applied as shown in Figure 7.1.

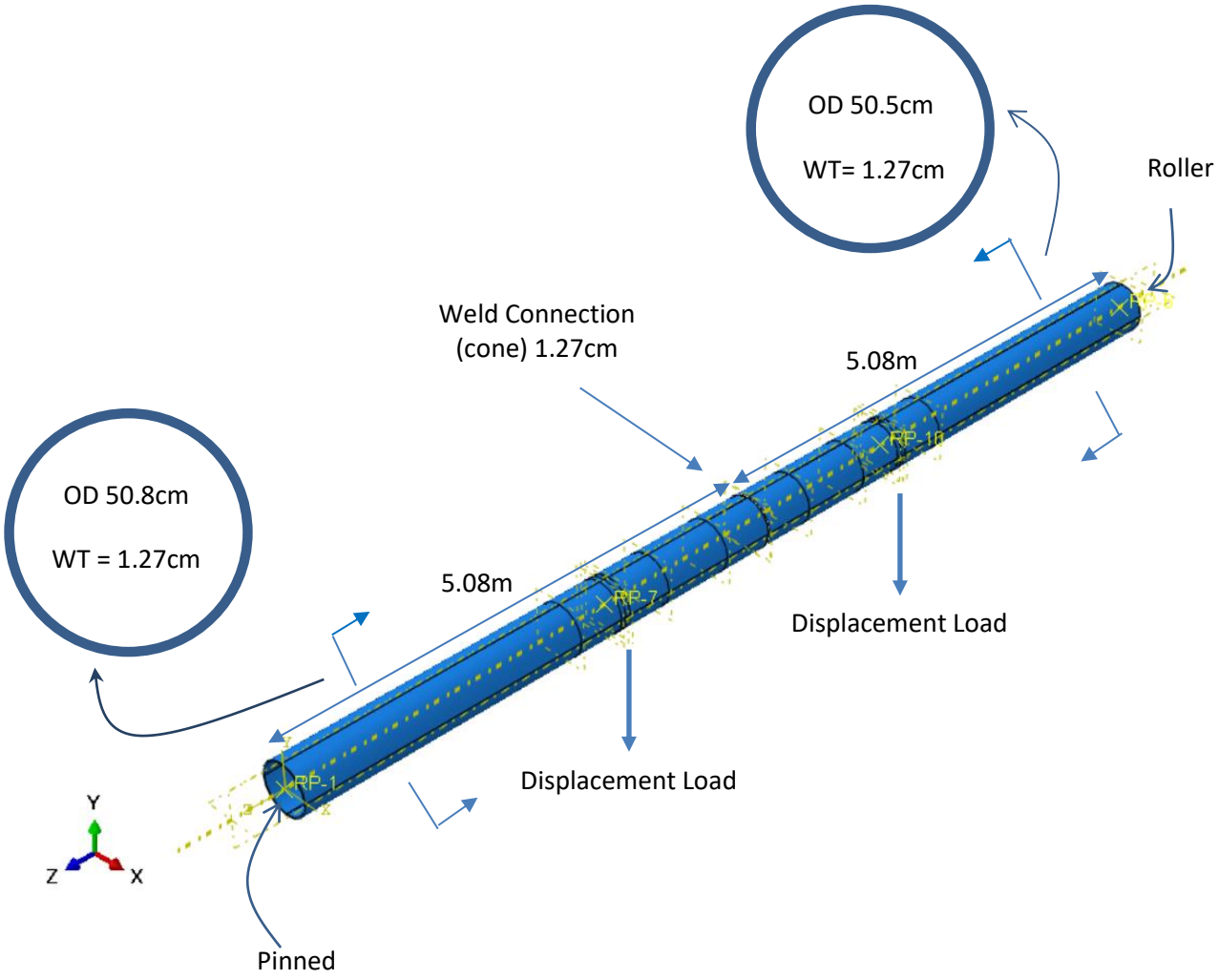

Figure 7.1 Simply supported four points loading

7.1.2 Materials Used

The stress strain curve of the steel used is shown in Figure 7.2. The steel pipe yield strength is 350 MPa (50 ksi) and elastic modulus is 200000 MPa (29000 ksi) and poison ratio is 0.25.

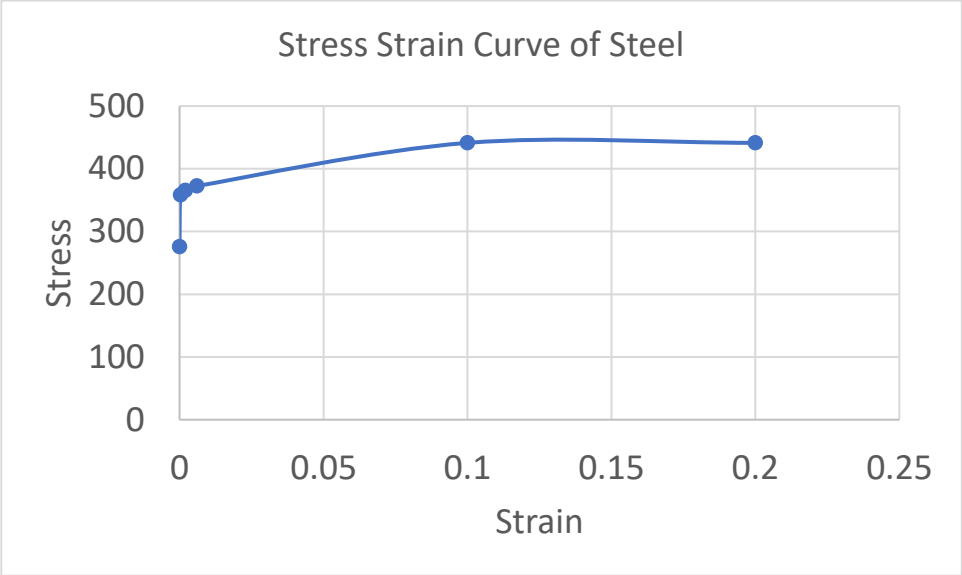

Figure 7.2 Steel stress-strain curve

7.1.3 Mesh and Results

Mesh size of 3cm were found to be sufficient for analysis results accuracy and expected failure were found in the pipe. Thus, 3cm mesh sizes were used at critical locations. Displacement at two equidistant locations were applied until the pipe buckled and failed. The analysis results are provided in Figure 7.3.

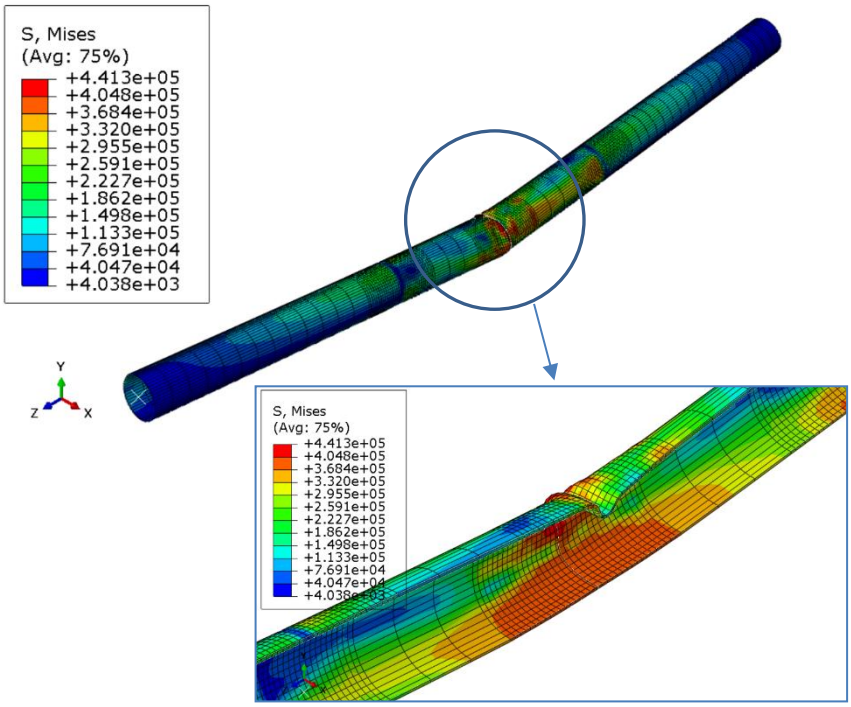

Figure 7.3 Simply supported beam analysis results

The maximum Von Mises stress reached an ultimate capacity of the pipe, 441 MPa can be seen in the analysis results. Plots of vertical displacement at mid-point again vertical displacement at two loading points are plotted in Figure 7.4. The pipe buckled at the midpoint of the tubular beam and closer to the weld.

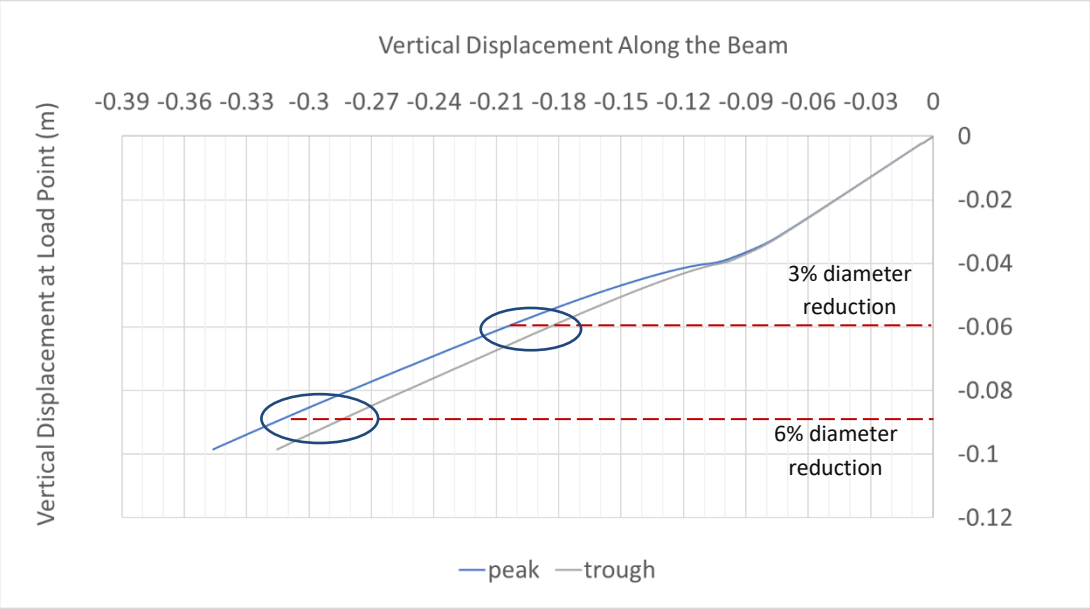

Figure 7.4 Deflection curve at load point vs deflection at the midpoint of the beam

At the loading point, nonlinear behavior was observed at the downward displacement of 0.04m. There is where the local buckling started. The tubular beam span was 5.08m (excluding weld length of 1.27cm). Displacement divided by the beam span (2*0.09/5.0) gives a hinge angle of 0.036 radians. The hinge angle of 2.06 degrees is obtained after conversion to degrees. The stress and strain results for 3% and 6% are shown in Figure 7.5.

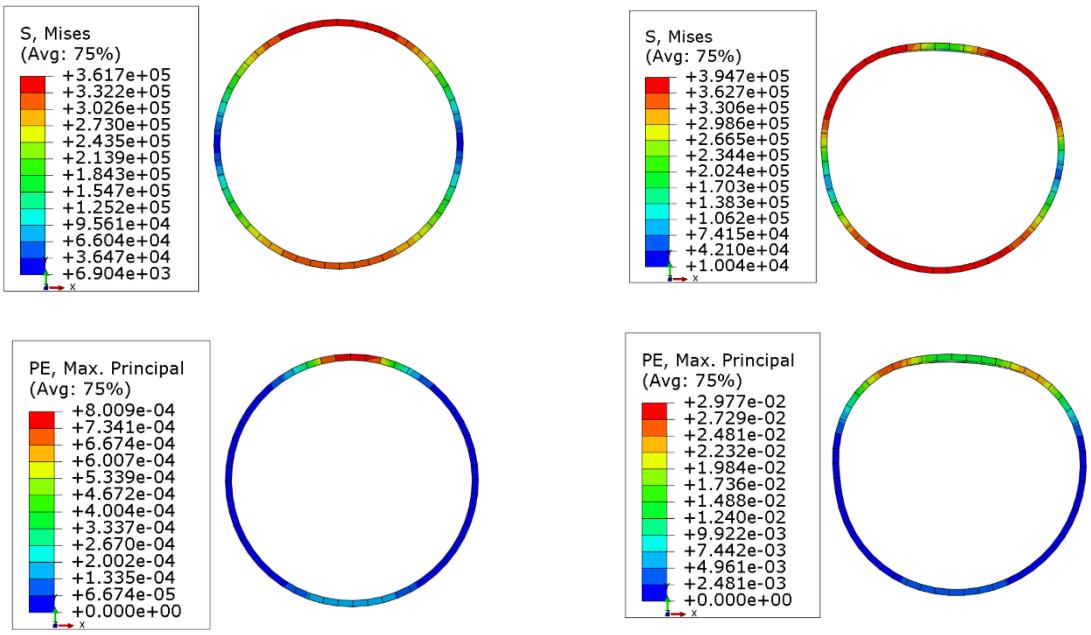

Figure 7.5 Deformation and stress of the pipe at 3% and 6% diameter reduction

At 6% diameter reduction or 9cm displacement at load point, the maximum inside diameter was 49.03cm and the minimum distance was 46.61cm. Hence the ovality was 2.53%. At 3% diameter reduction or 6cm displacement at load point, the maximum inside diameter was 48.32cm and the minimum inside diameter was 48.16cm. Hence, the ovality 3% diameter reduction was 0.17% and it is almost negligible. However, the pipe has gone into early plastic with 362 MPa and negligible strain.

7.2 Unbonded and Intact Composite Pipe

The beam span was 3.6127m long. Two vertical displacement downward loads were being applied at 1.40m from each support. Mesh size was 3cm at the region of mid-section 40cm length of the tubular beam center, and 5cm near the load point for another 20cm on each side and then 10cm near the supports. There are 40 elements around the pipe. Mesh element types are C3D8R, an 8-node linear brick, reduced integration, hourglass control. The beam and boundary conditions are shown in Figure 7.6.

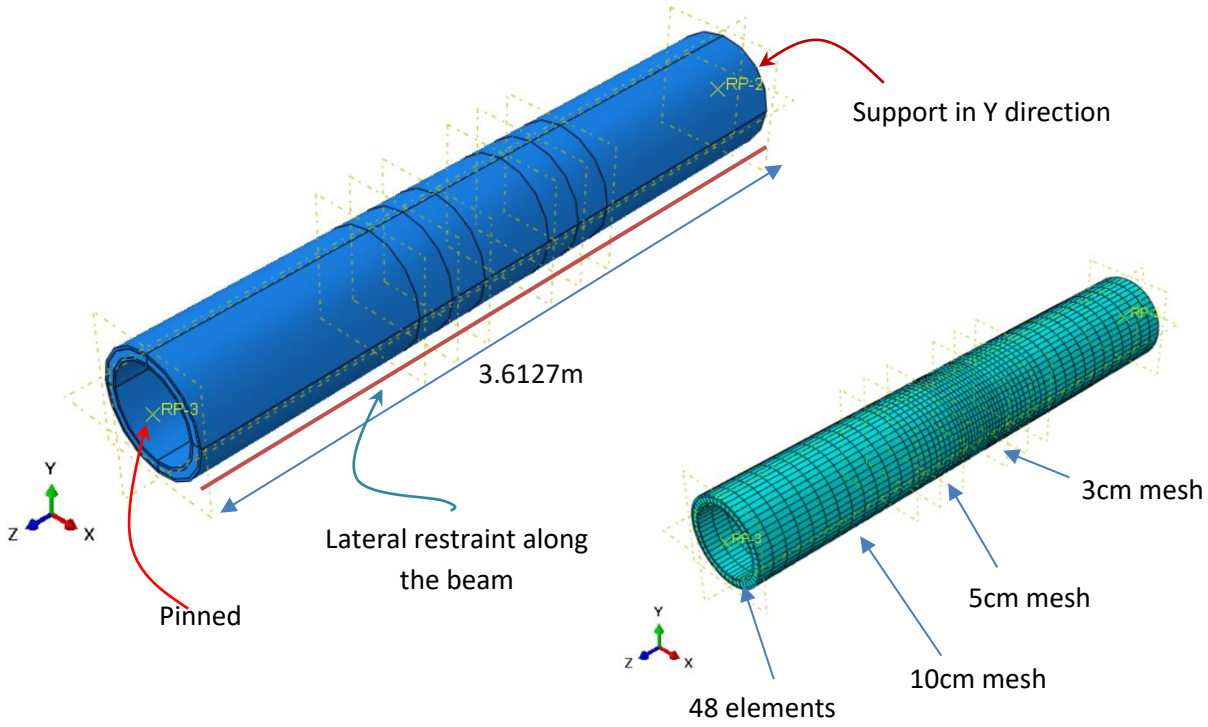

Figure 7.6 Simply supported 3.6127m long unbonded double-wall composite pipe

7.2.1 Analysis Result

Below result Figure 7.7 shows buckled failure of the composite pipe. Steel maximum plastic capacity is 441 MPa.

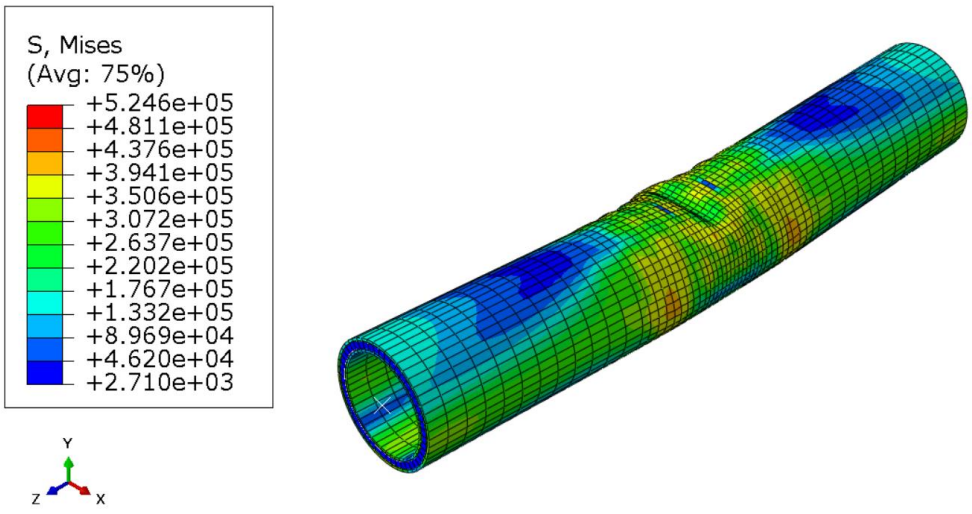

Figure 7.7 Failure result of the composite pipe

The result in Figure 7.8 shows failure at 399.5MPa. The deformed shape factor shown is 2 times the actual deformation. Wrinkles were observed at the compression side of the pipe. The largest wave formed at the mid-section of the composite beam. The wave gets smaller towards the supports, and it dissipates before reaching the support.

The plot in Figure 7.8 shows a deformed shape at a 3% diameter reduction. The maximum stress occurred at the outer pipe, and it was 399.5 MPa.

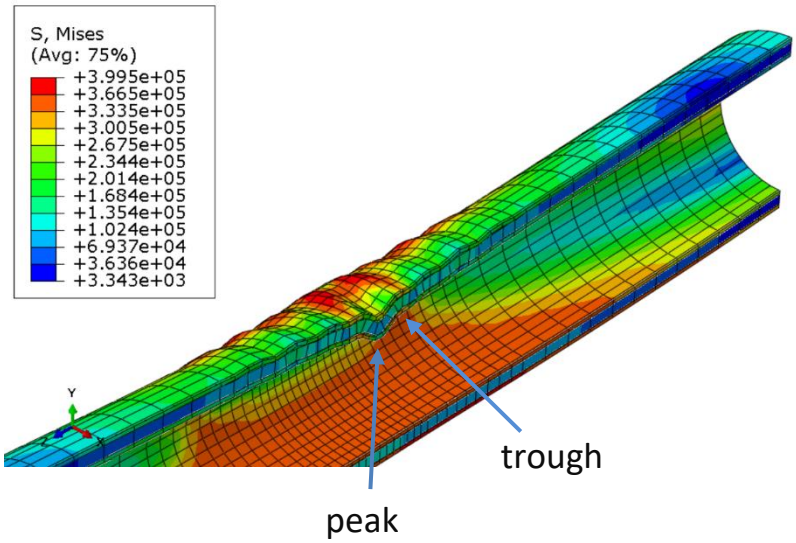

Figure 7.8 Failure results at 3% diameter reduction

Vertical displacement at mid-point vs at load point was plotted for stress 399.5MPa. The displacement plot was performed using the largest wave at mid-section at two points, peak and trough. The resulting plot is shown in Figure 7.9.

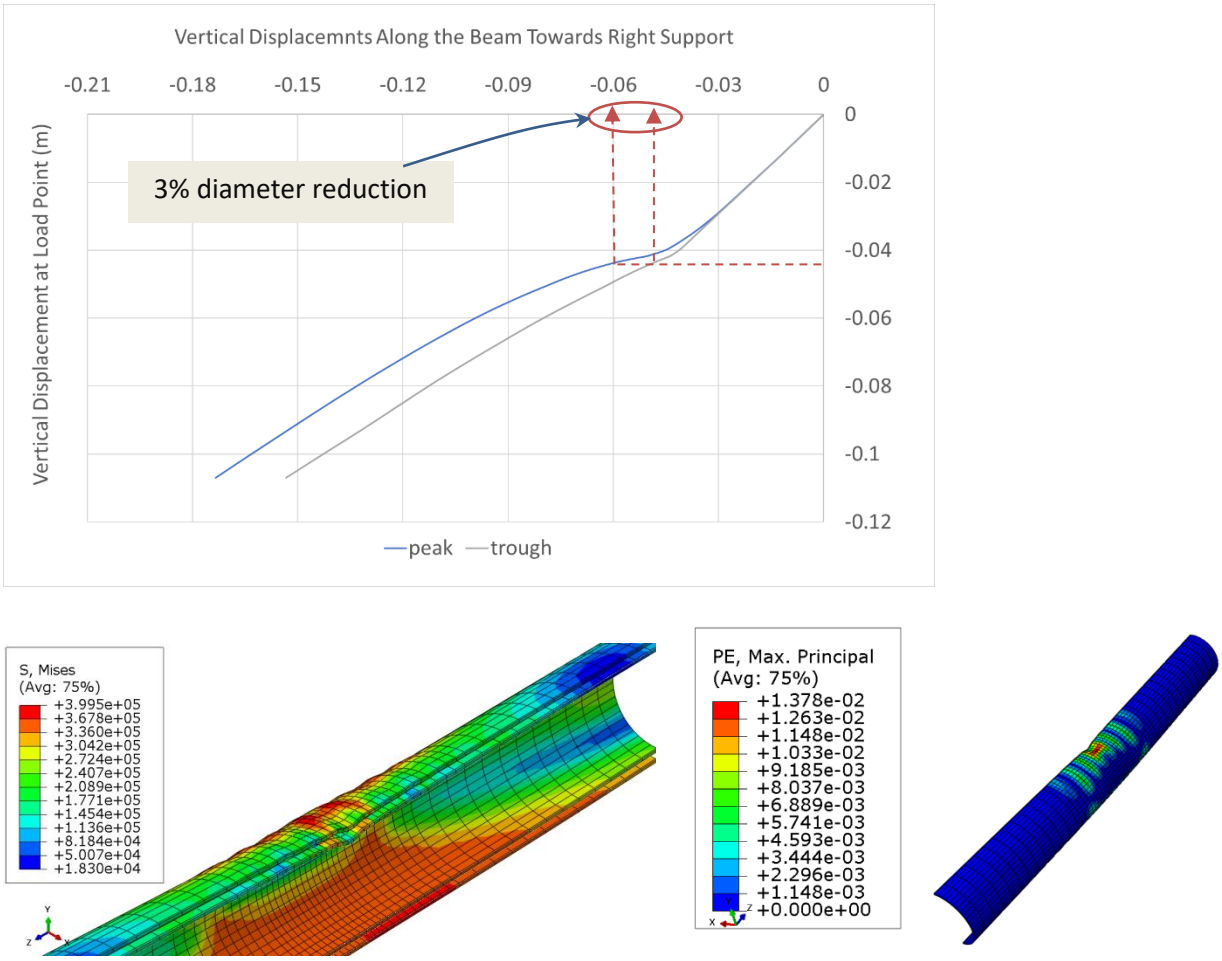

Figure 7.9 Displacement at load point vs displacement at midpoint of the beam and failure results

Local buckling started to appear at load point displacement of 0.03m (1.18 in). 3% diameter reduction occurred at load point displacement about 0.045m (1.77in), at von Mises stress 399.5MPa. 6% diameter reduction was never reached at these stress and displacement. The analysis required more displacement load to achieve 6% diameter reduction. It can be observed that 3% diameter reduction was reached by applying displacement load 15cm more (0.59in) from the first local buckling of the inner pipe. At the initial buckle at 0.03m load point displacement, the maximum stresses in the steel pipe stress was 386.5 MPa. The maximum strain at midpoint areas was 1.38%.

Figure 7.10 deformed shape at load displacement 0.03m was amplified by 2.0.

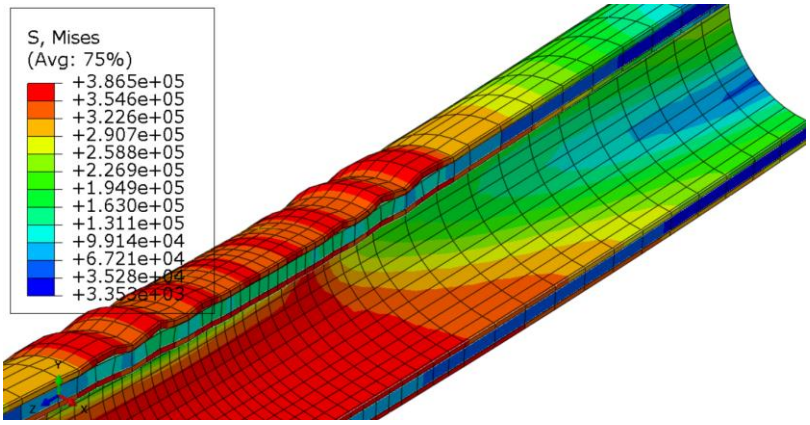

Figure 7.10 Results at the initial buckling of the inner pipe

Figure 7.11 shows maximum stress occurred in the polymer. There is a bigger wave at the middle part of the tubular beam. This is 6% diameter reduction deformed shape and the shape factor is 1.0.

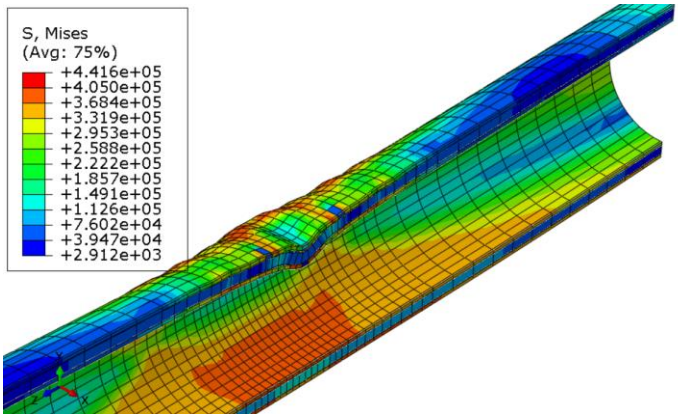

Figure 7.11 Results at 6% of the inner diameter reduction

Figure 7.12 is the vertical displacement at the mid-point, the largest wave at peak and trough. At the end of the curve at a maximum displacement load of 0.106m, the maximum stress in steel was 421 MPa. At this point, the polymer stress went beyond 441 MPa, which means failure occurred in the polymer. Maximum strain at this level was found to be 5.44% at the

loading points, and 2% at the mid-section local buckling. Marshall (2004) stated 6.4%, but it was a much longer pipe with large curvature.

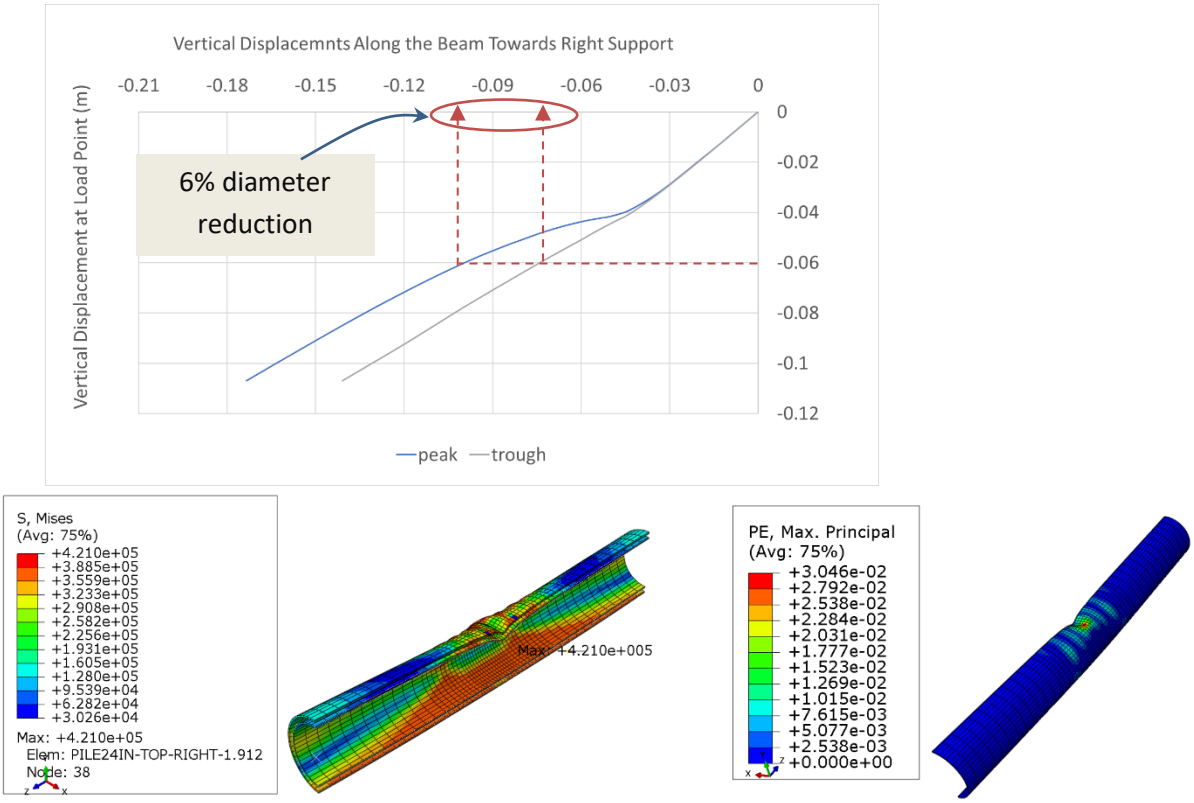

Figure 7.12 Displacement at load point against displacement at midpoint of the beam

6% diameter reduction occurred at about 0.06m displacements at load point. At this point, the maximum stress in the steel was 421MPa and the strain in the inner pipe was 3.05%

7.2.2 Further Analysis Failure Results

There was no visible local buckling at 352.8 MPa up to 367.1 MPa. However, at 367.1MPa, an initial wrinkle (local buckling) started to appear in the outer pipe. The plots are shown in Figure 7.13, 5 times the deformation. At 372.4 MPa, the initial local buckling started to form in the inner pipe and at 380.7MPa it becomes more visible. From the displacement at wrinkles and load point, it was more obvious that local buckling happed at vertical displacement

0.03m, and stress at 386.5 MPa. However, from the steel deformed plot, it appears the initial wrinkle started at 372 MPa. Plots of the stresses and deformed shapes are shown below.

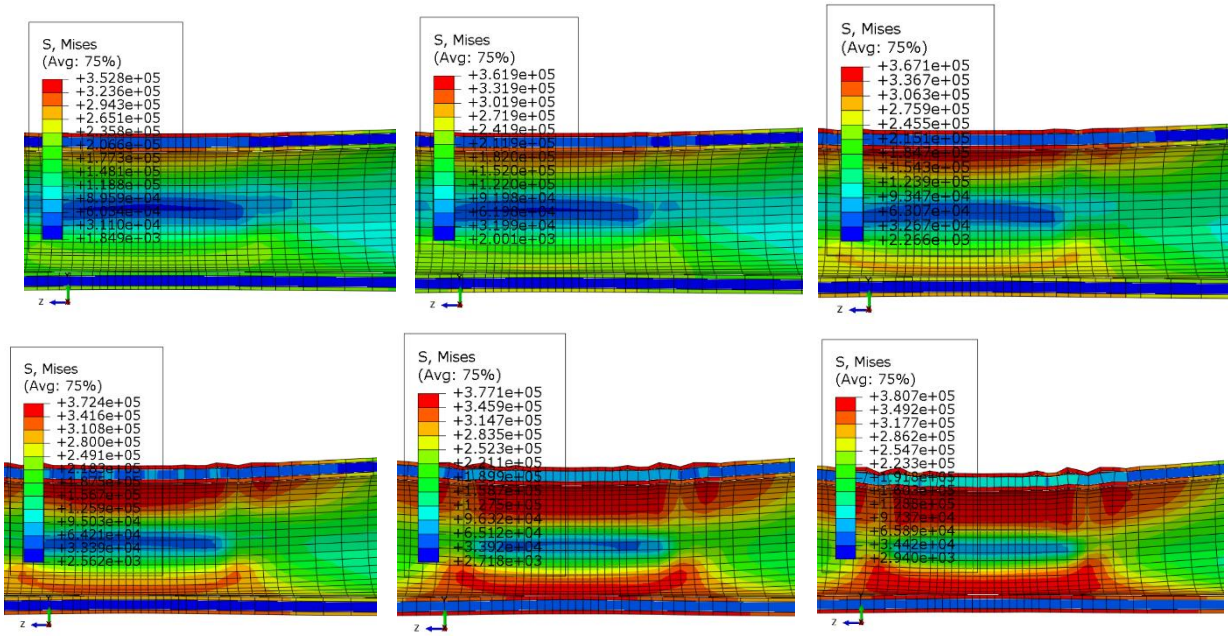

Figure 7.13 Progressive failure as the load displacement increases

From the pipe stress against load-displacement plot below, it can be observed that the inner pipe stress is still within elastic at 3% diameter reduction, and 370 MPa at 6% diameter reduction. The inner pipe never reaches ultimate steel yield strength utilizes only 84% of 441 MPa. Between 0.04m to 0.06m load displacement, there was a stress drop. This could be due to the buckling in the mid-section and loads were redistributed to some other parts of the section. This element was taken from the inner pipe mid-section at the largest stress element as shown in the plot in Figure 7.14. From the stress plot, it was observed that inner pipe stress reached 352MPa at the initial local buckling, and 355MPa at 6% diameter reduction. The maximum at the bottom tension at load-displacement 0.08m was 372 MPa. Overall, at 6% diameter reduction, the inner pipe stress utilizes only 80% of its ultimate capacity.

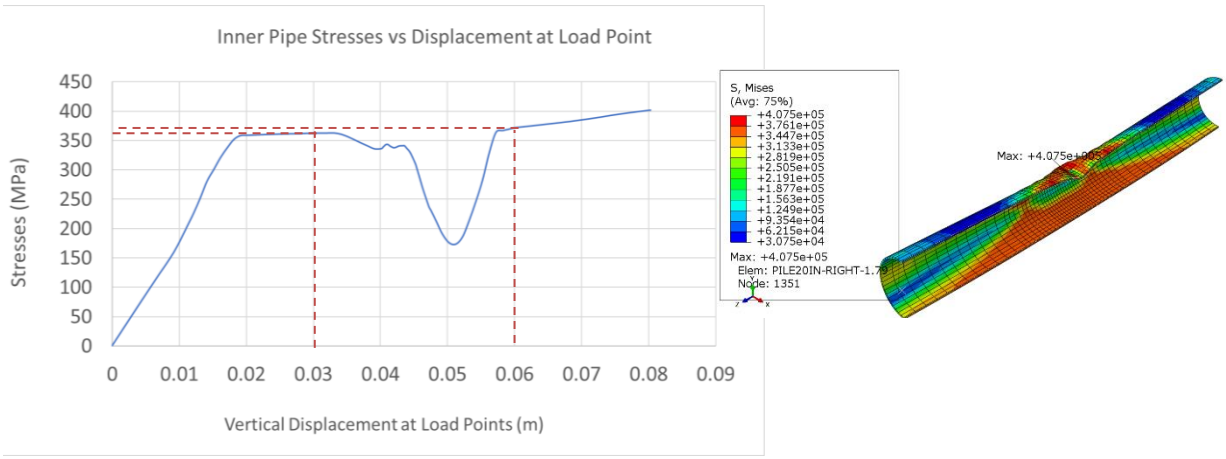

Figure 7.14 Von Mises stresses again displacement load

Figure 7.15 shows force displacement for the intact composite pipe at the mid-section. The load capacity at the initial local buckling was 4900kN, 5200kN at 3% diameter reduction, and 4700kN at 6% diameter reduction. After the initial buckling, it can be seen that there was not much load capacity left, only about a 6% increase in the load capacity the capacity reduces thereafter as the steel experiences more plasticity. The composite pipe's capacity slowly reduces after its inner pipe diameter is reduced by 3% and has reached the outer steel yield strength of 399.5 MPa and the inner pipe stress of 355 MPa.

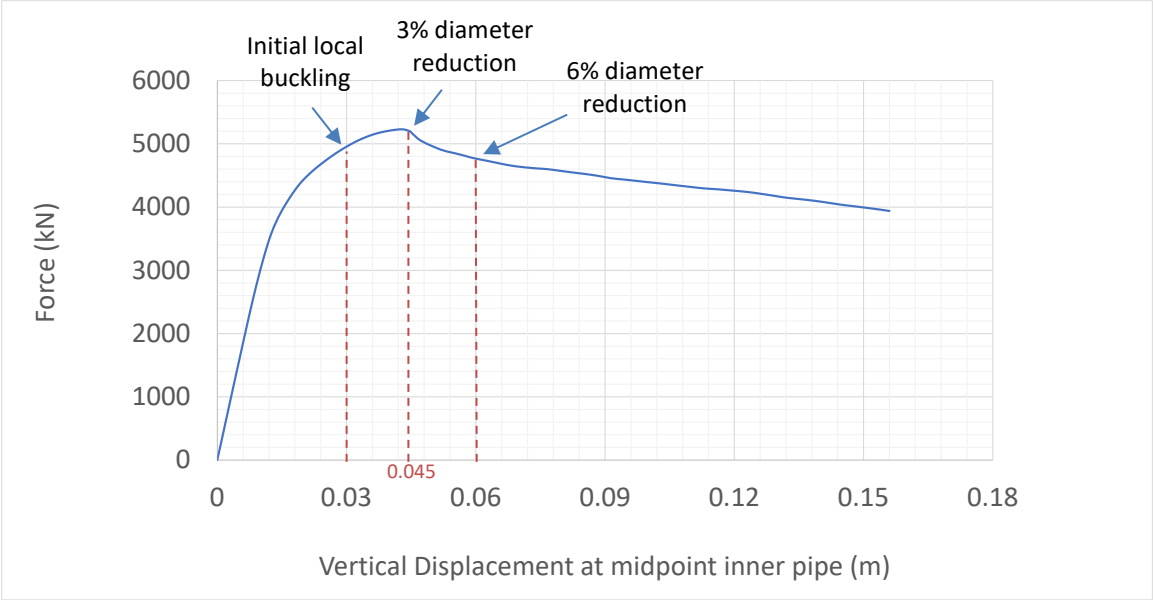

Figure 7.15 Load capacity of the simply supported unbonded composite section

Table 7.1 shows summary of the analysis results, including the total hinge angle.

Table 7.1 Hinge angle, stresses and strain of the unbonded perfect composite pipe

	Displacement at load point (cm)	Displacement at mid-point (cm)	Half beam length (cm)	Total hinge angle (degree)	Von Mises Stress in Steel (MPa)	Principal Strain (-)
Initial local buckling at 3cm load displacement	3.01525	3.1408	178.773	1.01	386.5	0.02618
3% diameter reduction	4.35187	7.7916	178.483	2.50	399.5	0.04202
6% diameter reduction	7.65973	12.7985	177.878	7.20	410.2	0.05442

7.3 Unbonded Imperfect Composite Pipe

The beam span was 3.6127m long. Two vertical displacement downward loads were being applied at 1.40m from each support. Mesh size was 3cm at the region of mid-section 40cm length of the tubular beam center, and 5cm near the load point for another 20cm on each side and then 10cm near the supports. There are 40 elements around the pipe. Figure 7.16 shows beam assembly and the boundary conditions.

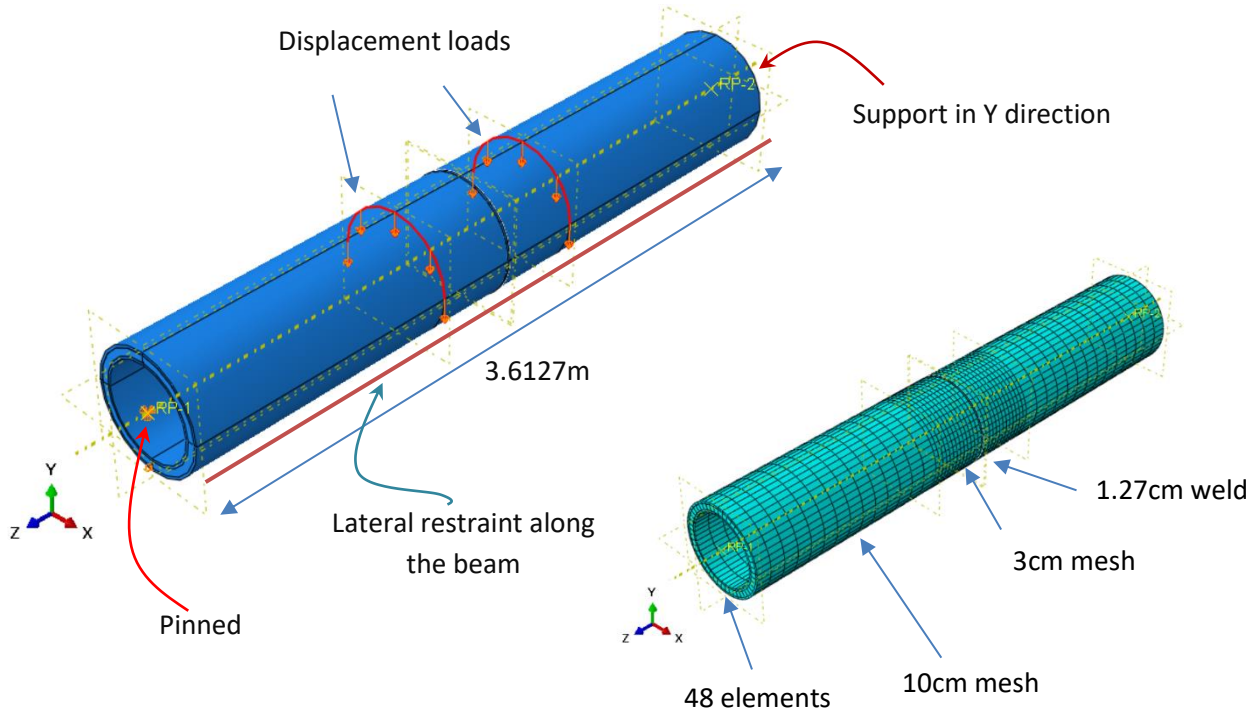

Figure 7.16 Imperfect unbonded composite section

7.3.1 Analysis Results

Figure 7.17 result shows the buckled failure of the composite pipe. Steel's maximum plastic capacity is 441 MPa. Maximum stress occurred in the polymer. However, the maximum stress in steel at this point was 428.8MPa. The deflection plot at mid-point against load point displaced is plotted below at the ultimate deformation.

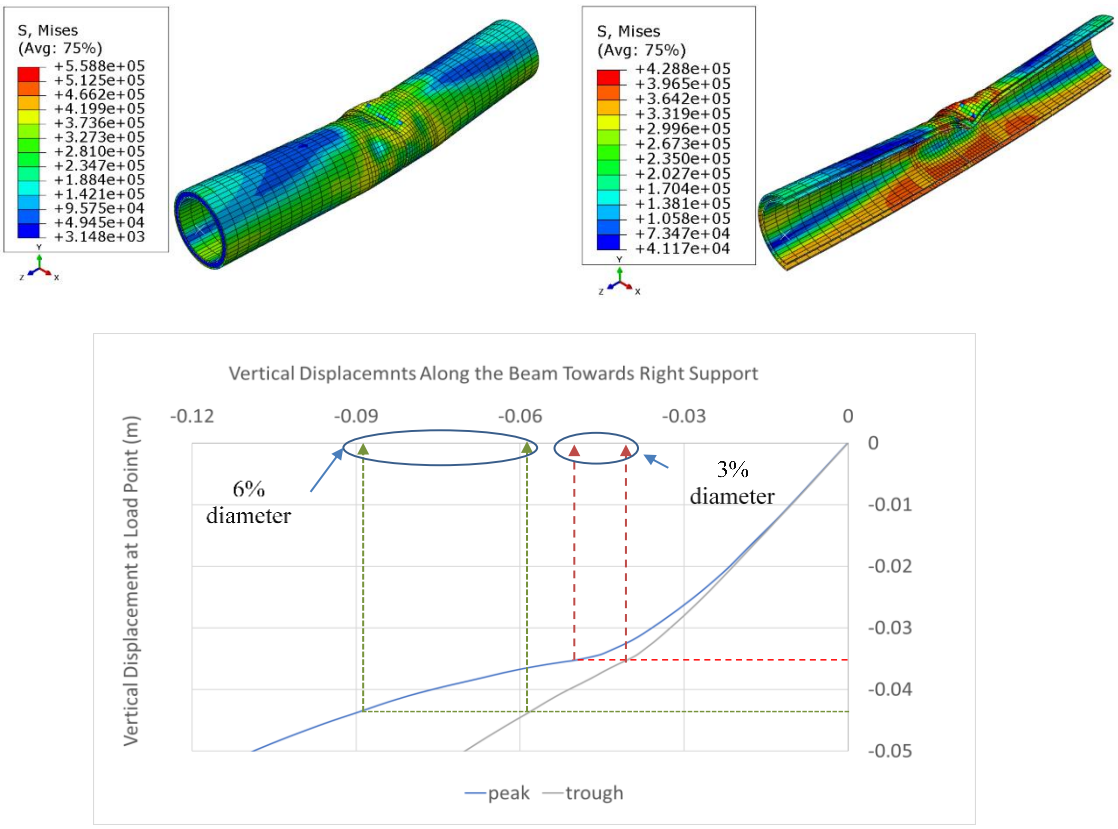

Figure 7.17 Displacement at load point against displacement at midpoint of the composite beam

From the plot in Figure 7.17, it can be observed that 3% diameter reduction occurred at 0.035m load displacement and 6% diameter reduction occurred at 0.044m load deflection. This is an approximation as there was just one big wave in the middle at the final beam deformation. More accurate plots will be plotted later.

From the bottom side displacement plot at peak and trough locations, there was no significant change of diameter in the two locations. In the analysis this part will be ignored, taking that there is no change in diameter due to the bottom side of the pipe deformation.

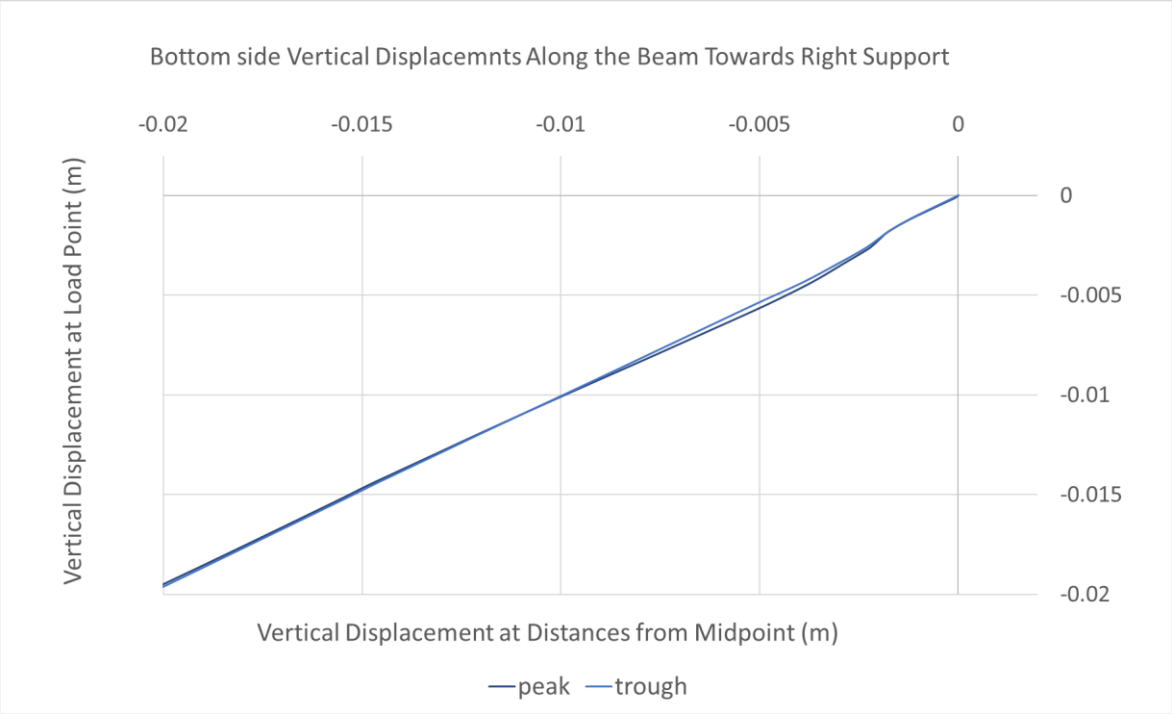

Figure 7.18 Displacement at the bottom side of the inner tubular pipe

Figure 7.19 deformed shape happened at 3% diameter reduction. The maximum stress occurred at the inner pipe weld connection, and it was 386.4MPa. The deformed shape factor shown is 2 times the actual deformation. Wrinkles were observed at the compression side of the pipe. The largest wave formed at the mid-section of the composite beam. The wave gets smaller towards the supports, and it dissipates before reaching the support. The strain was 0.02036 at the outer pipe loading point. However, the strain at the inner pipe was 0.01421 near the mid-section.

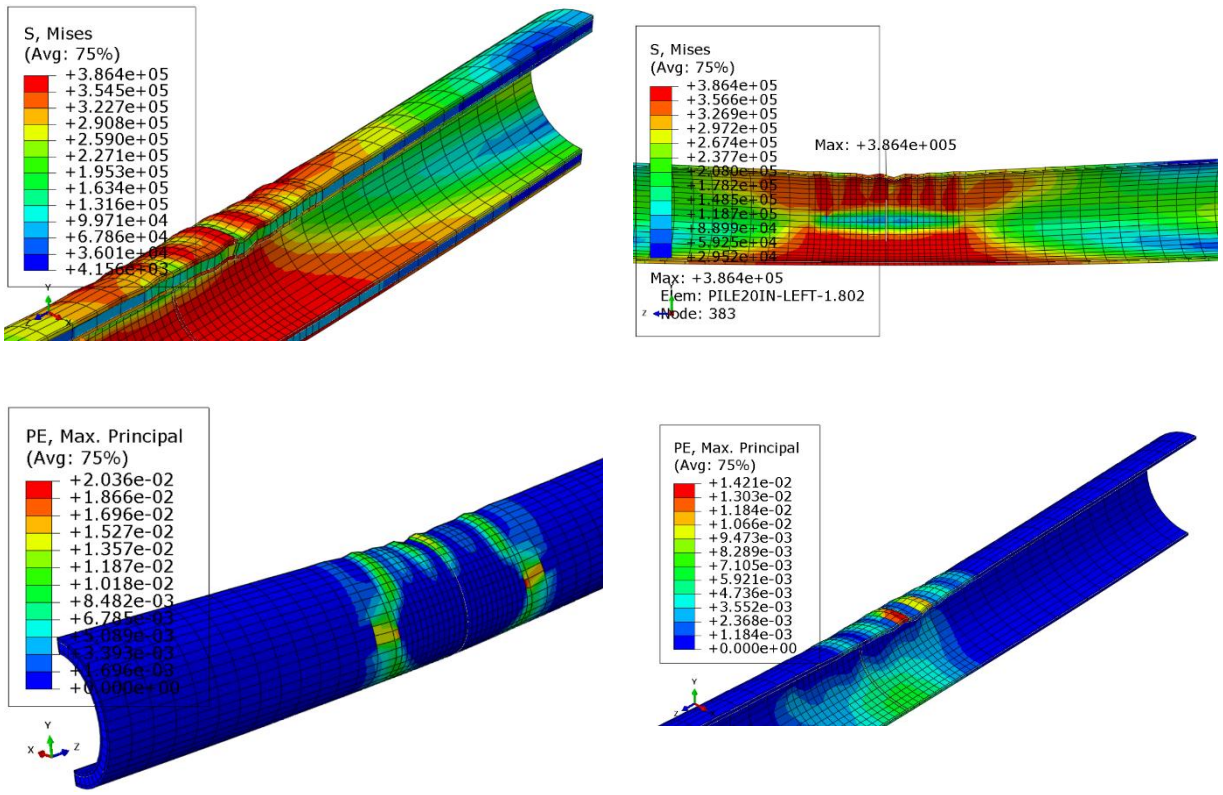

Figure 7.19 Stress and strain analysis results at 3% diameter reduction

Vertical displacement at mid-point against load point was plotted for stress 386.4 MPa. The displacement plot was performed using the largest wave at mid-section at two points, peak and trough. It was found in the analysis results that the local buckling started to appear at a load point displacement of 0.015m (0.59 in). 3% diameter reduction occurred at load point displacement about 0.035m (1.38in), at von Mises stress 386.4MPa. It can be observed that a 3% diameter reduction was reached by applying a displacement load 20cm more (0.79in) from the first local buckling of the inner pipe. At the initial buckle at 0.015m load point displacement, the maximum stress in the steel pipe was 374 MPa.

Figure 7.20 shows a deformed shape plot at load-displacement 0.015m, 5.0 amplification. The outer pipe can be seen buckled but the inner pipe started to experience initial local buckling.

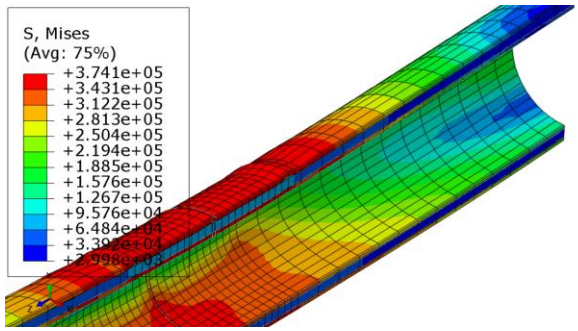

Figure 7.20 Initial buckling of the inner pipe

At this point of deformation, a more accurate plot was generated. Figure 7.21 is analysis results at 3% diameter reduction.

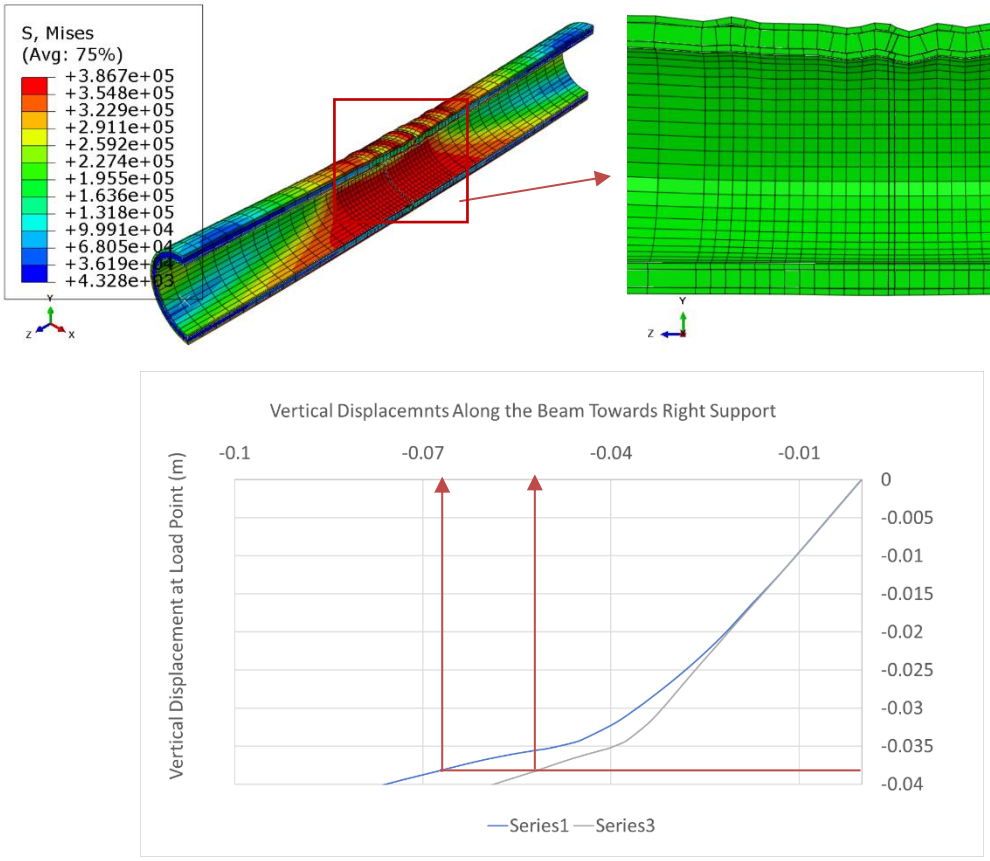

Figure 7.21 Displacement plot at 3% diameter reduction

Now, several smaller wrinkles can be seen on the compression side. Plotting the displacements of this will give a more accurate prediction of peak-trough joint displacement. 3% diameter reduction is now at load displacement of 0.038m, from the more detailed plot above. Figure 7.22 shows stresses at 3% diameter reduction, 2 times deformation.

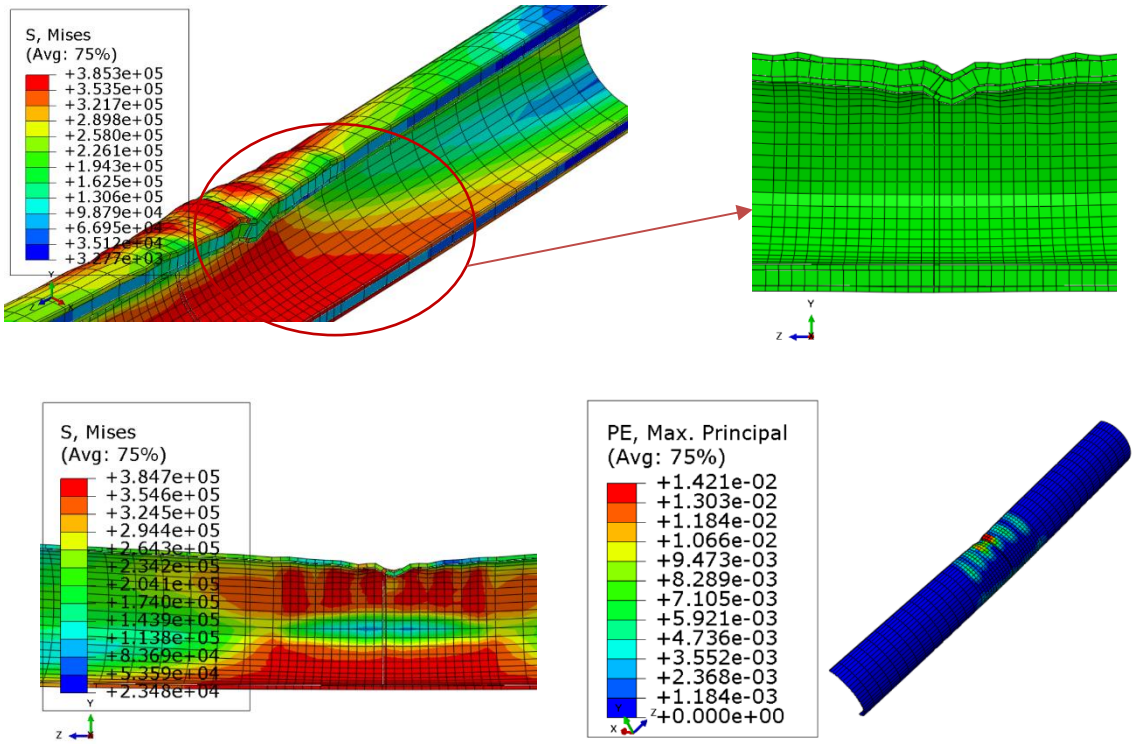

Figure 7.22 Stresses and strain at 3% diameter education

Maximum stress at 3% diameter reduction, the inner pipe stress was 385 MPa and the strain was 1.42%.

Figure 7.23 plot is the vertical displacement at mid-point, the largest wave at peak and trough. This is more accurate compared to the plot at the final displacement plot earlier. Now the load-displacement is 0.053m for 6% diameter reduction. The earlier approximation was 0.044m.

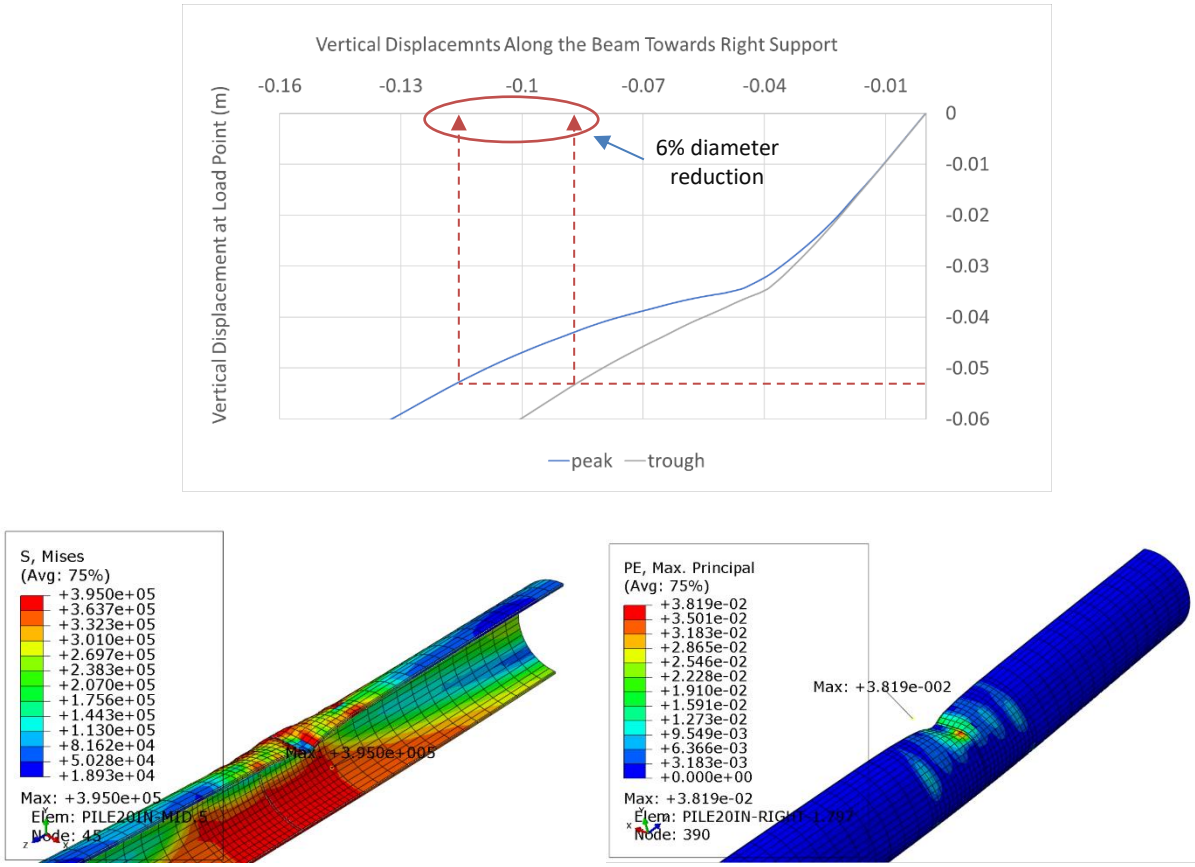

Figure 7.23 Displacement and failure results at 6% diameter reduction

From a more detailed plot, 6% diameter reduction occurred at about 0.053m displacement at load point. At this point, the maximum stress in the steel was 395 MPa in the inner pipe and the strain was 3.82%

7.3.2 Further Analysis Failure Results of Unbonded Imperfect Composite Section

This analysis shows stresses as loads increases. There was no visible local buckling at 355.6 MPa up to 367.2 MPa. However, at 377.9MPa visible wrinkle (local buckling) started to

appear in the outer pipe. The plots are shown below, 5 times the deformation. At 379.0 MPa, the local buckling started to form in the inner pipe, and at 380.7MPa the wrinkles become more visible. It was more obvious that local buckling happened at vertical displacement 0.038m, and stress at 386.5 MPa, and at this point the inner pipe diameter has reduced to 3%. Plots of the stresses and deformed shapes are shown in Figure 7.24.

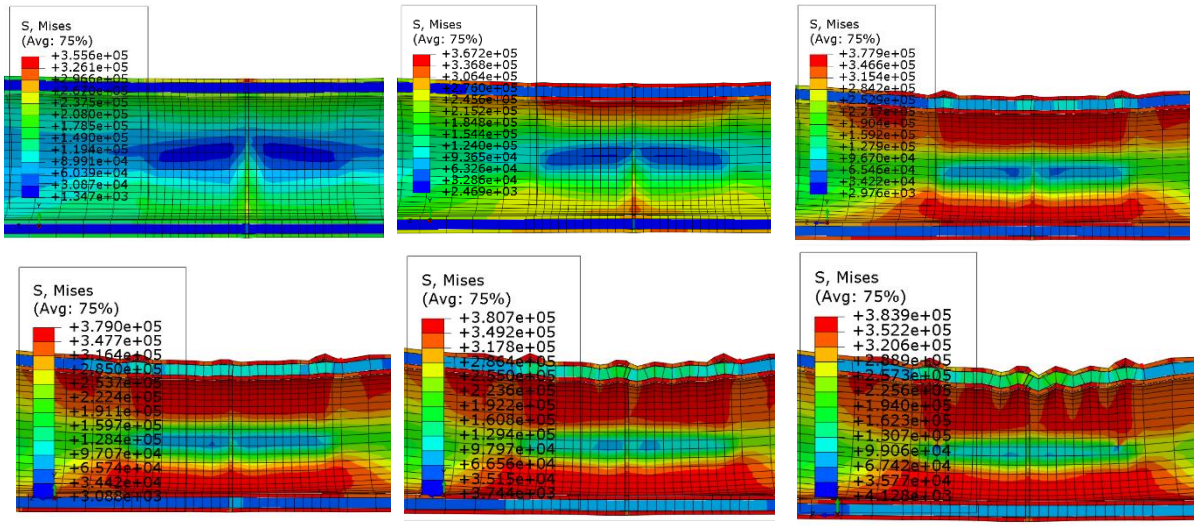

Figure 7.24 Progressive failure results

From the pipe stress against load-displacement plot below, it can be observed that the inner pipe stress is around 370 MPa at 3% diameter reduction, and 385 MPa at 6% diameter reduction. The inner pipe never reached ultimate steel yield strength and utilizes about 85% of 441 MPa at 6% diameter reduction. Between 0.04m to 0.06m load displacement, there was a stress drop. This could be due to the buckling in the mid-section and loads were redistributed to some other parts of the section, similar to intact composite section analysis. This element was taken from the inner pipe mid-section at the largest stress element as shown in Figure 7.25. An extrapolation line was drawn in the plot for stress estimation. From the stress plot, it was observed that in the inner pipe stress was about 350MPa at the initial local buckling, and close to 390MPa at 6% diameter reduction.

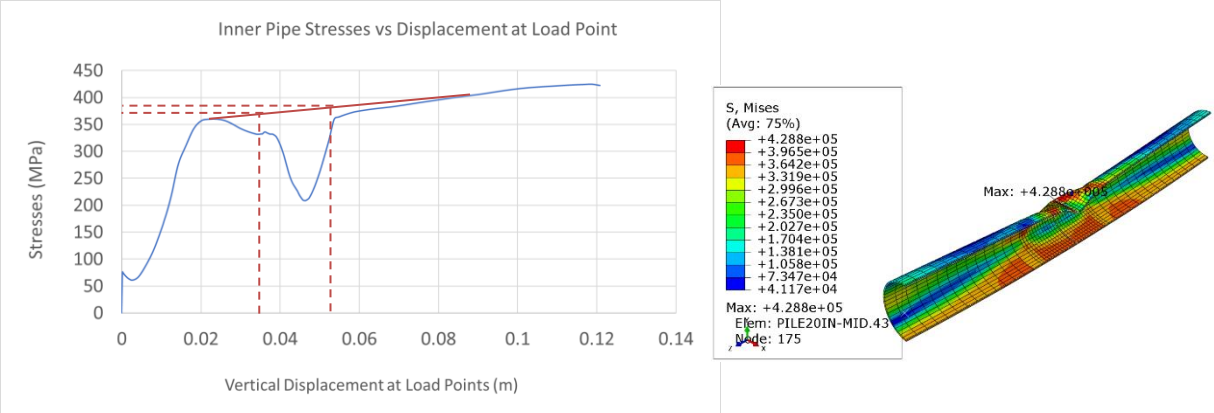

Figure 7.25 Stress plot of the inner pipe

Figure 7.26 plot shows force-displacement for the intact composite pipe at the mid-section. The load capacity was 4600 kN at the initial local buckling, 5000kN at 3% diameter reduction, and 4500kN at 6% diameter reduction. After the initial buckling, it can be seen that there was not much load capacity left with about a 16% increase in the load capacity. The load capacity reduces drastically thereafter. The steel experiences more plasticity. The composite pipes capacity reduces fairly rapidly after its inner pipe diameter is reduced by 3% and has reached both the outer and inner pipes steel yield strength of 385 MPa.

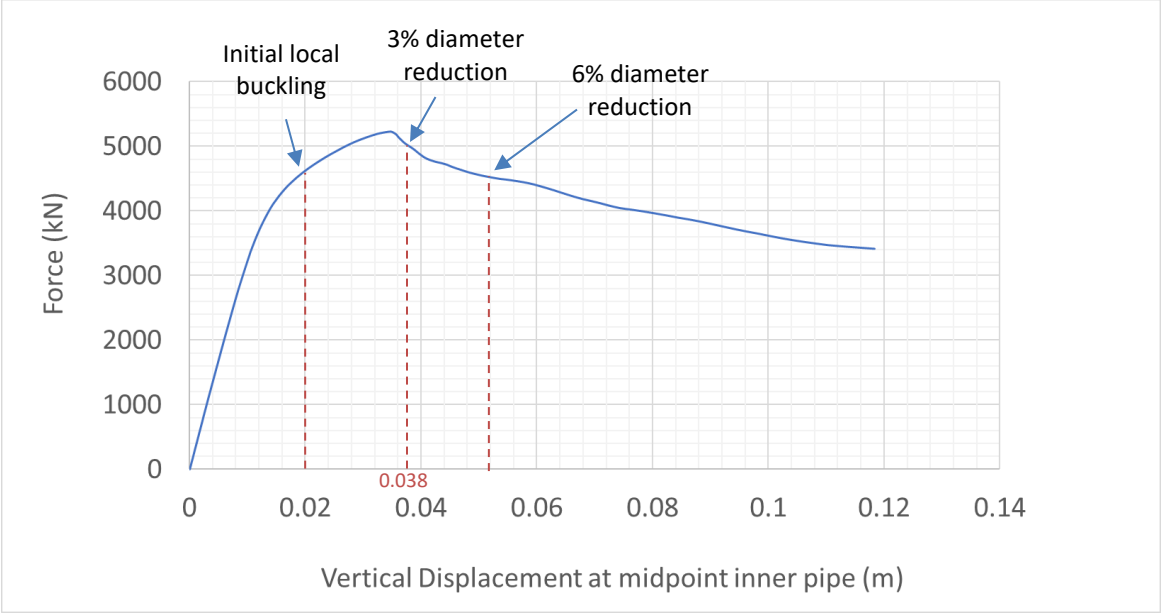

Figure 7.26 Load capacity of the unbonded imperfect composite pipe

Table 7.2 shows a summary of the analysis results, including the total hinge angle for the inner pipe.

Table 7.2 Stress, hinge angle and strain of the unbonded imperfect composite pipe

	Displacement at load point (cm)	Displacement at mid-point (cm)	Half beam length (cm)	Total hinge angle (degree)	Von Mises Stress in Steel (MPa)	Principal Strain (-)
Initial local buckling at 2cm load displacement	1.85089	2.37208	179.585	0.76	373.6	0.004252
3% diameter reduction	3.39507	4.15074	179.260	1.33	386.2	0.01372
6% diameter reduction	5.27965	11.5973	175.844	3.77	395.0	0.03819

7.4 Comparison Between Imperfect and Intact Composite Pipe

Two equal vertical displacement loads were applied on the simply supported composite beam near the mid-section. Displacements of the beam at mid-section were noted and used in Figure 7.27. The analysis results of imperfect and intact composite beams were compared in the

areas of load, stress, and hinge angle. The horizontal axis represents downward vertical displacement at the tubular composite beam mid-point.

The force applied was extracted from reactions at the two supports. Applied forces against the vertical displacement at the mid-section of the beams were plotted. From Figure 7.27, it can be seen that both imperfect and intact pipes have the same capacity. However, they have different post-peak capacities. The welded tubular beam lost capacity much more than the intact tubular composite pipe.

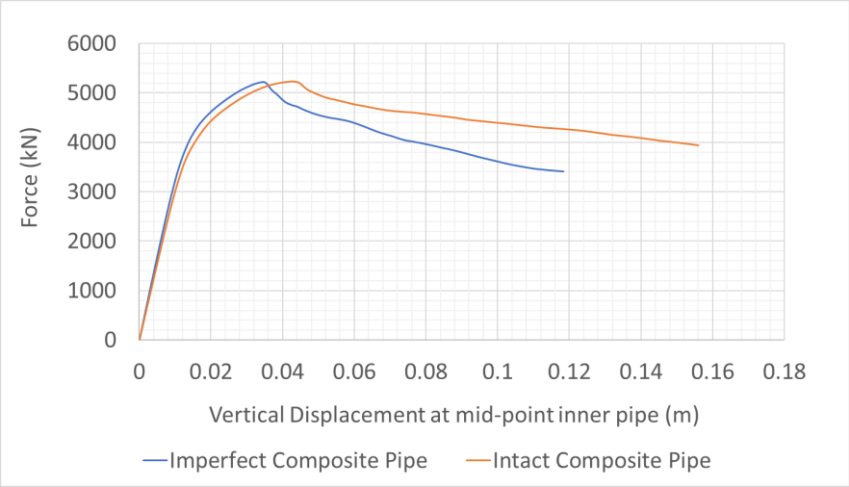

Figure 7.27 Load capacities comparison of imperfect and intact composite pipe

From the von Mises stress against beam deflection at mid-point plot in Figure 7.28, it can be observed that the intact composite beam has more capacity. It can deflect more and be able to take more stress.

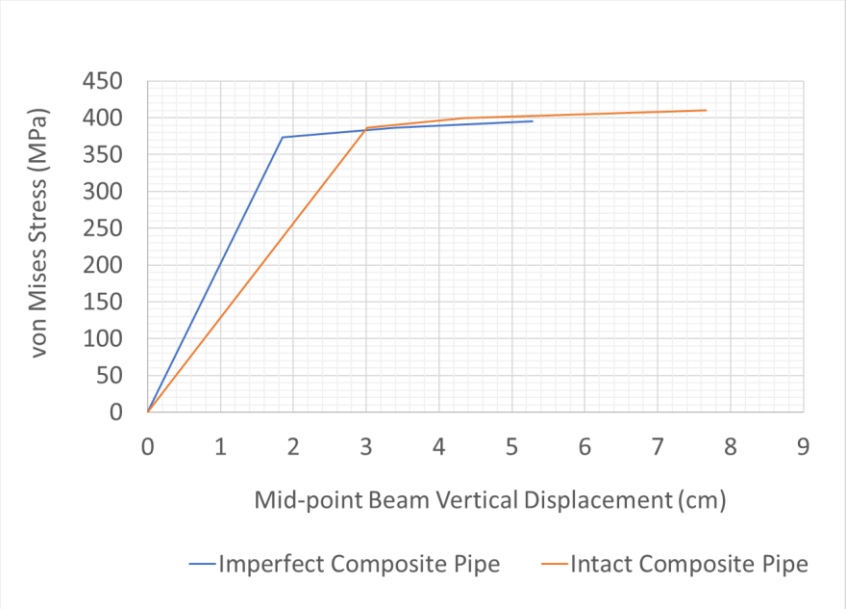

Figure 7.28 Displacements of imperfect and intact composite pipes

From hinge angle against beam deflection plot in Figure 7.29, it can be observed that the hinge angle of intact beam is much bigger because it has the ability to deflect more.

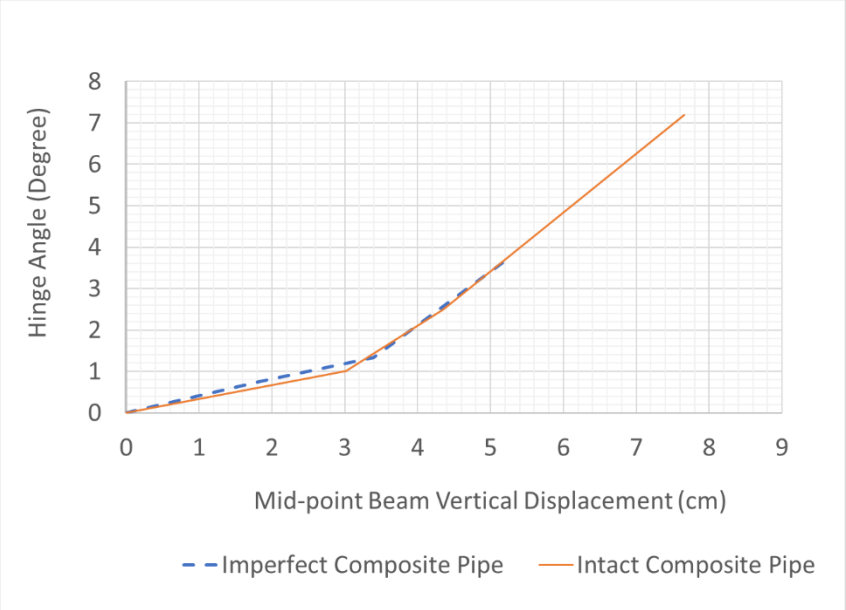

Figure 7.29 Hinge angle comparison of two unbonded composite pipe

Overall, it can be observed that the intact composite beam is much more ductile and has the ability to deflect much larger. Beyond post-peak, the load capacity of the intact beam reduces gradually. However, the load capacity of the imperfect composite pipe reduces drastically. The stress capacities in the two beams are similar to that of the load. The total hinge angle in the intact composite pipe can go much larger than that of the imperfect beam, the welded pipe. The intact composite pipe shows a much more ductile behavior than that of welded pipe. In reality, it is almost impossible to have such behavior or capacities. From the analysis result, it can be seen that the deflection capacity in the welded pipe is 30% lesser, in addition to having much lesser capacity beyond post-peak load. Thus, the intact capacity of the composite beam cannot be used in the design. It can be another study topic how much load capacity reduction is to be used when two composite pipes are connected.

7.5 Bonded Imperfect Composite Pipe

The beam length was 3.6127m long. Two vertical displacement downward loads were being applied at 1.20m from each support. Mesh size was finer, 2cm at mid-region of the beam length of the tubular beam center, and 10cm near the load points. There are 48 elements around the pipe. Mesh element types are C3D8R, an 8-node linear brick, reduced integration, hourglass control. The beam assembly and boundary conditions are shown in Figure 7.30.

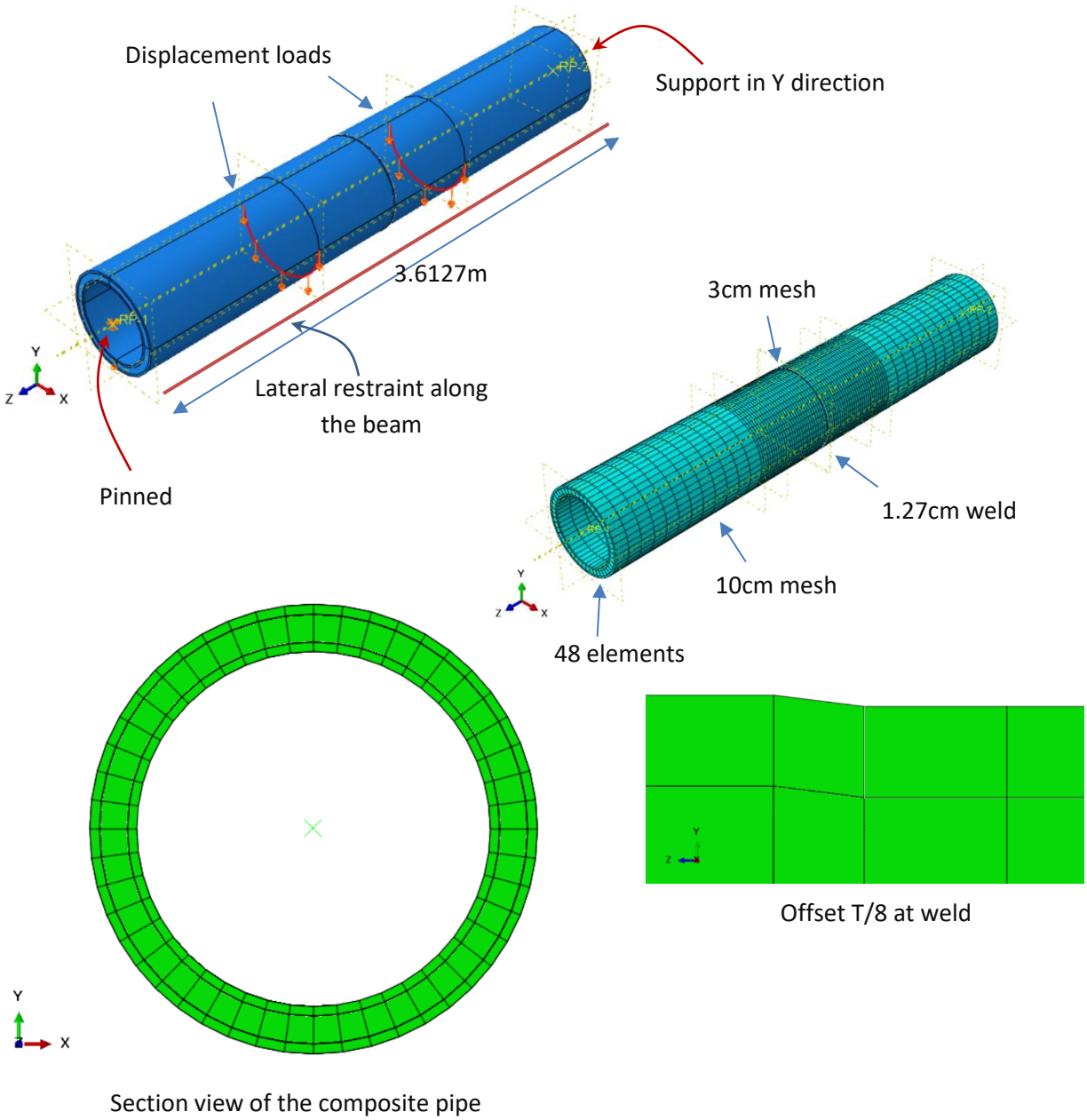

Figure 7.30 Imperfect bonded composite pipe

7.5.1 Analysis Results of the Bonded and Imperfect Composite Pipe

In the bonded imperfect composite pipe, the bond between steel and polymer is perfectly bonded, unlike the unbonded composite pipe.

7.5.1.1 Imperfect composite pipe polymer modulus of elasticity 200MPa

Figure 7.31 result shows buckled failure of the composite pipe. Steel's maximum plastic capacity is 441.3MPa. Maximum stress occurred in the polymer. However, the maximum stress in steel at this point was 428.8MPa. Stress failure results are shown below. The deflection plot at mid-point against load point displacement is plotted below at failure.

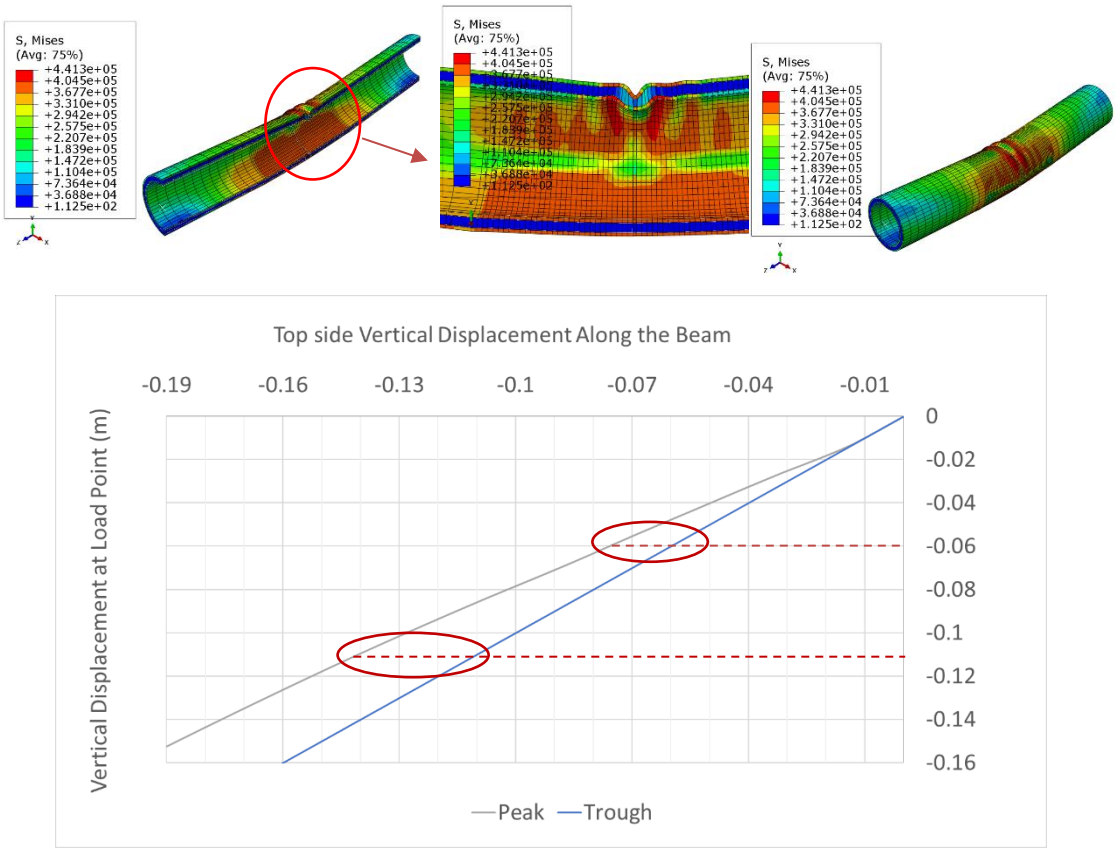

Figure 7.31 Displacement plot of the soft polymer composite pipe (Ep/Es = 0.001)

From the plot in Figure 7.31, diameter reduction at certain load displacements can be extracted. It can be observed that 3% diameter reduction occurred at 0.06m load displacement and 6% diameter reduction occurred at 0.12m load deflection. Initial local buckling was observed at a load point displacement of 0.015m. From the bottom side displacement plot at peak and trough locations shown in Figure 7.32, there was no

significant change of diameter. Hence, it can be concluded that the diameter reduction of the bottom side can be ignored.

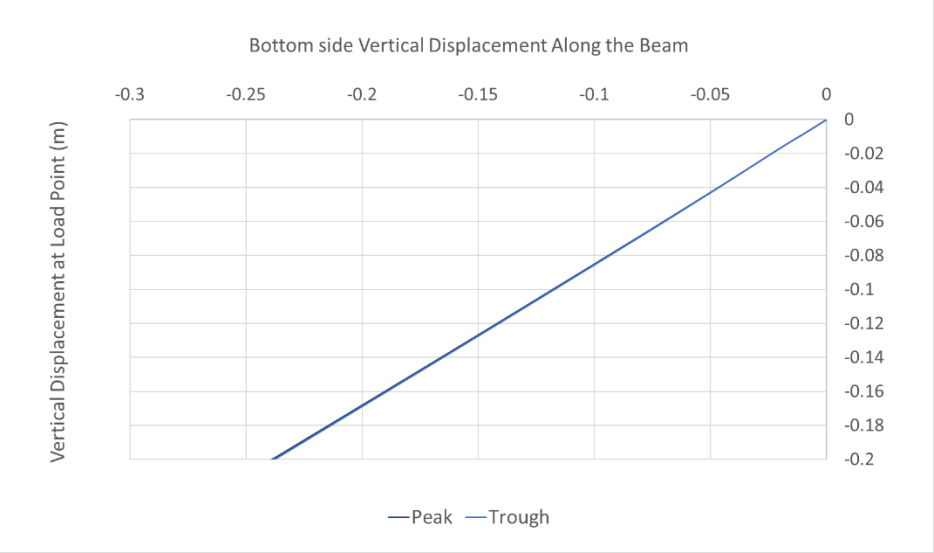

Figure 7.32 Displacement at bottom side of the inner pipe

The maximum stress at 6% diameter reduction was 441.3MPa and the strain was 0.06932. The maximum stress and strain occurred at the outer pipe. The inner pipe also experienced maximum stress capacity and the strain was 0.06627. At 3% diameter, the stress was 431.3MPa and the strain was 0.05236. At the initial local buckling, the stress was 380 MPa and the strain was 0.008433. Wrinkles were observed at the compression side of the pipe. The largest wave formed at the mid-section of the composite beam. The wave gets smaller towards the supports, and it dissipates before reaching the support. The stress and strain plots are shown in Figure 7.33 and Figure 7.34.

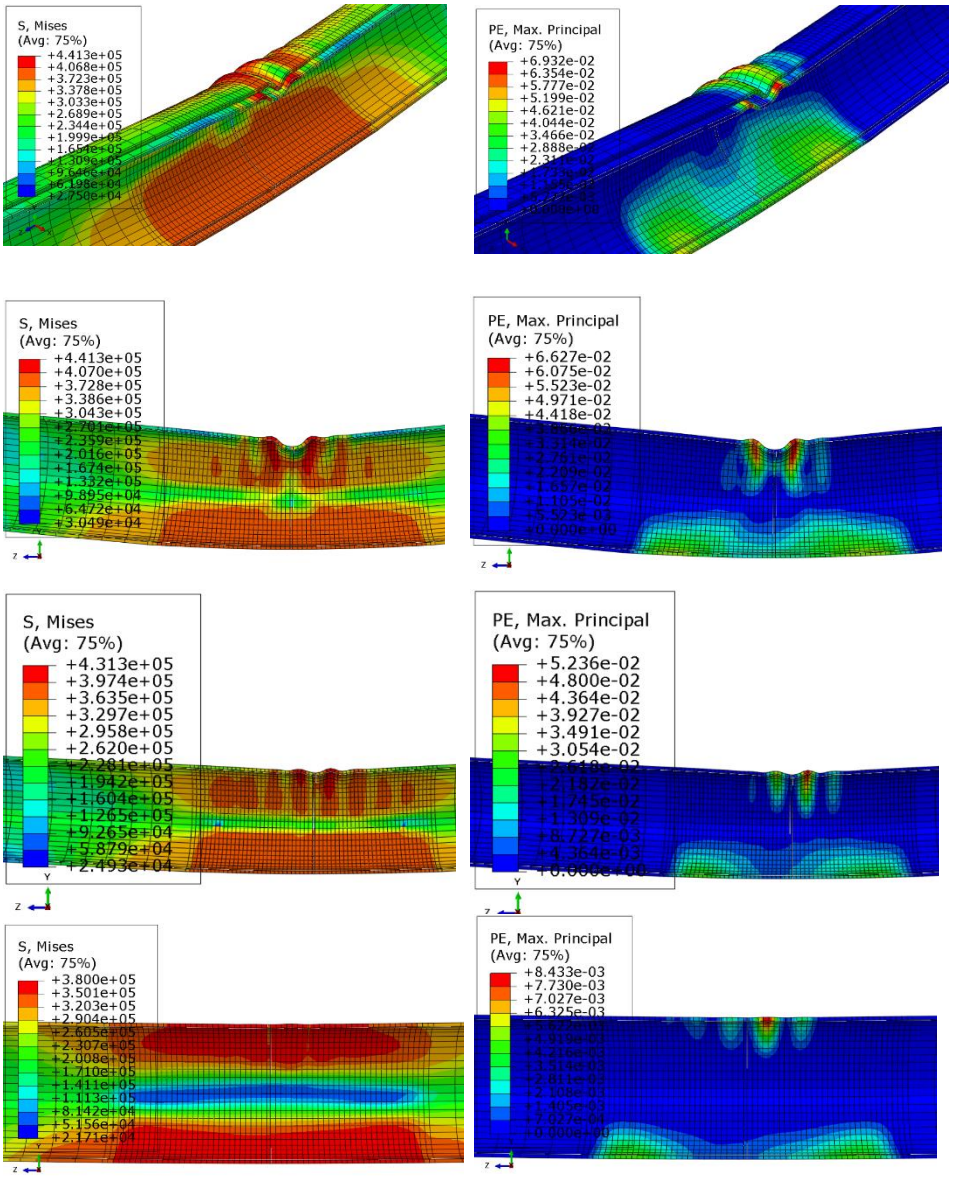

6% diameter reduction

6% diameter reduction

3% diameter reduction

Initial buckling

Figure 7.33 Stress and strain results of the composite pipe with soft polymer grout

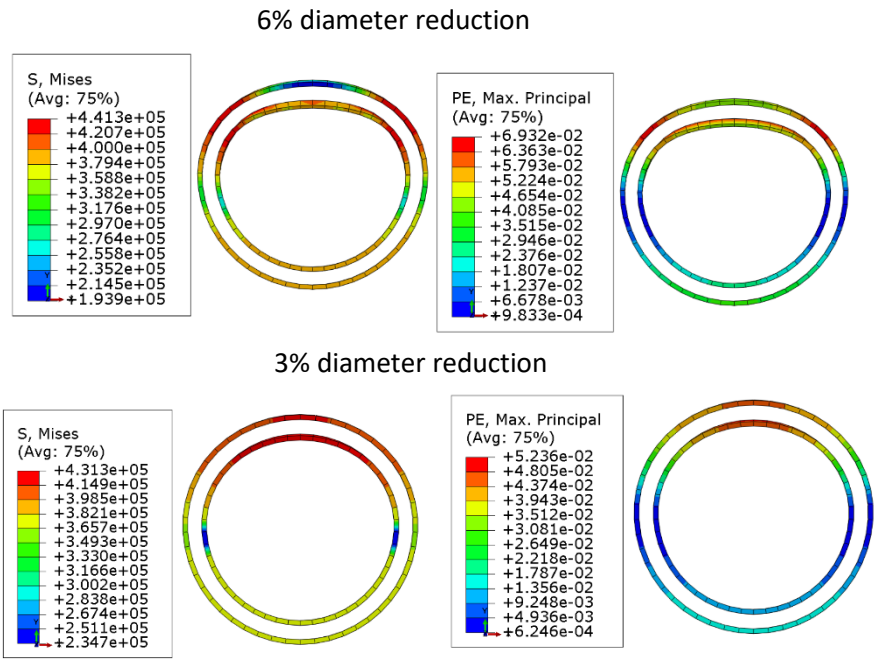

Figure 7.34 Deformation, stress and strain of the inner and outer pipes

Steel pipes of the composite section from pipe stress against load-displacement plot in Figure 7.35, it can be observed that the inner pipe stress is around 420MPa at 3% diameter reduction, and 440MPa at 6% diameter reduction. At initial local buckling, the stress was about 370MPa. These values are comparable to displacement at mid-point against load point plot.

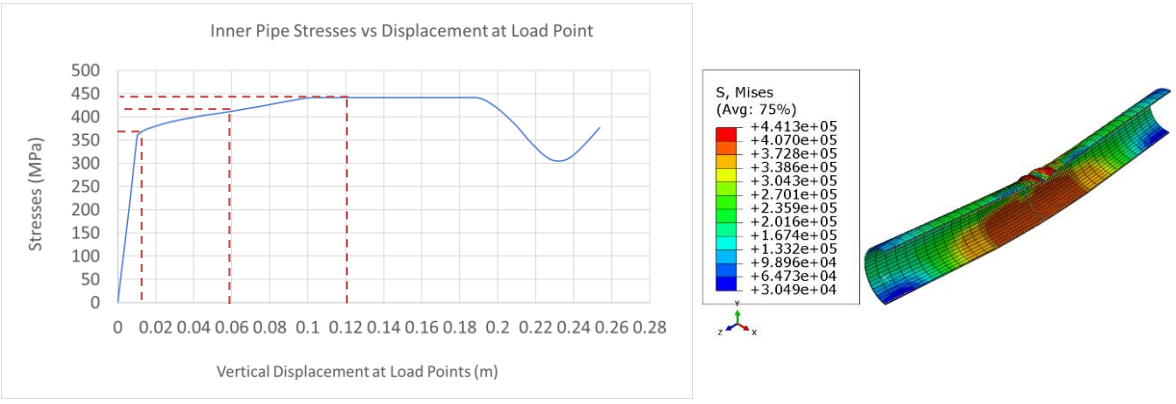

Figure 7.35 Inner pipe stress plot of the compose pipe

Figure 7.36 shows force displacement for the intact composite pipe at the mid-section. The load capacity was 4600 kN at the initial local buckling, 4700kN at 3% diameter reduction, and 4700kN at 6% diameter reduction. After the initial buckling, it can be seen that there was not much load capacity left with about a 2% increase in the load capacity. The composite pipe capacity reduces fairly rapidly after its inner pipe diameter is reduced by 6%. At this point, the inner and outer pipes' stresses are 441.3MPa, reaching the ultimate capacity of the steel. Therefore, the composite pipe's capacity reduces more rapidly once the steel has reached its ultimate stress capacity of 441.3MPa. As the beam capacity reduces due to plasticity in the composite pipe, the curve also decreases gradually as shown in Figure 7.36.

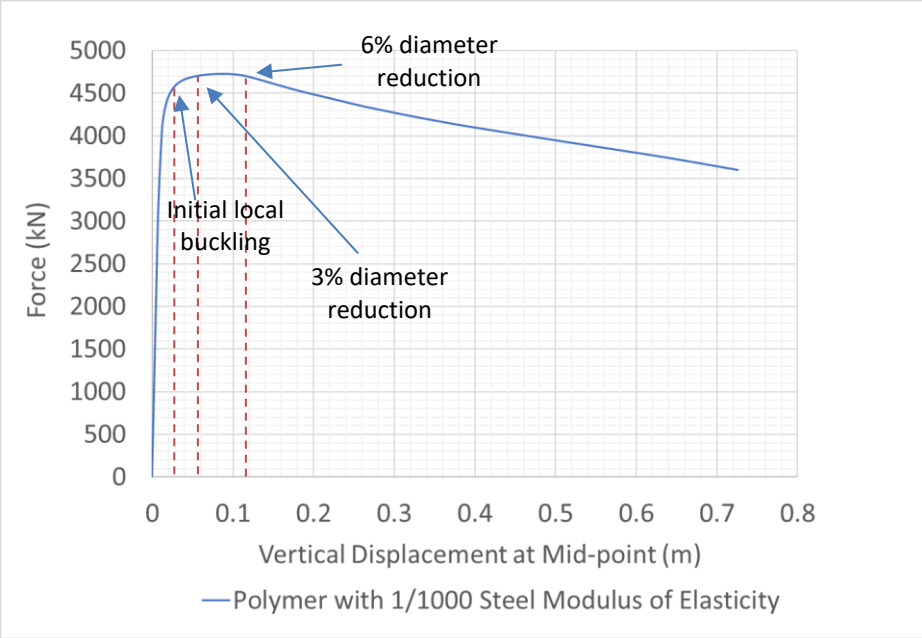

Figure 7.36 Load capacity of the composite pipe

7.5.1.2 Polymer modulus of elasticity 2,000 MPa

Figure 7.37 analysis results show 3% and 6% diameter reduction. For this polymer, the steel has already reached its ultimate capacity of 441MPa at 6% diameter reduction. At 3% diameter reduction the steel has stress 437.4MPa. Therefore, polymer with this stiffness is only good up to 3% diameter reduction and the strain at this point was 9.1%.

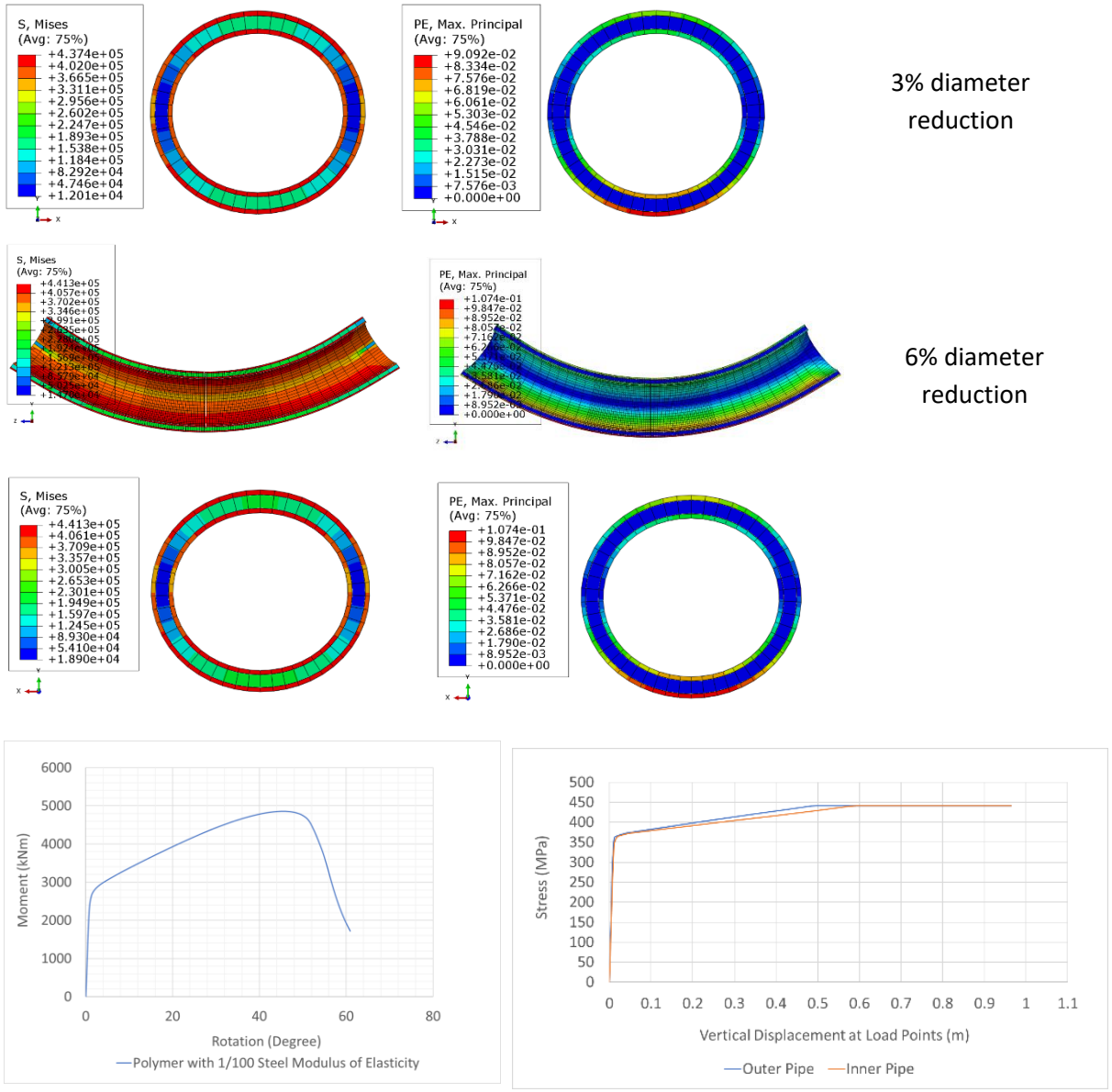

Figure 7.37 Analysis result for polymer with medium stiffness composite pipe (Ep/Es=0.01)

7.5.1.3 Polymer with Modulus of Elasticity 20,000MPa

The ratio of Polymer's modulus of elasticity to steel is 0.1. We can see from the result in Figure 7.38 that the stress was 411.9MPa at 3% diameter reduction and at 6% diameter reduction the stress was 423.8MPa. The strain was 0.0557 at 3% diameter reduction and at 6% diameter reduction the strain was 0.06588.

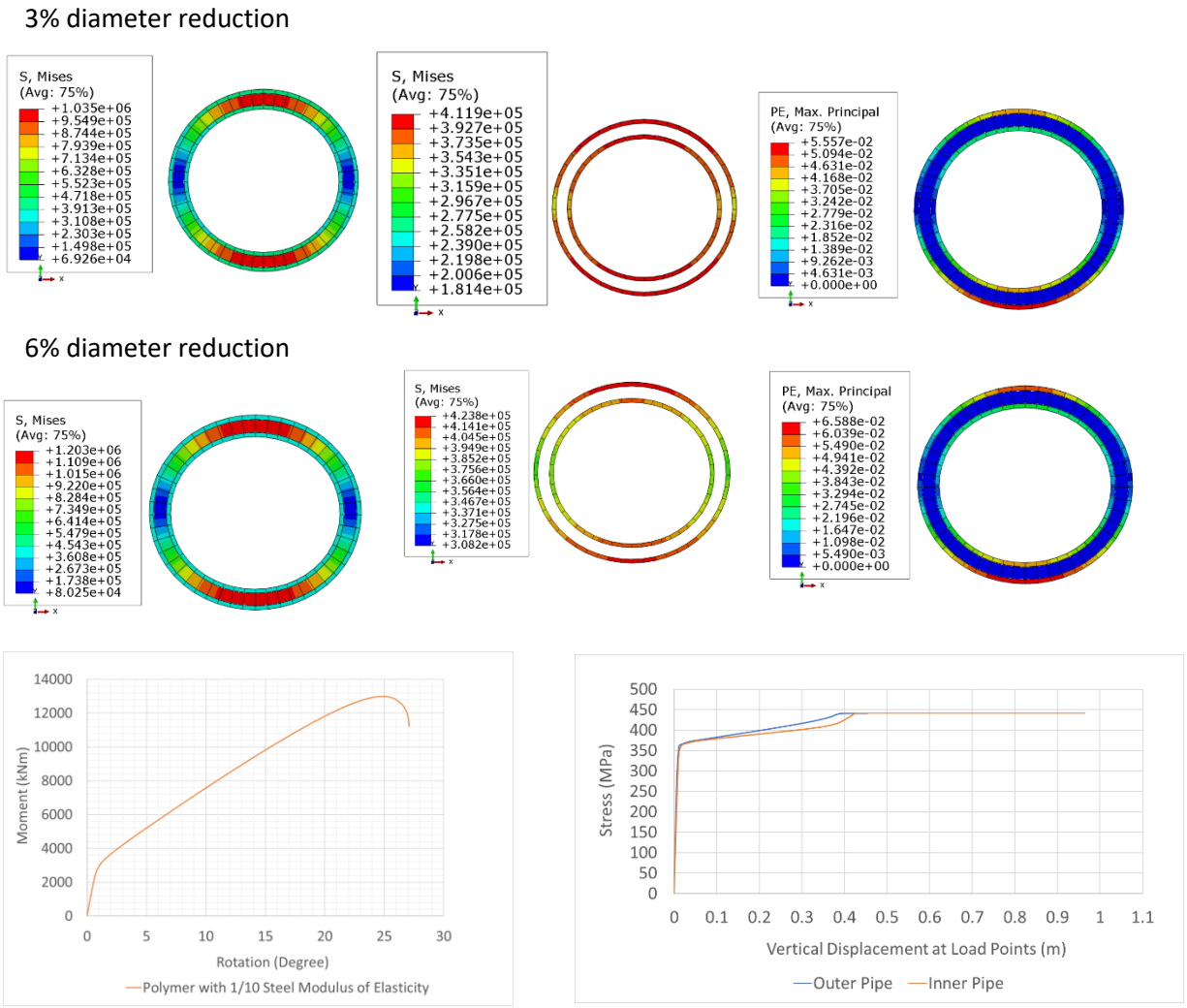

Figure 7.38 Deformation, stress and strain result of the composite pipe (Ep/Es =0.1)

7.5.1.4 Force-deflection comparison for imperfect composite pipe

The polymer stiffness grout has a significate impact on the composite pipe's overall capacity. We can see from Figure 7.39 that an increase in modulus of elasticity 10 times has the ultimate capacity increase by about 2 times. The initial buckling is about the same for all the 3 different polymer stiffness, however, capacity beyond buckling is significantly different for different polymer stiffness.

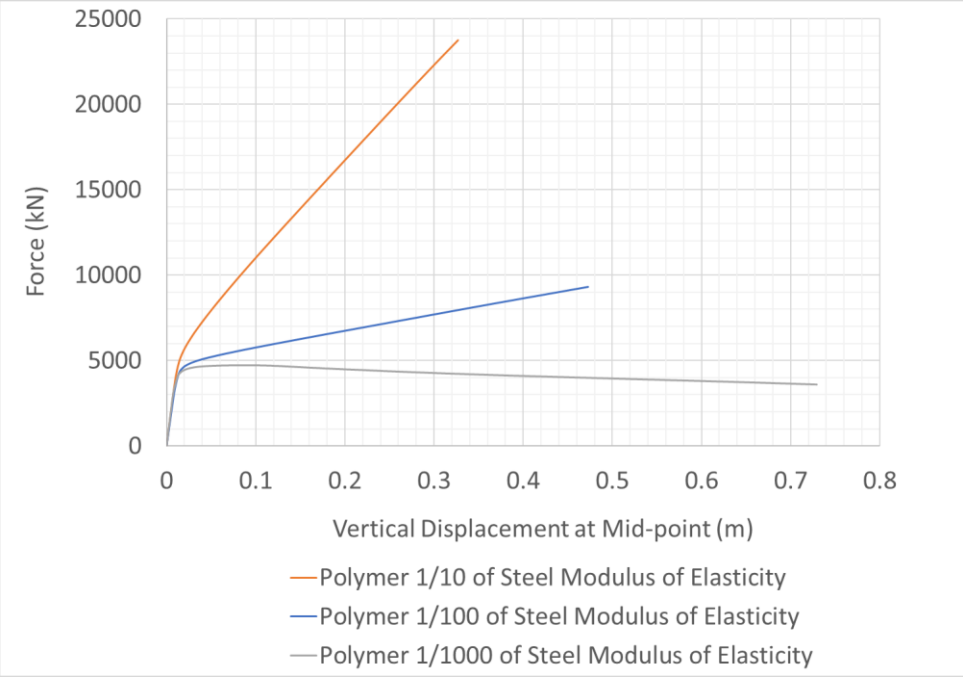

Figure 7.39 Load capacities comparison of the bonded and imperfect composite pipe

6.5.1.5 Force deflection comparison between imperfect and intact composite pipes

Imperfect and intact composite pipe analysis results are compared in Figure 7.40. The intact and imperfect pipe analysis results have negligible differences.

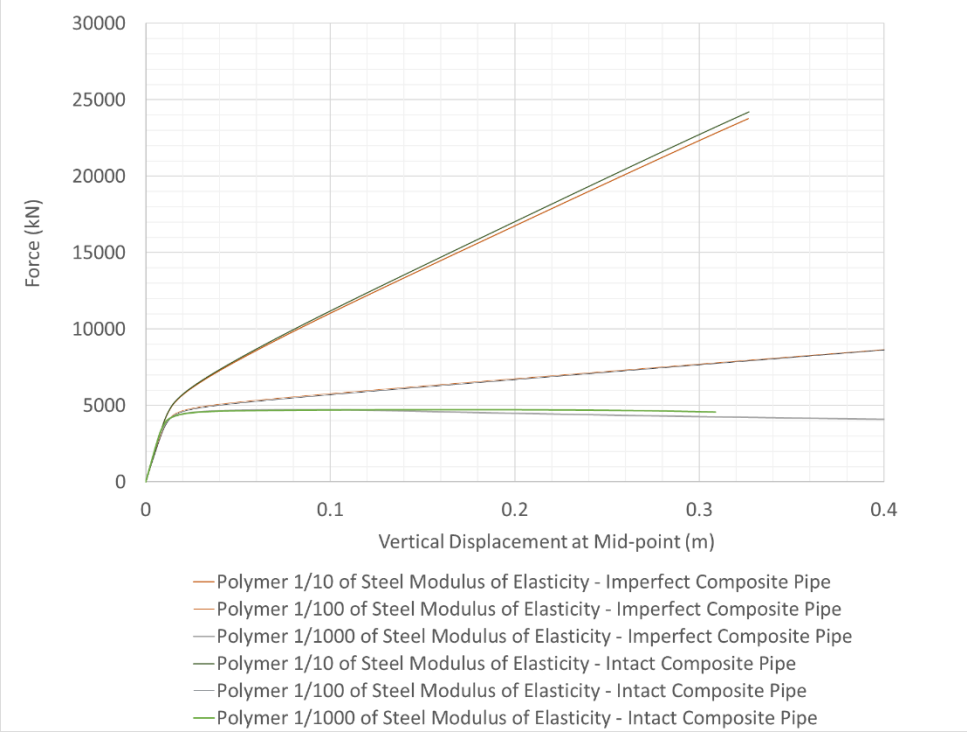

Figure 7.40 Load capacities comparison of the bonded imperfect and perfect composite pipes

7.5.1.5 Moment Capacity

Moment capacity was compared between different polymer stiffness of the composite popes. It can be observed from Figure 7.41 that 10 times different in the polymer stiffness has moment capacity over 2 times larger.

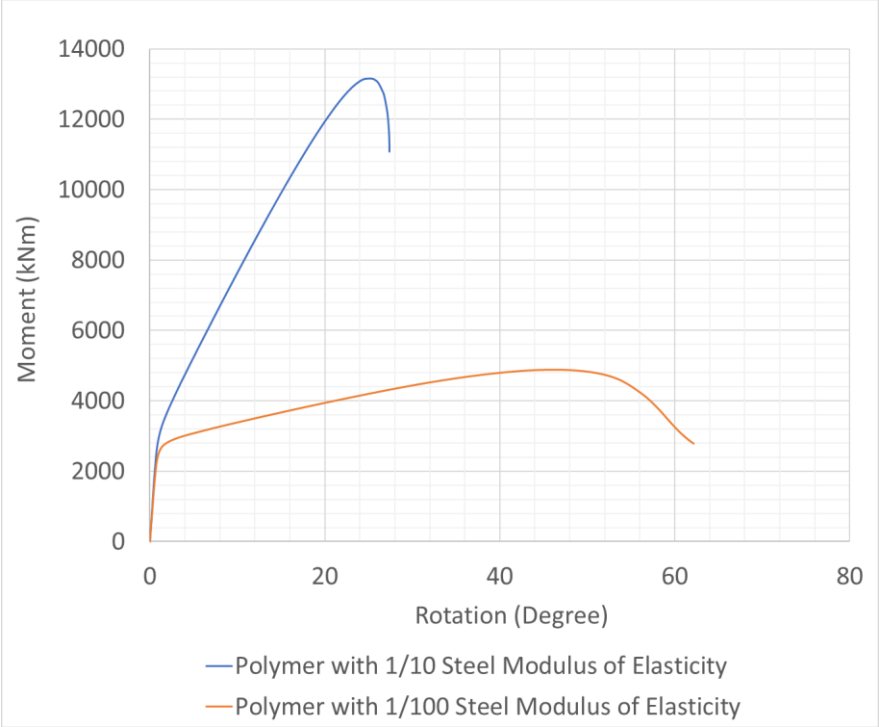

Figure 7.41 Rotation of bonded imperfect composite pipe

7.6 Composite Pipe with Different Annulus

7.6.1 Composite Pipe Annulus 2.54cm

Now the annulus between the two pipes is 2.54cm. Force – deflection plot in Figure 7.42 shows that capacity is two times different when polymer stiffness is differed by 10 times.

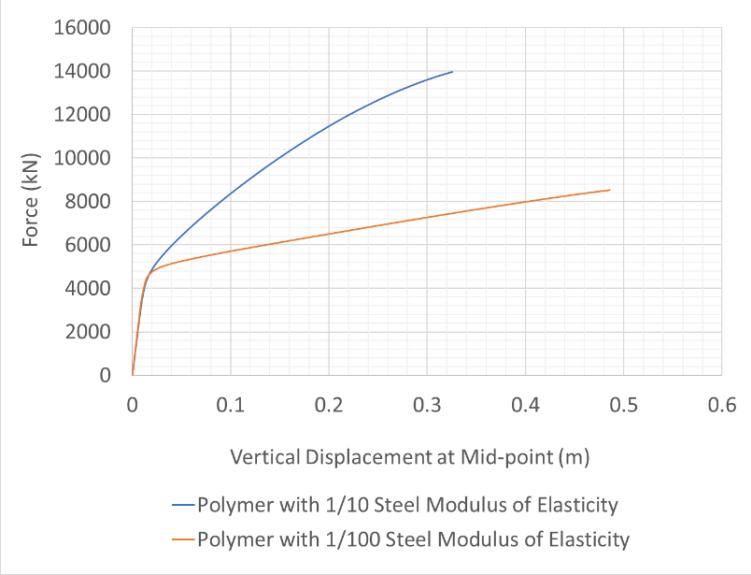

Figure 7.42 Vertical displacement of the bonded intact composite pipe with annulus one inch

7.6.2 Rotation Angle vs Moment Plot

Similar to analysis results earlier the moment capacity is over two times larger when the polymer grout stiffness is increased by 10 times. The comparison plot is shown in Figure 7.43.

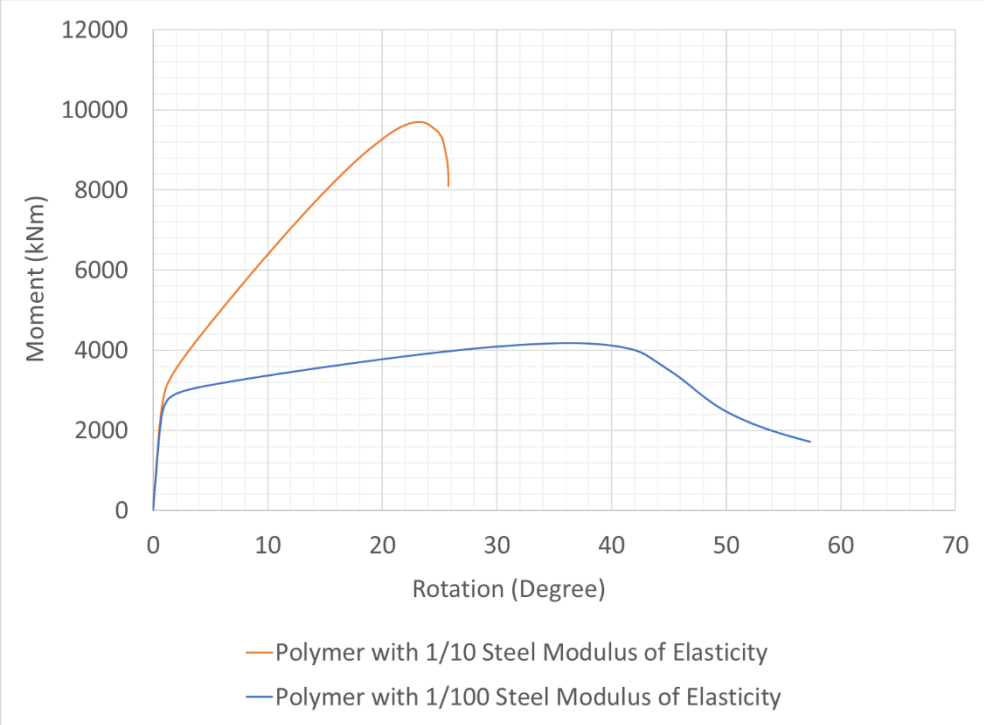

Figure 7.43 Rotation of the bonded intact composite pipe with annulus one inch

7.6.3 Composite Pipe Annulus 1.27cm

The annulus between the two steel pipes is now smaller, 1.27cm. The force and moment capacities are about two times larger when the polymer grout stiffness is increased by 10 times. However, as the annulus gets smaller it is observed that the difference between the two composite capacities is also smaller. The plots are shown in Figure 7.44 and Figure 7.45.

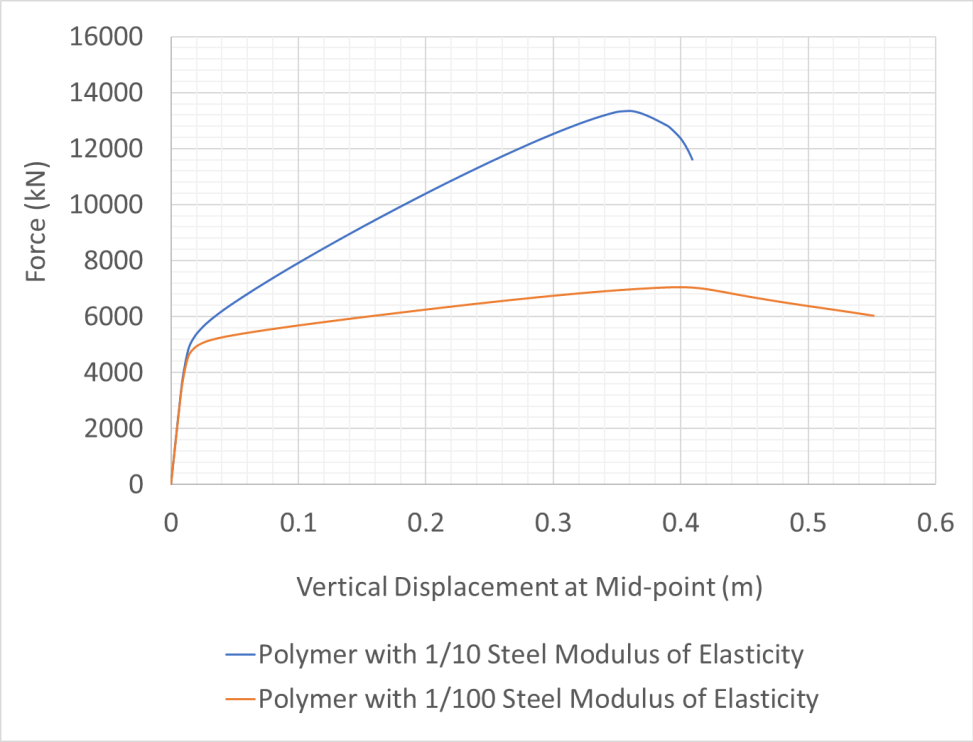

Figure 7.44 Vertical displacement of the bonded intact composite pipe with annulus half inch

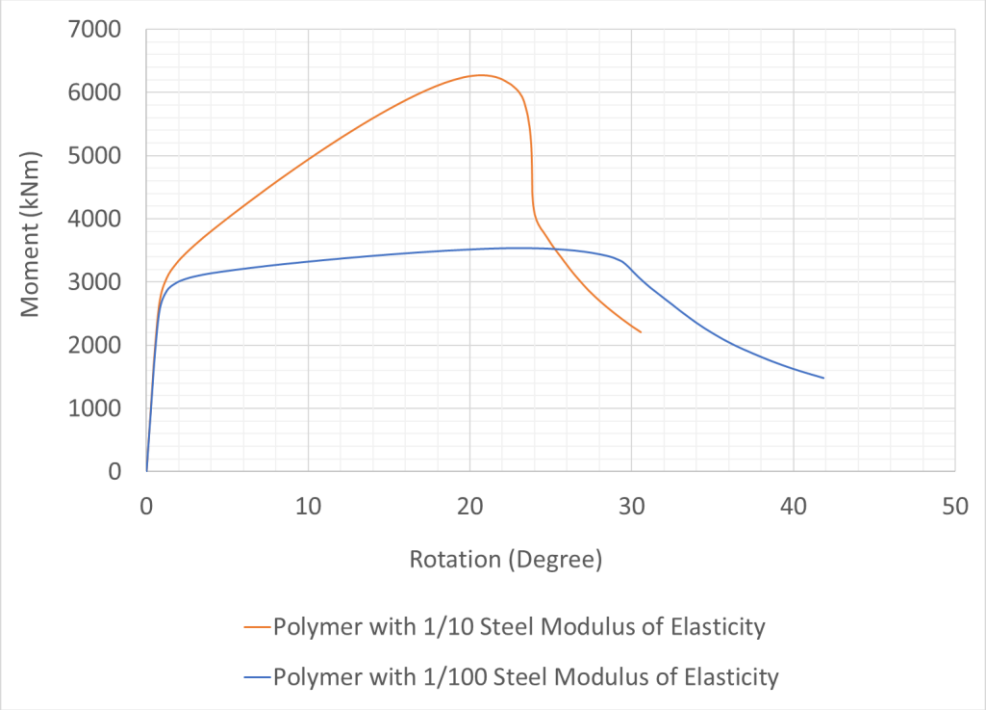

Figure 7.45 Rotation of the bonded intact composite pipe with annulus half inch

7.7 Comparison of 2 inch Thick Single and Double-wall Composite Pipe

Let us compare the 2-inch-thick single-wall pipe and the 2-inch overall thickness of the composite pipe. The beam length is 3.6127m. The single-wall pipe is 24x2 inches. The double-wall composite pipe is 24x0.5 inch and 21x0.5 inch, the annulus 1 inch thick is grouted with polymer. Rotation was applied at both ends. Single-wall pipe failed by buckling, and wrinkles were formed at mid-length. Such failure did not occur in the double-wall composite pipe. Strain at 2% was observed. Double-wall composite pipe reached 2% strain in the steel at a rotation angle of 11 degrees, however, the rotation angle of single-wall pipe was 9 degrees at this point. The single-wall pipe also experienced higher stress with 396 MPa. The double-wall composite pipe experienced slightly lower stress with 383 MPa. Although these may be acceptable, the single-wall pipe ovality was 9% and this is way over the acceptable limit of 2% to 6%. The double-wall composite pipe experienced a very small ovality of just 0.5%. Therefore, it can be

seen that the double-wall composite pipe with polymer grout significantly improves the pipe ovalization shows 24x2 inch single-wall and double-wall composite pipes bending in air analysis results comparison.

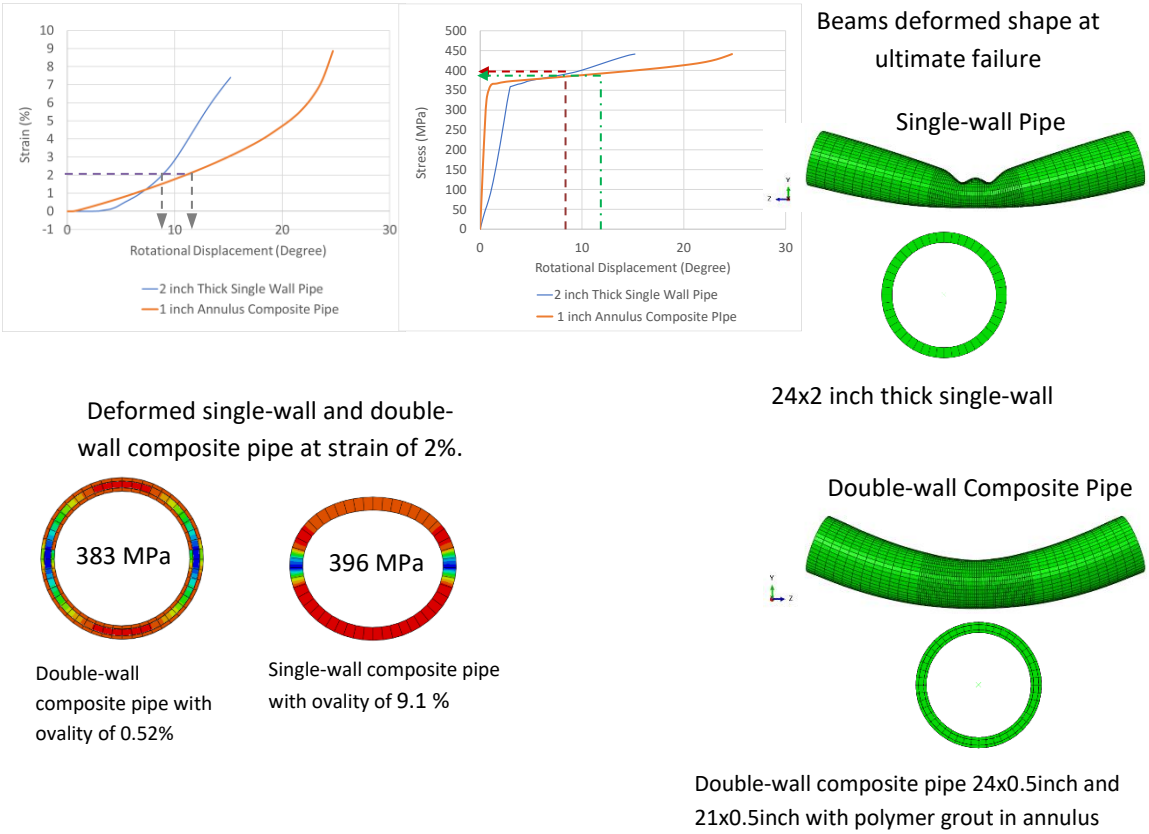

Figure 7.46 24x2 inch single-wall and double-wall composite pipes bending in air

7.8 Comparison of Welded and Un-welded Composite Pipe Analysis in Air

Simply supported imperfect double-wall composite pipe four points bending assembly is shown in Figure 7.47. The inner and outer pipes were welded using a T/8 offset. One end of the beam is pinned, and the other end is a roller. The beam is restrained against lateral displacement and is only allowed to move vertically. The vertical displacement loads were applied at 2 equidistance locations, a third and two-third of the beam length. The welded pipe represents

imperfection in the pipe. The un-welded is taken as an intact composite pipe. Four-point bending analysis was performed on both simply supported beam sections in the air.

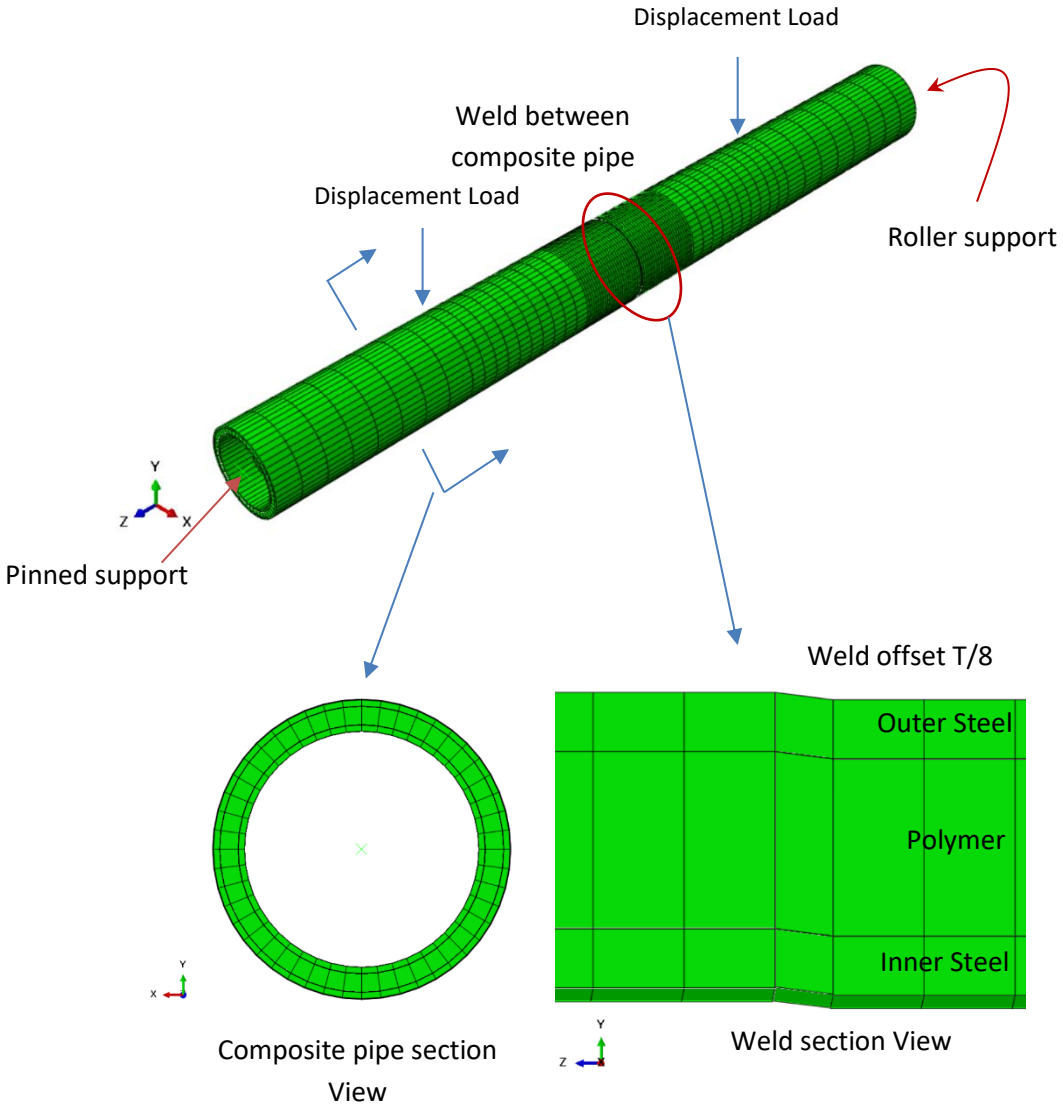

Figure 7.47 SPS four-point bending beam boundary conditions and weld section view

Figure 7.48 shows the composite pipe ovality with 3% for the imperfect and intact composite pipe. It can be seen from the results that even at 3% ovality, the strain is already high.

The intact composite pipe has a strain value of 5.42% and the imperfect composite pipe has a strain value of 6.14%. The stresses are also close to the ultimate capacity of 441 MPa.

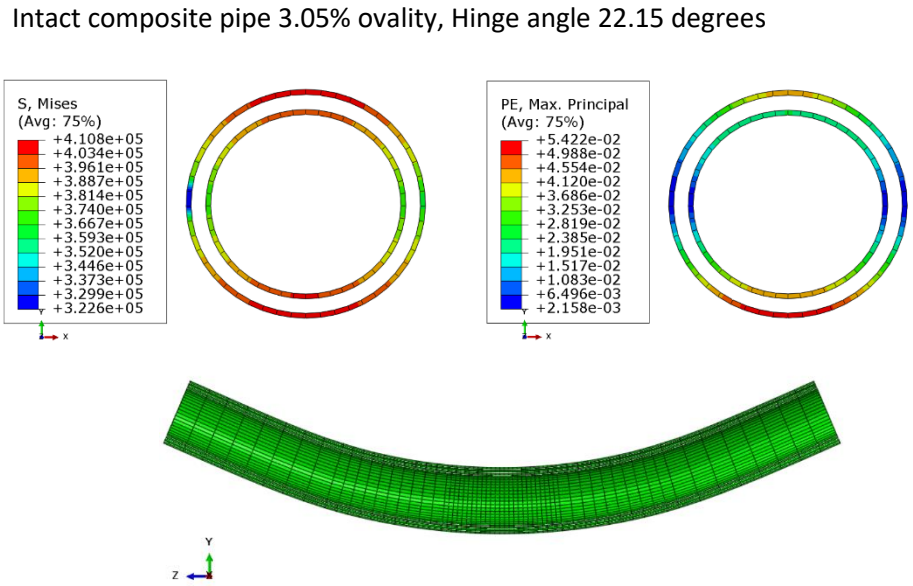

Figure 7.48. Result of 3% ovality

The analysis results for 6% ovality are shown in Figure 7.49. The strain and stresses are still high. They are not far above the 3% ovality, with a 29% increase in strain for the SPS section with imperfect weld and the stresses increase only by 4%.

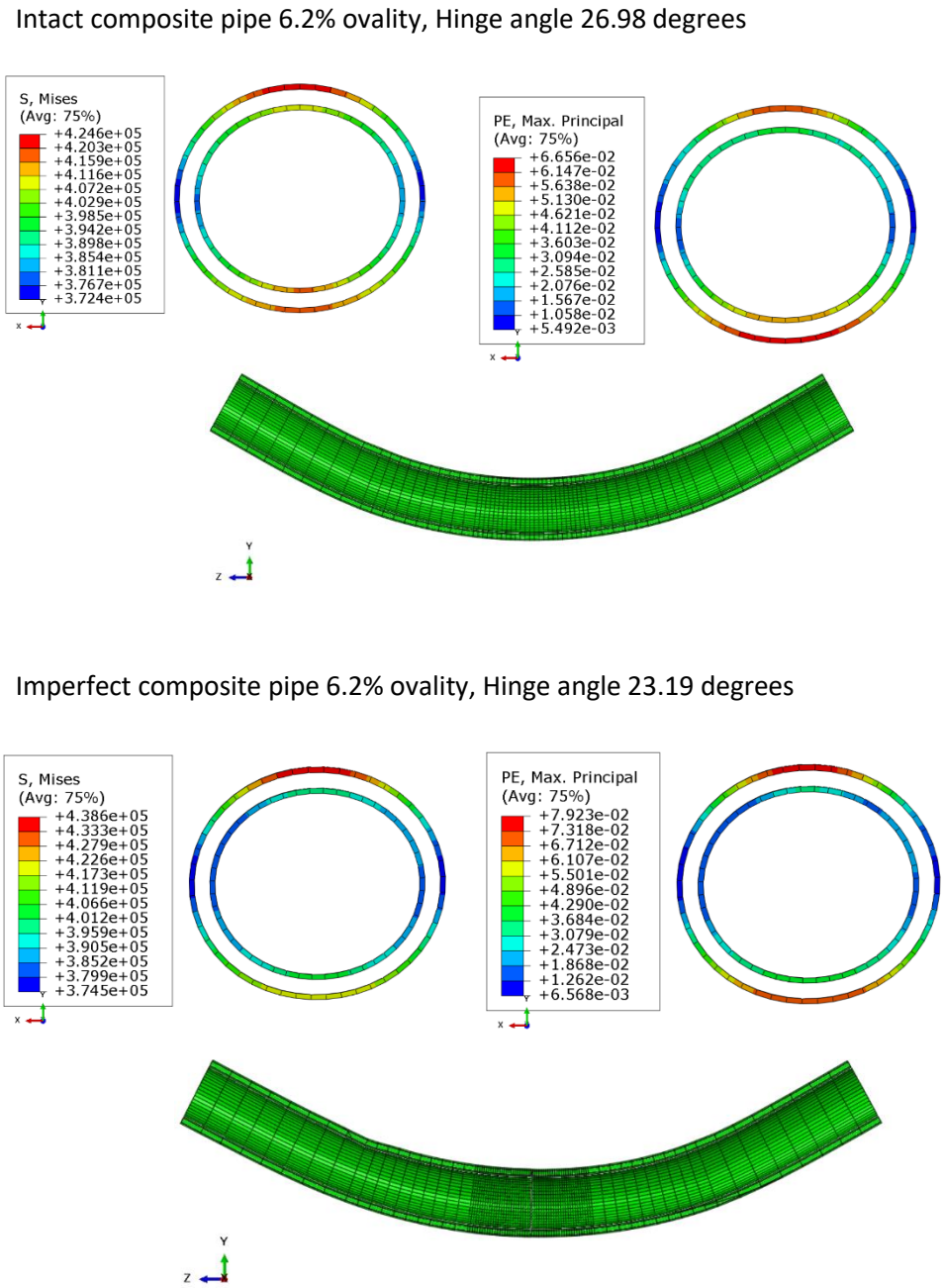

Figure 7.49. Results of 6% ovality

The strain was limited at 4% for the outer pipe and 2% for the inner pipe as shown in Figure 7.50. Ovality for the imperfect pipe was 0.74% and ovality of the inner pipe was just 0.48%. This shows that strain is the governing in SPS composite pipe. The imperfect SPS composite pipe exhibits more ductility than the intact composite pipe. The imperfect composite pipe strain for the outer and inner pipe shows a much larger difference than the intact composite pipe. The stresses are also larger than the intact composite pipe.

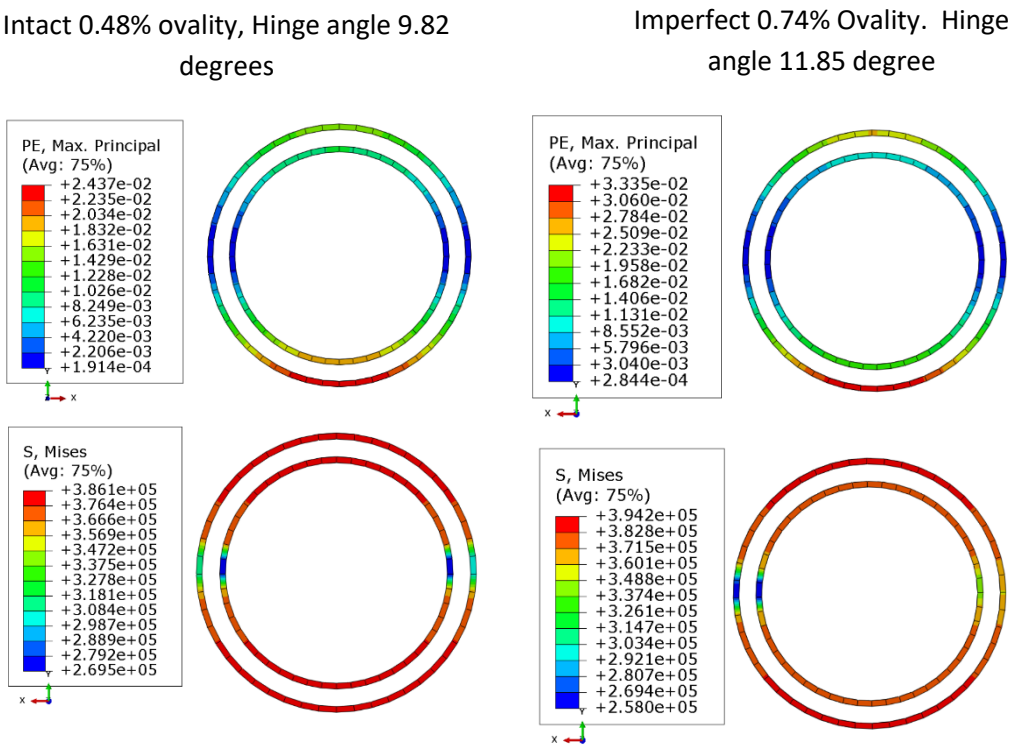

Figure 7.50. Strain limit 4% for the outer pipe and 2% for the inner pipe

The stress and strain analysis result shows welded strain is 37 percent higher than the un-welded composite pipe for the outer pipe. The stress is 2% higher in the welded pipe than the intact pipe. Taking the worst scenario from different pipe ovality it can be concluded that the strain can be 37% higher in the welded pipe and stresses can be 4% higher in the welded pipe.

7.9 Results Comparison of Intact and Welded Composite Pipe

Benchmark studies performed show that the FE analysis results match the test results. Single-wall pipe analysis result shows buckling and wrinkling in the pipe, ovality, high stress, and strain.

SPS double-wall composite pipe four-point bending in air analysis results show that the imperfect weld in the pipe has high stress and strain, and larger ovality compared to the intact composite pipe. The analysis results summary is recorded in Table 7.3.

Table 7.3 Results summary of SPS double-wall composite pipe analysis in air

Observation	Tubular	Ovality (%)	Stress (MPa)	Inner Pipe Strain (%)	Outer Pipe Strain (%)	Hinge Angle (Degree)
1	Intact	3.1	410.8	4.1	5.42	22.1
	Weld	3.1	421.3	3.7	6.13	21.8
Difference		0	2.56	9.76	13.10	1.36
2	Intact	6.2	424.6	5.2	6.7	27.0
	Weld	6.2	438.6	4.8	7.9	23.2
Difference		0	3.30	7.69	18.99	14.05
3	Intact	0.48	386.1	2.0	2.44	9.82
	Weld	0.74	394.2	2.0	3.34	11.85
Difference		54.17	2.10	0.00	36.89	20.67

When the ovality is set to 3% or 6%, the intact composite pipe has a larger angle to achieve the ovality limits and hence the inner pipe strains are larger compared to the welded pipe. The strain difference for inner and outer pipe for intact composite pipe is smaller than

welded pipe. However, when the strain limit is set to 2% for the inner pipe, the welded composite pipe rotates larger than the intact composite to achieve 2% strain, and also the outer welded pipe strain is significantly larger. Based upon the observation from 3 different types in Table 7.4 for a single-wall four-point bending analysis in air, the critical values for ovality, stress, and strain are extracted for the welded pipe. So, when the intact composite pipe is used, the amplification factor given by the welded pipe should be applied to offset the imperfection in the pipe.

Table 7.4 Amplification factor for intact composite pipe

Type	Ovality	Stress	Strain
Amplification Factor for Intact Composite Pipe	1.54	1.04	1.37

It was also found that wrinkles appear in the compression side of the SPS composite pipe when there is no bond between the steel-polymer-steel. The steel pipes experience high strain even with small deformation. The stress and strain in the inner pipe are larger than the inner pipe similar to the bonded composite pipe.

CHAPTER 8 FINDINGS AND CONCLUSIONS

There were several analyses performed over the entire research. In general, they are:

1. Portal beam single-wall pipe with axial and lateral loads
2. Single-wall pipe in clay
3. Double-wall composite pipe in clay
4. Pipe analysis on different clay stiffnesses
5. Deepwater flow line calculation and analysis
6. Single-wall pipe 4 point loads analysis and bending
7. Unbonded double-wall composite pipe analysis
8. Bonded double-wall composite pipe analysis
9. Load Capacity and Behavior of Composite Pipes with Different Annulus Thickness
10. Double-wall Composite Pipe and Single-wall Pipe Comparison
11. Intact and Welded Composite Pipe Analysis in Air Results Comparison.

8.1 Portal Beam Single-wall Pipe with Axial and Lateral Loads.

PA, PB, PC, and PC series of the portal beam single-wall pipe were tested to validate the experimental results in 1980.

PA-1, PA-2, PA3, PA-4, and PA5 finite element analysis results were a relatively good match with the experimental analysis results. Buckled failures at the base fixity were also the same for test and FE. A Mesh size study was also performed. The mesh size used in the test was TxT. When the mesh was refined 1.8 times, the results did not change significantly. The peak capacities for two different mesh sizes were still very close. Detailed analyses were documented in Chapter 4.

Similarly, PB, PC, and PD series pipes were tested. FE results were relatively close to the experimental results. Buckling and failure mode at the fixity was also the same for FE and test. From the test, it was observed that the beam capacity reduces slowly as the latest load increases in the absence of axial load. However, the load capacity of the portal pipe reduces as the axial load increases in the presence of lateral load. The mechanism here is that the curve goes up to the peak as the applied load increases. As the beam goes into plastic and as it loses its capacity the curve gradually comes down and the analysis could no longer continue as there is no more capacity in the beam.

8.2 Single-wall Pipe in Clay

Two single-wall pipes 50.8∅x1.27cm and 50.8∅x2.54cm were tested in medium clay stiffness with lateral loads at the top of the pipe. Ovalization of the pipes was observed especially for 3% and 6%. It was observed that at twice lateral displacement, 3% pipe ovalization became 6%. However, von Mises stresses in the pipe were still relatively small with 231 MPa at 3% ovalization and 335Mpa at 6% ovalization for the 50cm pipe with 1.27cm wall thickness. For the thicker pipe with 2.54cm thick, at 3% pipe ovalization the von Mises in the pipe was still low with about 293 Mpa, and at 6% ovalization the stress was 366 Mpa which is slightly over the elastic limit. So, it can be observed that stress capacity was not an issue for the single-wall pipe for the seafloor pipeline. It was rather an ovalization in the pipe that was governing the pipe load capacity.

When the single-wall pipes were loaded until they failed or buckled, the half-inch thick pipe has von Mises stress of 389Mpa and the one-inch thick pipe has 407Mpa. So, they have not reached the steel ultimate capacity of 441Mpa. However, the steel pipes were failed by buckling.

8.3 Double-wall Composite Pipe in Clay

The lateral load-displacement was applied up to 3.43m or 11.25ft. The ovalization of the inner pipe was 0.25% as per API RP 1111 ovality calculation formula and the maximum von Mises stresses of the pipe was 370Mpa. The steel's elastic yield strength was 350 Mpa, so the steel was in the early plastic region, considering its ultimate strength of 441 Mpa. However, there was no ovalization, unlike the single-wall pipe. When it was compared against Marshall's (2004) calculation results, it was found that the displacement with FE results was 11.25ft much more than that of 7.8ft by Marshall.

8.4 Pipe in Clay Analysis and Benchmark Test

Matlock (1970) tested a laterally loaded pile in clay. The experimental result was used as a benchmark for FE analysis using the cap plasticity model. The stress-strain curve of the test was entered in the FE model. The FE analysis results were compared against the experimental results. The FE cap plasticity model analysis results and the experimental results were found to be closely matching. Marshall's (2004) plastic model for soft clay results was slightly off from the experimental result because the plastic strain used in the designed calculations was small and the strain used for the experiment in soft clay was large.

Finer mesh and coarser mesh analysis results were also found the be the same. The coarser mesh has 12 elements in the pipe section and the finer mesh has 16 elements. Along the pipe, the coarser mesh size was 20cm and the finer mesh size was 10cm. No significant results differences were found.

8.5 Pipe analysis on Different Clay Stiffnesses

It can be seen from the analysis results that the load required reduces as the stiffness of the clay reduces. Stiff clay, medium clay, and very soft clay were used in the analysis. The

largest displacement load was required when the stiff clay compressive strength of 4000 psf was used. Even at 1.5m half pipe offset or 3m full pipeline offset, the pipe stress was 380 Mpa. Although the pipe is experiencing plasticity, the plastic ultimate strength is 441 Mpa and hence the pipe capacity has not been fully utilized. At this point, the ovality of the pipe was 1% and this is still much smaller than the API limit of 2%. The strain was also still relatively small with 1.68%, less than 2% limit of ASCE's requirement.

8.6 Single-wall Pipe 4-point Loading and Bending Analysis

The simply supported 4 points loads tubular beam was tested capacity. At 6% diameter reduction, the hinge angle was 2 degrees. The stresses and strain were 395Mpa and 2.98% respectively. At 3% diameter reduction, the stress and strain were 362Mpa and 0.008%. Marshall (2004) single-wall pipe embedded in 1200 psf clay has strain 1.25% and hinge angle of 2.5 degrees. Therefore, this is closer to FE analysis with a 6% diameter reduction. The strain with FE analysis is higher because it could be due to the weld imperfection inclusion. However, the results are relatively close. The ovality is 2.5% and this is slightly larger than API's 2% but less than DNV's 3%.

8.7 Unbonded Double-wall Composite Pipe Analysis

For unbonded and intact double-wall composite pipe, at 3% diameter reduction the stress was 399.5 Mpa and the strain was about 1.38%. At 6% diameter reduction, the stress was 421 Mpa and the inner pipe strain was 3.05%. This shows that unbonded perfect composite pipe experiences high stresses even at a 3% diameter reduction. However, the stresses only increased by 5% to accommodate load which causes a 6% diameter reduction. Wrinkles were observed at the compression side of the pipe.

For unbonded and imperfect composite pipe, buckled failures were similar to that of intact pipe. At 3% diameter reduction, the stress was 386Mpa and strain was 1.42%. At 6% diameter reduction, the stress was 395Mpa and the strain was 3.82%.

Thus, it was observed that when welded is added in the analysis, the strain slightly increases. However, the intact composite pipe stresses are slightly higher. Nevertheless, the difference in stresses between imperfect and perfect did not have a significant difference with about just 7%.

Looking at the load capacities, it can be observed from the force-deflection plot that the peak load is the same. However, the capacity with imperfect welded reduced much faster than the intact composite pipe. The imperfect composite pipe reaches the plastic much faster than the intact tact. At about 1.8cm vertical displacement at midpoint imperfect composite pipe started experiencing plasticity whereas the intact composite pipe required 2.7cm vertical displacement to achieve that level. Hinge angles are similar in both intact and imperfect composite pipes.

8.8 Bonded Double-wall Composite Pipe Analysis

Three polymer stiffnesses were analyzed, namely 200 Mpa, 2,000Mpa, and 20,000Mpa. Wrinkles were found when the polymer grout has soft stiffness, which is Ep/Es of 0.001. In other words, the polymer's stiffness or Young's modulus is 1000 times less than that of steel. However, there was no wrinkle found when Ep/Es are 0.01 and 0.1.

For soft polymer with 200 Mpa, the steel had already utilized its ultimate yield strength of 441 Mpa at 6% diameter reduction and the strain was high which is 6.93% and that is beyond the acceptable limit of 2% or 3%. Even at 3% diameter reduction, the steel's stress was still high with 431Mpa and the strain was 5.24%.

For medium stiffness polymer with 2,000Mpa, the stress still failed with 441Mpa utilization, and the strain was 10.74 at 6%diameter reduction. The stress was 437.4Mpa and the strain was 9.09% at a 3% diameter reduction.

Stiff polymer with 20,000Mpa gave the best results with stress in the steel 412Mpa and strain 5.55% for 3% diameter reduction and stress in the steel of 424Mpa and strain in the steel with 6.59% Mpa for 6% diameter reduction. High stresses in the polymer were observed.

Load capacities comparison of the three polymer's stiffnesses shows different behavior of the load capacities beyond post-buckling. When Ep/Es=0.001, there is no capacity left post peak load. When Ep/Es=0.01, the load capacity beyond post-peak shows the composite pipe could take almost two times the buckling load. However, when Ep/Es=0.1, there was significant load capacity still left beyond the buckling load, still having a capacity of easily 4 times the buckling load.

When imperfect and intact composite force-deflection capacities were compared, there were no significant between the welded and non-welded pipe. Moment capacity plots for stiff and medium-stiff of the composite pipe were compared. It was found from the plot that Ep/Es of 0.1 has 3 times more moment capacity than that of 0.01.

8.9 Load Capacity and Behavior of Composite Pipes with Different Annulus Thickness

Force and moments capacities were investigated for different annulus, 2.54cm and 1.27cm in the earlier Section. For the annulus of 2.54cm, the stiffener polymer always has higher load and moment capacities than the softer polymer. Similarly, for the annulus of 1.27cm, the stiffer polymer Ep/Es of 0.1 has a much higher force and moment capacities than that of 0.01.

8.10 Double-wall Composite Pipe and Single-wall Pipe Comparison

From the analysis results of 2 inches overall thick pipe for the double-wall composite and single-wall pipe, it can be seen that at the strain of 2%, the ovality of double-wall composite pipe is still very small with just 0.52% whereas the ovality of the single-wall pipe is over 9%. The rotation to achieve 2% strain is larger for the double-wall composite section. Although the composite section reached its elastic stress limit earlier than the single-wall pipe, the stress increases much slower beyond the elastic limit. The composite section has a higher capacity for strain and especially it has high resistance to ovality. It could be seen from the analysis results that the double-wall composite section brings all aspects of benefits in terms of material properties.

8.11 Intact and Welded Composite Pipe Analysis in Air Results Comparison.

Imperfect double-wall composite section exhibits higher stress and strain than the intact composite pipe. The imperfect composite pipe also has a lesser ability to the angle of rotation. When the ovality of the composite pipe was limited at 3% and 6%. At 3% ovality, the strain in the imperfect composite pipe was 13% higher. At 6% ovality, the strain in the imperfect composite pipe was 19% higher. Based upon the T/8 offset weld, amplifications should be applied to the intact composite pipe such that the ovality should be amplified by 1.54, the strain should be amplified by 1.37, and the stress should be amplified by 1.04 to account for the weld connection in the pipe.

8.12 Conclusions

1. Portal Single-wall Pipe with Axial and Lateral Loads.

Portal tubular beam experimental results performed by Sherman (1980) static loadings were verified and validated using the FE analysis. However, some inconsistencies in results were observed. For example, PA-5 experimental failure was slightly different from PA1, PA2, and PA-4. Test results in Figure 4.4, PA-5 test result shows that the load capacity dropped to 1 kip at lateral displacement 0.7in and then the load picked up again up to 2.8kip. This type of behavior was not found in the same test series. Similarly, PC-5 shows inconsistencies in test results compared to the other PC test series. The FE analysis shows consistencies and expected results, unlike some inconsistencies test results. Hence, in this aspect, the FE analysis results are consistent, accurate, and reliable.

The original mesh size was TxT and when the mesh was 2 times finer, the test result change was negligible. TxT mesh size in the FE analysis result was very close to the actual test result. Hence, having too fine a mesh for this test does not only bring more benefits but it may result in losing computation time and may cost productivity.

2. Single-wall Pipe in Clay

In a single-wall pipe in clay, it was found that the governing factor is the ovalization of the pipe. For half-inch thick pipe with a 20inch diameter, at 6% ovality, the stress was still in the elastic range with 335MPa, less than 350MPa. In one inch thick pipe, the stress at 6% ovality was 366MPa, still much less than the ultimate plastic capacity of 441 MPa. The strain limits are still low at 0.2%, however, the ovality has reached 6%.

3. Double-wall Composite Pipe in Clay

Ovality is not an issue with double-wall composite pipe, unlike the single-wall steel pipe. In addition, the steel stresses are in just early plasticity for ovality of 1.9% of the inner pipe diameter with the stress of 379MPa and the strain of 1.43%. This is still within the allowable strain limit of 2% of API RP 1111 and the ASCE.

4. Pipe in Clay Analysis and Benchmark Test

Cap plasticity model method of finite element analysis results closely matched with Matlock's (1970) test results. Marshall's (2004) plastic model for soft clay was found to be slightly off beyond 40% of the total lateral displacement and this was probably due to using very small plastic strain in the model. Using two times coarser mesh along the pipe and 25% coarser mesh around the circumference did not change the analysis results.

5. Pipe analysis on different clay stiffnesses

In soft clay, the stresses in the pipe are much smaller than the stresses in stiffer clay.

6. Single-wall Pipe with Four Point Loads Analysis

At 6% diameter reduction, the hinge angle was 2 degrees for 20x0.5 inches pipe with weld. The stress in the pipe was already high with 395MPa and the strain was 2.98%. These exceed the limit of API RP2A 1111 and ASCE requirements. At 3% diameter reduction, the stress was in early plastic with 362 MPa and has a small strain of 0.008%. Marshall's (2004) plastic model calculation result was close to a 6% diameter reduction in the FE analysis.

7. Unbonded Double-wall Composite Pipe Analysis in Air

When there was no bond between steel and the composite, stresses are found to be high. Even at 3% diameter reduction, the stress was already reaching 400MPa and the strain was

1.38%. At 6% diameter reduction, the beam carried only 5% more loads. This caused the strain to go up to 3% with a stress of 421MPa. Due to wrinkles, high stresses, and strain in the steel pipes, unbonded double-wall composite pipes are not suitable for offshore pipelines. A significant difference was not found between the pipes with the imperfect and intact composite pipes.

8. Bonded Double-wall Composite Pipe Analysis

The ratio of polymer stiffness (Ep) to that of Steel (Es) has a significant effect on the failure behavior of the composite pipe and capacities. For example, wrinkles are found in the composite pipe when Ep/Es is 0.001. However, wrinkles are not present when the stiffer polymer is used such as Ep/Es of over 0.01 in this research. Ep/Es of 0.1 is found to be working well for the composite pipe. In addition, larger stress and strain are found when the core ratio is smaller.

9. Behavior of Composite Pipes with Different Annulus Thickness

The larger the annulus, in other words, the thicker the grout the higher the load capacity. Wrinkles are found in the softer polymer grout, in the compression side of the tubular composite pipe. Annulus with 3.81cm, 2.54cm, 1.27cm exhibits the same failure behavior.

10. Double-wall Composite Pipe and Single-wall Pipe Comparison

The single-wall pipe has an issue with ovality whereas the double-wall pipe does not have it. For the same strain, for example, a strain of 2%, the double-wall pipe has the ability to rotate more angles than the single-wall pipe. The stresses are also slightly smaller in the double-wall composite pipe.

11. Intact and Welded Composite Pipe Analysis in Air Results Comparison.

A welded double-wall composite section has a higher strain, higher ovality, and higher stress than the intact composite pipe. So, the intact composite pipe ovality, strain, and stress should be amplified to account for the imperfect welded connection.

CHAPTER 9 FUTURE RESEARCH

1. Find the best polymer material to be used for the grout in the annulus of the pipeline.
2. Perform an in-depth study of the imperfect weld. The current research performs centerline offset of T/8 of the outer pipe for composite pipeline diameter with 24 inch and 20 inch with 0.5 inch thick for both pipes. The new study should change the pipe sizes and thicknesses. In addition the properties of the polymer materials and perhaps the size effect may also be studied.
3. It may also be worthwhile to study crack and its propagation on the composite pipe.
4. Include internal pressure and thermal effect in the FE analysis. Blast effect in the pipe and drop object studies should also be performed.The current study assumes the bond between steel and polymer is perfectly bonded. The actual bond between polymer and steel pipe should be studied.
5. Study fatigue of the SPS composite pipeline at the weld connection.
6. Perform 4 point loads experimental test for the composite pipe. This can be in a smaller scale. Test both cases of intact double-wall composite pipe and welded pipe. Investigate the results.
7. Study the application of SPS composite pipeline in different applications such as tunnel where the pipes pass through rocks.

BIBLIOGRAPHY

1111, A. R. (1999). Design, Construction, Operation, and Maintenance of Offshore Hydrocarbon Pipelines. *American Petroleum Institute*.

ACI. (2014). *Building Code Requirements for Structural Concrete (ACI 318-14).* American Concrete Institute.

API 579-1/ASME FFS-1. (2007). Fitness-For-Service. *The American Society of Mechanical Engineers*.

API-5L. (2013). *API Specificaiton 5L, Specification for Line Pipe.*

Arjomandi, K., & Taheri, F. (2012). Bending capacity of sandwich pipes. *Ocean Engineering*.

ASCE. (2005). *Guideline for the Design of Burried Steel Pipe.* Americal Socienty of Ciivil Engineers.

ASME-B31.1. (2001). *ASME code for pressure piping.*

Bai, Q., & Bai, Y. (2014). *Subsea Pipeline Design, Analysis, and Installation.* Gulf Professional Publishing.

Baker Jr, M., & Fessler, R. R. (2008). *Pipeline Corrosion.* U.S. Department of Transportation, Pipeline and Hazardous Materials Safety Administration, Office of Pipeline Safety.

Barnes, P., Hejazi, R., & Karrech, A. (2018). Instability of mechanically lined pipelines under large deformation. *Finite Elements in Analysis and Design*, 62-69.

Beer, F. P., Johnston, Jr., R. E., & DeWolf, J. T. (2006). *Mechanics of Materials.* Singapore: McGraw-Hill.

Berardo, G., Salvini, P., Mannucci, G., & Demofonti, G. (2000). On Longitudinal Propagation of a Ductile Fractuure in a Buried Gas Pipeline: Numerical and Experimental Analysis. *Proceedings of IPC2000: The International Pipeline Conference.* Alberta.

Broms, B. B. (1964). Lateral resistance of piles in cohesive. *Journal of the soil mechanics and foundations division, ASCE*.

Cohen, L. (2021, July 6). Retrieved from CBS News: https://www.cbsnews.com/news/gulf-of-mexico-fire-ocean-burst-pipeline/

DeepwaterHorizon. (2021). *Google*. Retrieved from en.wikipedia.org: https://en.wikipedia.org/wiki/Deepwater_Horizon

Demofonti, G., & Spinelli, C. M. (2011). Technical challenges facing the transport of anthropogenic CO2 by pipeline for carbon capture and storage purposes. *6th Pipeline Technology Conference 2011*.

DNV-OS-F101. (2013). *Submarine Pipeline Systems.* Det Norske Veritas.

Edition, A. R.-W. (2014). Planning, Designing, and Constructing Fixed Offshore Platforms—Working Stress Design.

Engineer, M. (2017, October 26). *Marine Engineering*. Retrieved from https://marine-engineerings.blogspot.com/2017/10/design-of-offshore-structures.html

Giakoumelis, G., & Lam, D. (2004). Axial capacity of circular concrete-filled tube columns. *Construction Steel Research 60*, 1049–1068.

Helwany, S. (2007). *Applied Soil Mechanics with ABAQUS Applications.* John Wiley.
Hetenyi, M. (1946). *Beams on elastic foundation.* Ann Arbor: The University of Michigan Press.
Hu, H. T., & Su, F. C. (2011). Nonlinear analysis of short concrete-filled double skin tube columns subjected to axial compressive forces. *Marine Structures*, 319–337.
Hu, H., & Schnobrich, W. (1989). Constitutive modeling of concrete by using nonassociated plasticity. *Material Civil Engineering 1(4)*, 199-216.
Hu, H.-T., & Su, F.-C. (2011). Nonlinear analysis of short concrete-filled double skin tube columns subjected to axial compressive forces. *Marine Structures*, 319–337.
Karamanos, S. A., Keil, B., & Card, R. (2014). Seismic design of buried steel water pipelines. *ASCE*.
Lam, D., Dai, X., Han, L., Ren, Q., & Li, W. (2012). Behaviour of inclined, tapered and STS square CFST stub columns subjected to axial load. *Thin-WalledStructures*, 54: 94–105.
Lardieri, A. (2018, January 16). *Google*. Retrieved from USNews.com: https://www.usnews.com/news/national-news/articles/2018-01-16/bp-takes-17-billion-charge-on-deepwater-horizon-costs-now-top-65b
Liang, Q. Q. (2017). Nonlinear analysis of circular double-skin concrete-filled steel tubular columns under axial compression. *Engineering Structures*, 639–650.
Liu, B., Liu, X. J., & Zhang, H. (2009). Strain based design criteria of pipelines. *Loss Prevention in the Process Industries*.
Luo, K., Pi, Y.-L., Gao, W., Bradford, M. A., & Hui, D. (2015). Investigation into long-term behaviur and stability of concrete-filled steel tubular arches. *Journal of Constructional Steel Research*, 127-136.
Mander, J. B., Priestley, M. J., & Park, R. (1988). Theoretical stress-strain model for confined concrete. *Journal of Structural Engeering, ASCE 114(8)*, 1804–1826.
Marshall, P. (2008). *Interpretive Discussion of Tubular Beam-Column Test Data.* Houston.
Marshall, P. W. (1982). An overview of recent work on cyclic inelastic behavior and system reliability. Structural stability Research Council.
Marshall, P. W. (1990). Advanced Fracture Control Procedures for Deepwater Offshore Towers. *American Welding Society*.
Marshall, P. W. (2004). Enhanced Strain-Based Design of Tubular Members. *Structural Stability Research Council.*
Marshall, P. W., & Thang, V. (2014). Radical Proposals for Hot Spot Stress. *Steel Construction, 7*(2).
Marshall, P. W., Gates, W. E., & Nahin. (1977). Analytical Methods for Determining the Ultimate Earthquake Resistance of Fixed Offshore Structures.
Marshall, P. W., Thang, V., & Brake, N. A. (2014). Bond Enhancement in Curved Sandwich Shells. *IceTech14.*
Matlock, H. (1970). Correlation for Design of Laterally Loaded Piles in Soft Clay. *Offshore Technology Conference.*

Meyer, B. J., & Reese, L. C. (1979). *Analysis of Single Piles Under Lateral Loading.* Center for Transportation Research, The University of Texas at Austin.

Mohr, W. (2003). *Strain-Based Design of Pipeline.* Submitted to US Dept. of Interior, Minerals Management Services and US Dept. of Transportation, Research and Special Programs Administration.

Mohr, W. (2007). Strain-Based Design of Pipelines.

Mursi, M., & Uy, B. (2003). Strength of concrete fillled steel box columns incorporating interaction buckling. *Journal of Structural Engineering, ASCE 129 (5)*, 626-639.

Nash, W. (1998). *Shaum's Outlines: Strength of Materials.* McGraw-Hill.

Pagoulatou, M., Sheehan, T., Dai, X., & Lam, D. (2014). Finite element analysis on the capacity of circular concrete-filled double-skin steel tubular (CFDST) stub columns. *Engineering Structures*, 102–112.

Papadaki, C. I., Karamanos, S. A., Chatzopoulou, G., & Sarvanis, G. C. (2018). Buckling of internally-pressurized spiral-welded steel pipes under bending. *International Journal of Pressure Vessels and Piping*.

Reese, L. C., & Impe, W. (2011). *Single Piles and Pile Groups Under Lateral Loading* (2nd ed.). Taylor & Francis Group, LLC.

Reese, L. C., Wiliam, M. I., & Wang, S. T. (2006). *Shallow and Deep Foundations.* Hobken: John Wiley & Sons.

Richart, F. E., Brandtzaeg, A., & Brown, R. L. (1928). *A study of the failure of concrete under combined compressive stresses, Bulletin No. 185.* Champaign: University of Illinois, Engineering Experiment Station.

Saenz, L. (1964). Discussion of Paper "Equation for Stress-Strain Curve of Concrete" by Desai, P. and Krishnan, S. *Journal of American Concrete Institute*, 61, 1229-1235.

Sherman, D. R. (1980). *Portal Tests.* University of Wisconsin-Milwaukee.

Tao, Z., Han, L.-H., & Zhao, X.-L. (2004). Behaviour of concrete-filled double skin (CHS inner and CHS outer) steel tubular stub columns and beam-columns. *Journal of Constructional Steel Research*, 1129–1158.

Thang, V., Hui, D., Zhou, J., & Marshall, P. W. (2022). Failure prevention of seafloor composite pipelines using enhanced strain-based design. *Reviews on Advanced Materials Science*, 306-321. https://doi.org/10.1515/rams-2022-0035

Thang, V., Marshall, P. W., Brake, N. A., & Adam, F. (2016). Studded bond enhancement for steel-concrete-steel sandwich shells. *Ocean Engineering*.

Tomii, M. (1991). Ductile and strong columns composed of steel tube, infilled concrete and longitudinal steel bars. *Proceedings of the 3rd international Conference on Steel-Concrete Composite Structures.* Fukuoka: Association of Steel-Concrete Structures.

Uckan, E., Akbas, B., Shen, J., Rou, W., Paolacci, F., & O'Rourke, M. (2015). A simplified analysis model for determining the seismic response of buried steel pipes at a strike-slip fault crossings. *Soil Dynamics and Earthquake Engineering*, 55-65.

Zhao, H.-S., Lie, S.-T., & Zhang, Y. (2018). FAtigue assessment of cracked pipes with weld misalignment by using stress intensity factors. *International Journal of Fatigue*, 192-209.

VITA

The author was born in Myanmar, formerly known as Burma. He received a Bachelor of Engineering degree in Civil Engineering from the National University of Singapore in 2010. Then, he worked in the offshore engineering industry for 3 years, designing oil and gas offshore jacked platforms in Southeast Asia offshore. He later earned a Master of Engineering Science degree from Lamar University, Texas, in 2014. He started taking courses at the University of New Orleans in the Spring of 2017 and later enrolled in Ph.D. in Engineering and Applied program in 2018 Spring. He is practicing his profession in the field of science and engineering and is a licensed professional engineer in the State of Texas.